Phosphoproteomics identifies microglial Siglec-F inflammatory response during neurodegeneration

Highlights

- Phosphoproteomics analysis of CK-p25, 5XFAD, and Tau P301S mouse models finds dysregulated signaling networks associated with Alzheimer's disease pathologies.
- A phosphorylation site on Siglec-F is found to be upregulated across all three models of disease.
- Expression of Siglec-F and its human paralog Siglec-8 is increased in reactive microglia.
- Overexpression of Siglec-F and Siglec-8 *in vitro* drives an endocytic and pyroptotic inflammatory response.

Authors

Nader Morshed[1,2], William T. Ralvenius[3,4], Alexi Nott[3,4,5], L. Ashley Watson[3,4], Felicia H. Rodriguez[6], Leyla A. Akay[3,4], Brian A. Joughin[1,2], Ping-Chieh Pao[3,4], Jay Penney[3,4], Lauren LaRocque[1], Diego Mastroeni[7], Li-Huei Tsai[3,4,8,#], Forest M. White[1,2,9,*]

1 Department of Bioengineering, Massachusetts Institute of Technology, Cambridge, MA, 02139, USA

2 Koch Institute for Integrative Cancer Research, Massachusetts Institute of Technology, Cambridge, MA 02139, USA

3 Picower Institute for Learning and Memory, Massachusetts Institute of Technology, Cambridge, MA 02139, USA

4 Department of Brain and Cognitive Sciences, Massachusetts Institute of Technology, Cambridge, MA 02139, USA

5 Department of Cellular & Molecular Medicine, University of California San Diego, La Jolla, CA 92093, USA

6 Department of Chemical and Materials Engineering, New Mexico State University, Las Cruces, NM 88003, USA

7 ASU-Banner Neurodegenerative Disease Research Center, Tempe, Arizona 85287, USA

8 Broad Institute of MIT and Harvard, Cambridge, MA 02142, USA

9 Center for Precision Cancer Medicine, Massachusetts Institute of Technology, Cambridge, MA 02139, USA

Correspondence: lhtsai@mit.edu

* Correspondence: fwhite@mit.edu

In Brief

Phosphoproteome signaling changes associated with Alzheimer's disease (AD) are poorly characterized. Here, Morshed et al. apply phosphoproteomics to mouse models of AD to uncover a novel microglial receptor, Siglec-F, that is upregulated on a subset of inflammatory microglia across models of neurodegeneration. The human paralog, Siglec-8 is also found to be upregulated in late-onset AD microglia. Overexpression of Siglec-F and related human Siglecs activates pro-inflammatory signaling responses in BV-2 cells.

Summary

Alzheimer's disease (AD) is characterized by the appearance of amyloid-β plaques, neurofibrillary tangles, and inflammation in brain regions involved in memory. Using mass spectrometry, we have quantified the phosphoproteome of the CK-p25, 5XFAD, and Tau P301S mouse models of neurodegeneration. We identified a shared response involving Siglec-F which was upregulated on a subset of reactive microglia. The human paralog Siglec-8 was also upregulated on microglia in AD. Siglec-F and Siglec-8 were upregulated following microglial activation with interferon gamma (IFNγ) in BV-2 cell line and human stem-cell derived microglia models. Siglec-F overexpression activates an endocytic and pyroptotic inflammatory response in BV-2 cells, dependent on its sialic acid substrates and immunoreceptor tyrosine-based inhibition motif (ITIM) phosphorylation sites. Related human Siglecs induced a similar response in BV-2 cells. Collectively, our results point to an important role for mouse Siglec-F and human Siglec-8 in regulating microglial activation during neurodegeneration.

Introduction

Alzheimer's disease (AD) is a neurodegenerative disease which presently affects over 5.8 million Americans and 55 million people worldwide (2020). Recent evidence has identified distinct stages of AD development, from: early amyloid-β (Aβ) deposition, tau hyperphosphorylation, release of pro-inflammatory cytokines, reactive gliosis, demyelination, synaptic loss, metabolic changes, and ultimately neurodegeneration (De Strooper and Karran, 2016). The impact of gliosis on this process is emphasized by recent genome-wide association studies (GWAS) that have uncovered mutations in microglial genes, including TREM2, CD33 and INPP5D, which contribute to disease pathogenesis through phosphorylation signaling (Colonna and Wang, 2016; Jansen et al., 2019; Kunkle et al., 2019; Lambert et al., 2013). Biochemical studies have highlighted the important role of signaling networks involving protein kinases such as cyclin-dependent kinase 5 (Cdk5), Gsk3β, PKCα, and EphA4 in mediating pathological processes linked to Aβ and phospho-Tau (Alfonso et al., 2016; Choi et al., 2014; Patrick et al., 1999; Rosenberger et al., 2014). However, there have been few studies of how these signaling proteins affect proteome-wide phosphorylation events, or the phosphoproteome, during neurodegeneration.

Tools to measure the phosphoproteome have been developed using mass spectrometry (MS) (Ficarro et al., 2002; Lemeer and Heck, 2009; Rigbolt and Blagoev, 2012; Riley and Coon, 2016; White and Wolf-Yadlin, 2016; Zhang et al., 2005). However, previous studies in AD have analyzed only a portion of the phosphoproteome and overlooked critical phosphotyrosine (pTyr)-sites that mediate the activity of many known kinases (Bai et al., 2020; Dammer et al., 2015; Henriques et al., 2007; Hoos et al., 2013; Marttinen et al., 2018; Tagawa et al., 2015; Yu et al., 2016). We aimed to measure and compare the phosphoproteomes of different mouse models of AD in order to understand signaling changes linked to neurodegeneration. We analyzed three separate mouse models of Alzheimer's disease and

neurodegeneration: (1) CK-p25 (Cruz et al., 2003), a model of p25/Cdk5 activation in forebrain neurons; (2) 5XFAD (Oakley et al., 2006), a model of Aβ toxicity; (3) Tau P301S (Ghetti et al., 2002), a model of phospho-Tau and neurofibrillary tangles. Using a sensitive sample enrichment protocol, we quantified low-abundance pTyr peptides and global phosphoserine / phosphothreonine (pSer/pThr) peptides in the hippocampus and cortex of these mice where pathology occurs.

Downstream analysis of these datasets revealed neuronal, astrocytic, and microglial phosphorylation signaling changes associated with disease. Furthermore, we observed dysregulation of Cdk5 phosphorylation substrates in these mouse models. We found that the Δp35KI mutation, which attenuates Cdk5 overaction by blocking calpain-mediated cleavage of Cdk5 activator p35 into p25 (Lee et al., 2000; Seo et al., 2014), exerted a protective effect on the neuronal CaMKII-linked phosphoproteome in mice with 5XFAD background. Across all models, we observed an increase in phosphorylation on Siglec-F (Also known as Siglec5), a member of the CD33-related Siglec family of immunoreceptors (Angata et al., 2004; Zhang et al., 2007). We found that Siglec-F was upregulated on a subset of reactive microglia in CK-p25 and 5XFAD mice. These Siglec-F^{+} microglia appeared early on in disease progression and were spatially correlated with Aβ pathology. While mouse Siglec-F does not have a direct homolog in humans, there are several human Siglecs that share features with Siglec-F (Duan and Paulson, 2020). We identified human Siglec-8, the functionally convergent paralog of mouse Siglec-F (Tateno et al., 2005), upregulated in post-mortem brain samples from late-onset AD patients.

To assess the functional effects of Siglec-F, we designed several *in vitro* models of Siglec activation on microglia. We found that treatment with interferon gamma (IFNγ) increased Siglec-F expression using BV-2 cells, an immortalized line model of mouse microglia (Henn et al., 2009). We similarly observed that induced pluripotent stem cell (iPSC)-derived microglia (iMGLs) had increased Siglec-8 expression after IFNγ treatment. We found that Siglec expression in BV-2 cells activates an endocytic and pyroptotic inflammatory response in an ITIM-dependent manner. These phenotypes were rescued by blocking sialic acid substrate binding and inhibiting signaling through Janus Kinase (JAK), SHP-2, and NLRP inflammasome pathways. Together, these data highlight Siglec-F and Siglec-8 as new markers for activated microglia and potential targets for modulating neuroinflammation in AD.

Results

CK-p25 phosphoproteomics identifies activated signaling preceding neurodegeneration

To characterize signaling network changes in several mouse models of neurodegeneration, we used mass spectrometry-based phosphoproteomics to quantify the pTyr phosphoproteome, global phosphoproteome, and protein expression profiles of brain tissues from diseased and wildtype (WT) mice. We first examined CK-p25 mice which can activate p25/Cdk5 signaling in forebrain neurons in an inducible manner. By removing doxycycline from the diet of these mice, we can induce gliosis within two weeks as well as neuronal loss and cognitive deficits by 6 weeks (Gjoneska et al., 2015., Mathys et al., 2017). We collected tissue from adult mice (3-4 months old (m.o.)) induced for 2 weeks to capture signaling changes that precede neurodegeneration. Briefly, peptides from the hippocampus, cortex, and cerebellum were labeled with isobaric tandem mass tags (TMT), enriched for pTyr peptides by immunoprecipitation (IP), and analyzed by quantitative multiplex LC-MS/MS analysis using a previously described methodology (Dittmann et al., 2019; Reddy et al., 2016) (**Figure 1A, Table S1**). To gain insight into signaling downstream of activated Cdk5 in this model, the pTyr IP supernatant of each tissue was

enriched for CDK and MAPK substrates by IP with a phospho-motif specific antibody (Joughin et al., 2009). We subsequently performed a deep analysis of the global (pSer/pThr) phosphoproteome on the supernatant from this second IP of cortical tissue, through reverse-phase fractionation followed by immobilized metal affinity chromatography-based pSer/pThr enrichment. Finally, protein expression profiling was performed on IP supernatant. This strategy led to the identification and quantification of 10,828 unique peptides (10% pTyr, 70% pSer/pThr, Supplementary Table 1) across the hippocampus and cortex of CK-p25 and CK control mice (CK-p25: n=3; CK: n=3). In agreement with the known forebrain-specific expression of p25 in this model, no significant changes were detected in protein phosphorylation in cerebellum samples from control and CK-p25 mice (**Table S1**).

Among peptides from the hippocampus and cortex, 318 were upregulated and 111 were downregulated in CK-p25 mice relative to CK controls (**Figure S1A, S1B**). Among the upregulated pTyr peptides there was a set of sites that map to proteins predicted to be primarily expressed in microglia and astrocytes in the hippocampus and cortex of CK-p25 mice (**Figure 1B, S1C-S1E**). In addition to pTyr changes, we observed a larger number of upregulated pSer/pThr sites (**Figure S1A, S1B**). Motif analysis of the global pSer/pThr dataset found a -pS/T-P- motif with lysine in the +2 and +3 positions enriched in the upregulated set of peptides (**Figure S1F**), which matches the reported substrate motif of CDKs (Beaudette et al., 1993; Songyang et al., 1994; Suzuki et al., 2015). Among the upregulated pTyr and pSer/pThr phosphosites, we found several kinases, receptors, and transcription factors, including Stat3 (pY705), Cdk1/2/3 (pY15), Galk2 (pS208), Erk1 (Mapk3; pT203, pY205), Brsk2 (pS456, pT460, pS468), Src (pY535), Lyn (pY316), Fgr (pY511), Fyn (pY531), Protein Kinase C δ (Prkcd; pY311), Ick (pY159), Mak (pT157), Pik3r1 (pY467; pY580; pY467), Inpp5d (pY868), and Siglec-F (pY561). Among these proteins, Cdk1, Stat3, Erk1, Brsk2, Inpp5d, Src, and Fyn have been previously reported to be associated with neurodegeneration (Cavallini et al., 2013; Counts and Mufson, 2017; Haim et al., 2015; Karch and Goate, 2014; Mota et al., 2014; Poulsen et al., 2017). Our data sheds new light on their involvement at an early stage in this mouse model. Further, increased phosphorylation of specific Src-family kinases (Src, Lyn, Fgr, Fyn) represents a novel insight into signaling pathway changes that have not been identified in other AD phosphoproteome datasets lacking pTyr enrichment. Overall, our phosphoproteomics analysis in CK-p25 mice shows that significant pTyr and pSer/pThr signaling changes are associated with neuroinflammation prior to neuronal loss during neurodegeneration.

5XFAD and Tau P301S phosphoproteomes tie unique signaling events to AD pathologies

We next assessed the 5XFAD (Oakley et al., 2006) AD mouse model to see if there were common trends in signaling changes associated with Aβ pathology. Using a the same phosphopeptide enrichment methodology, we examined mice that were 9-10.5 m.o. with the aim of identifying signaling changes induced after pathology became pervasive in the hippocampus. This strategy led to the identification of 24,365 unique peptides (4% pTyr, 80% pSer/pThr) in the hippocampus and cortex of 5XFAD mice (5XFAD: n=8; WT: n=4; **Table S1**). Of these peptides, 191 were upregulated and 105 were downregulated in 5XFAD compared to WT mice (**Figure S1B, S2A)**. These changes included two peptides from the transgene amyloid precursor protein (APP): LVFFAEDVGSNK and HFEHVR (**Figure S2B**). We identified pTyr sites that were upregulated on neuron-enriched proteins, including Dlg2, Epha5/6, and Syt1, as well as microglia-enriched proteins Siglec-F, Inpp5d, Fyb1, Grp84, Ptprc, Dock2, and Lsp1 (**Figure 1C, S1F, S1C**). We observed some overlap in upregulated peptides between the hippocampus and cortex, although the correlation between tissue changes was lower than in CK-p25 (**Figure S1D, S2D**). Motif

analysis identified the enriched motif: -L-.-R-Q-.-pSer/pThr-[VLIMF]- within the set of downregulated peptides in the hippocampus (**Figure S2E**). This motif closely matches the substrate motif of CaMKII, a kinase known to be dysregulated by Aβ in AD (Ghosh and Giese, 2015; White et al., 1998). Phosphosite enrichment analysis (PSEA) found that CaMKII-substrates were negatively associated with 5XFAD genotype (**Figure 1D**), further supporting decreased CaMKII activity in this model. We also observed that the downregulated phosphosites were enriched for proteins specifically expressed in neurons (**Figure S1E**). Together these data point to a model in which Aβ activates particular glial and neuronal signaling pathways and suppresses overall CaMKII activity in the hippocampus.

To determine the role of p25/Cdk5 signaling in 5XFAD AD pathogenesis, we compared the phosphoproteome of 5XFAD and WT mice to those crossed with mice harboring the Δp35KI mutation. Δp35KI prevents Cdk5 overactivation by blocking the generation of p25 from p35 by calpain in neurotoxic conditions (Lee et al., 2000; Seo et al., 2014). We found multiple Δp35KI-linked phosphorylation sites that were decreased in 5XFAD and corrected back to WT levels in 5XFAD;Δp35KI mice (**Figure S2F**). Of these Δp35KI-linked sites, 62% matched the purported CaMKII phosphorylation motif in at least two adjacent residue positions compared to 16% pSer/pThr sites in background dataset. Intriguingly, we did not observe any effects of Δp35KI on markers of glial activation (Astrocyte: Aqp4, Gfap; Microglia: Ctsb, Ctsd, Siglec-F, Inpp5d). These findings suggest that Aβ activates microglia and astrocytes independent of p35 cleavage into p25, while suppressing signaling in neurons in a p25-dependent manner.

To assess signaling changes that occur in a Tau-centric model of AD and neurodegeneration, we quantified the phosphoproteome in Tau P301S mouse model (Ghetti et al., 2002). Using a similar phosphoproteomic platform, we collected pTyr, global pSer/pThr, and protein expression data from hippocampal tissues of 4 m.o. mice when pathologies first development. Interrogation of the 4 m.o. Tau P301S dataset revealed minimal signaling from activated microglia, in agreement with disease progression in this model that suggests microgliosis occurs in grey matter at ~6 m.o. (van Olst et al., 2020; Yoshiyama et al., 2007). We therefore also obtained hippocampal tissues from 6 m.o. mice and quantified tyrosine phosphorylation to focus on signaling from activated microglia, as detected in our analysis of other models. In total, we identified 11,853 total unique peptides (6% pTyr, 83% pSer/pThr) across all tissues (P301S: 4 m.o. n=5, 6 m.o. n=4; WT: 4 m.o. n=5, 6 m.o. n=4, 9 m.o. n=1; **Table S1**). Of these peptides, 297 were upregulated while 30 were downregulated in Tau P301S mice compared to controls (**Figure S1B**). We found that pTyr peptide abundance increased at both 4 and 6 m.o. in P301S mice (**Figure 1E, Figure S3A**). The global pSer/pThr phosphoproteome changes were dominated by increased phosphorylation of transgenic MAPT peptides (**Figure S3B, S3C**) as well as members of the collapsin response mediator proteins (Crmp1, Crmp2/Dpsyl2, Crmp4/Dpysl3, Crmp5/Dpsyl5), cytoskeletal proteins (Tuba1-4,8, Tubb1-6, Nefm, Stmn1, Map1b), and synapse-associated proteins (Cdh8, Dlg2, Tanc2, Syn2, Bcan). Peptides that were upregulated at 4 m.o. were similarly upregulated in 6 m.o. mice (**Figure S3D**). However, in 6 m.o. mice we saw upregulation of two microglia-enriched pTyr peptides (Siglec-F, Inpp5d) (**Figure 1E**). In contrast with the other models, we did not identify any enriched phosphorylation motifs in P301S mice. Together, our phosphoproteome data sets allow us to compare and contrast signal networks in different neurodegenerative processes.

Cross-model comparison identifies shared kinase and microglial activation

To identify central signaling nodes associated with AD and neurodegeneration, we searched for common changes across mouse models. Phosphosite enrichment analysis (PSEA) identified signatures of shared kinase activation for CDK1/2/5, ERK1/2, and GSK3B (**Figure 1D**). Among these kinase family members, we identified protein changes on Cdk5 as well as phosphosite changes on Erk1, Cdk1/2/3, and Src; all of which were significantly upregulated in 2wk CK-p25 mice. We additionally observed increased phosphorylation on Gsk3a/b in 6 m.o. Tau P301S mice (**Supplementary Data Table S2**). Across all disease models, we identified two phosphopeptides that were consistently upregulated: Siglec-F (Siglec5; pY561) and Inpp5d (pY868) (**Figure 1F, 1G**). We manually validated these spectra to confirm the peptide assignments were correct (**Figure S3E, S3F**). Both of these proteins are expressed primarily in microglia and are related to human genes *CD33* and *INPP5D* identified in AD GWAS studies (Karch and Goate, 2014). Due to the under-explored nature of Siglec-F in neurodegeneration, we next investigated its role in microglial activation.

Siglec-F is upregulated on subsets of inflammatory microglia

To determine whether increased Siglec-F phosphorylation was associated with increased Siglec-F protein expression in our models, we used immunofluorescence (IF) imaging to locate and quantify Siglec-F expression. We first validated that the antibody E50-2440 was able to label Siglec-F in BV-2 cells with stable viral protein expression of Siglec-F carrying mutated pTyr sites, with minimal immunoreactivity in control cells expressing an empty vector (**Figure S4A**). We next stained CK and CK-p25 brain slices from mice after 3 weeks of p25 induction. We observed that a subset of Iba1^{+} microglia in CK-p25 mice stained positive for Siglec-F expression (**Figure 2A**). In contrast, we did not observe immunoreactivity for Siglec-F on microglia in CK control mice that lack p25 expression. As previously observed, CK-p25 microglia exhibited gliosis (Mathys et al., 2017), quantified here as an increase in the area covered by Iba1 signal (**Figure 2B**). Relative to these changes, Siglec-F was upregulated throughout the dentate gyrus (DG), CA1, CA2, and CA3 regions of the hippocampus in CK-p25 mice (**Figure 2C, S4B, S4C**). Across all four regions, ~15-35% of area was positive for Siglec-F relative to Iba1 and this amount was highest in the CA3. We quantified the % area overlap of Siglec-F and Iba1 in CK-p25 mice and found that 97% of Siglec-F signal was located ≤2 voxels away from Iba1 (**Figure S4D, S4E**). Together, our findings show that Siglec-F is expressed on a subset of activated microglia in the CK-p25 mouse model.

We next stained for Siglec-F and Iba1 expression in 5XFAD mouse brain tissue. To understand if these microglia are linked to early Aβ deposition, we stained the hypothalamus of 2 m.o. 5XFAD mice where Aβ plaques are first observed (Canter et al., 2019). We observed microglia in this region that expressed Siglec-F in proximity to Aβ plaques (**Figure 2D**). By 6 months of age, we found Siglec-F^{+} microglia throughout the thalamus, hippocampus, and cortex of 5XFAD mice (**Figure 2E, 2F, S4F**). The amount of Siglec-F was positively correlated with the total volume of Aβ plaques in each field of view (**Figure 2G**). As in CK-p25 mice, >99% of all Siglec-F signal was located ≤2 voxels away from Iba1 (**Figure S4G, S4H**). Similar to CK controls, we observed minimal Siglec-F signal in 6 m.o. non-Tg mice (**Figure 2F**). To test whether these Siglec-F^{+} microglia were plaque-associated, we calculated the mean distance between Siglec-F and Iba1 mask voxels and neighboring Aβ plaques in wide-field z-stack images from plaque-containing regions of 6 m.o. 5XFAD animals. We observed that Siglec-F^{+} voxels were significantly closer to Aβ plaques compared to total Iba1 (**Figure 2H**). Together these data show that Siglec-F is upregulated on microglia in response to Aβ pathology and may play a role in microglia activation.

To further explore the potential relationship between Siglec-F and microglial activation, we analyzed published single-cell and bulk RNA-seq data sets. In CK-p25 mice (Mathys et al., 2017), we observed three Siglecs (*Siglec-1*, *Cd22*, and *Siglec-F*), upregulated in late-response reactive microglia that appear by two weeks of p25 induction (**Figure S5A**). Other Siglecs (*Cd33*, *Siglec-E*, *Siglec-G*, *Siglec-H*) were downregulated in late-response microglia when compared with homeostatic microglia from CK controls. A subset of these reactive microglia that express type-II interferon response genes (marker genes: *Cd74*, *H2-Ab1*) showed highest Siglec-F expression. We next examined the disease-associated microglia (DAM; marker genes: *Lpl*, *Cst7*) population identified in 5XFAD mice (Keren-Shaul et al., 2017) and observed a similar trend: Siglec-1, CD22, and Siglec-F were all upregulated in DAM compared to homeostatic microglia (**Figure S5B**). Moreover, a gene co-expression network analysis found that Siglec-F expression increased in the entorhinal cortex of 4-6 m.o. Tau P301L (rTg4510) mice (Castanho et al., 2020). Finally, Siglec-F was found to be upregulated in the hippocampus of 24-29 m.o. mice compared to 3 m.o. (Stilling et al., 2014). These results suggest that activated microglia express Siglec-F in brain regions associated with aging and neurodegeneration.

Siglec-8 is upregulated in aging-associated microglia

To identify the human receptor analog of mouse Siglec-F, we examined published single-cell sequencing data sets. While CD33 has been previously identified in IHC staining of AD patient tissue (Griciuc et al., 2013), other related receptors Siglec-5 and Siglec-8 have not been carefully examined. Siglec-5 shares the closest sequence homology with Siglec-F (Aizawa et al., 2003; Angata et al., 2001), however, Siglec-8 more closely matches the substrate binding and expression pattern of Siglec-F on eosinophils (O'Sullivan et al., 2018). A single-cell analysis on temporal lobe biopsies identified two clusters of MHC-II^{+} aging-associated microglia (Sankowski et al., 2019). Siglec-8 was classified as a marker gene for one of these aging-associated microglia populations and was upregulated only in these two clusters. An additional snRNA-seq analysis of human AD (Zhou et al., 2020) found an AD-associated microglia cluster that had increased expression of Siglec-8. We examined bulk tissue RNA microarray data from young and aging brain tissues obtained from a previously published dataset (Berchtold et al., 2008)**.** We found that Siglec-8 had increased expression in individuals over the age of 60 in the hippocampus and other brain regions (**Figure 2I, 2J, S5C, S5D**). Among individuals with age ≥60 we observed a trend towards increased Siglec-8 transcript abundance in AD, but this effect was not significantly different from MCI and ND cases. These data suggest that Siglec-8 expression may be upregulated in aged human microglia, while little is known about Siglec-5 due to its low expression levels.

To explore whether Siglec-8^{+} microglia are present in AD, we used IF to quantify Siglec-8 expression in human post-mortem cortical tissues. We first stained for Siglec-5 and Siglec-8 and observed that Siglec-8 signal was co-localized with Iba1 (**Figure S6A**). We showed that this Siglec-8 antibody (ab198690) was able to label BV-2 cells expressing Siglec-8 (**Figure S6B**). We then stained for Siglec-8, MHC-II, and Iba1 in human cortical sections containing both white matter (WM) and grey matter (GM) regions. We analyzed tissue from a healthy control, early-onset AD patients and late-onset AD patients (n=1, 58 y.o., Braak I; n=3, 60 y.o., Braak VI; n=4, 77-96 y.o., Braak IV-V; **Table S2**). We observed Siglec-8 signal co-localized with Iba1^{+}/MHC-II^{+} microglia in early- and late-onset AD patients (**Figure 2K, S6C-S6E**). For each image, we generated fluorescent signal masks for quantification of channel overlap. We observed that 75% of Siglec-8 signal was located ≤2 voxels away from Iba1 or MHC-II in images with minimal blood vessel autofluorescence (**Figure S6F, S6G**). We then compared percent

area of Siglec-8 localized to Iba1 across patient groups and found increased overall Siglec-8 expression in late-onset AD compared with early-onset and control individuals (**Figure 2L, 2M**). This comparison was significant both when comparing individual image stack averages as well as patient averages from GM and WM regions. Although Siglec-8 expression was increased in some brain regions of early-onset AD patients, this effect was not significant compared to the control patient samples. Siglec-8$^+$ microglia did not appear to be significantly biased towards either WM or GM regions (**Figure S6H**). The amount of Siglec-8 also did not appear to be correlated with the total volume of Aβ plaques in a field of view (**Figure S6I**). Altogether, these results show that microglia upregulate Siglec-8 in an age-dependent manner.

Siglec-F and Siglec-8 can be upregulated by IFNγ

Given that Siglec-F$^+$ microglia were enriched for type II interferon response genes (Mathys et al., 2017) in the CK-p25 model, we next sought to understand whether Siglec-F and Siglec-8 are regulated by inflammatory cytokine signaling. Previous work has identified the cytokine interferon gamma (IFNγ) as a regulator of type II interferon inflammation in AD patients and mouse models of neurodegeneration (Mastrangelo et al., 2009; Wood et al., 2015; Zheng et al., 2016) and a potential driver of Siglec-8 expression in eosinophils (Steinke et al., 2013). Using flow cytometry, we found that BV-2 cells treated with 10 ng/mL IFNγ for 72 hours had increased Siglec-F expression (**Figure 3A**). In this system, we observed that cells had increased size, reduced cell count, and reduced doubling times after treatment with IFNγ (**Figure S7A-S7C**). The effects on cell size and proliferation were observed in treatments between 1 and 100 ng/mL IFNγ, suggesting that we are saturating IFNγ receptor signal. IFNγ is known to signal through Janus kinase 1 and 2 (Jak1/2), which can be targeted with the small molecule inhibitor tofacitinib (Flanagan et al., 2010). The effects of IFNγ on cellular phenotypes and Siglec-F expression were blocked by co-treating cells with ≥5 μM tofacitinib (**Figure 3A, S7D, S7E**). Together these data show that Siglec-F expression can be upregulated by IFNγ and mediated through the Jak1/2 pathway.

We next tested the effect of IFNγ on an *in vitro* human iPSC-derived microglia (iMGL) model. We observed that iMGLs upregulated Siglec-8 expression after 72 hours of treatment with 25 ng/mL IFNγ by IF (**Figure 3B**). This effect was less effective with IFNα or IFNβ, suggesting type-II interferon signaling dependence (**Figure 3C**). We observed that co-treatment of iMGLs with IFNγ and 5 μM tofacitinib was able to reverse the upregulation of Siglec-8 by IF and qPCR (**Figure 3D, S7F, S7G**). We were able to replicate these effects in iMGLs matured in the presence of homeostasis-inducer TGFβ (Butovsky et al., 2014) (**Figure S7H**). In summary, our results support the link between Siglec-F and Siglec-8 expression with type II interferon-activation states.

Siglec expression in BV-2 cells induces cell death

To explore the functional relevance of expression and phosphorylation of Siglec-F and related receptors, we designed a Siglec-overexpression system using BV-2 cells. Previous studies suggest that Siglec activation can trigger apoptotic events in T cells and eosinophils (El Firar et al., 2009; Kiwamoto et al., 2015; Youngblood et al., 2019; Zhang et al., 2007; Zimmermann et al., 2008). Using a constitutive MCSV-IRES-puro (MIP) retroviral construct we found that overexpression of Siglec-F leads to an increased culture doubling-time (**Figure 4A**). This effect was dependent on Siglec-F's cytosolic tyrosine residues, as individual Y561F or Y538F mutations led to a partial loss-of-function (LOF), while the Y538F;Y561F (2xY->F) mutant showed complete LOF (**Figure 4A**). Increased doubling times were associated with ligand binding, as co-treatment of cells with 50 mU sialidase was able to partially restore

proliferation in WT Siglec-F cells. However, sialidase treatment was slightly toxic to cells carrying LOF mutations as measured by an increase in doubling time (**Figure 4A**). Using flow cytometry, we observed an increased proportion of BV-2 cells expressing WT or Y561F Siglec-F that were labeled with early (Annexin-V$^+$) and late apoptotic (Annexin-V+; PI$^+$) markers (**Figure 4B**). Thus it appears that constitutive overexpression of Siglec-F activates a cellular death program such as apoptosis, necroptosis, pyroptosis, or ferroptosis (Green, 2019).

We repeated these experiments using the human Siglec receptors: CD33, Siglec-5, and Siglec-8, based on their respective implication in AD GWAS studies (Carrasquillo et al., 2011; Hollingworth et al., 2011), closest sequence homology to Siglec-F, and closest substrate binding pattern to Siglec-F (preferring 6'-sulfo-sLe^x) (O'Sullivan et al., 2018). Overexpression of each human Siglec caused a similar reduction in proliferation rate, while 2xY->F mutations (CD33 Y340F;Y358F, Siglec-5 Y520F;Y544F, and Siglec-8 Y447F;Y470F) restored proliferation to WT rates (**Figure 4A**). Co-treatment with 50 mU sialidase was able to restore proliferation in CD33-expressing cells to a similar degree as Siglec-F. However, the effect of sialidase was not as strong in cells expressing Siglec-5 or Siglec-8, suggesting a possible difference in substrate binding patterns necessary for Siglec activation (**Figure 4A**). These results indicate that Siglec-F and related human Siglec receptors may signal in a similar ITIM-dependent manner to induce cell death, although their activating context may vary slightly.

To further validate these findings, we repeated these experiments in BV-2 cells using the pINDUCER dox-inducible lentiviral toolkit (Meerbrey et al., 2011). Expression of Siglec-F in this system showed dose-dependent impairment of proliferation with differences in cell count and confluency within 24 hours after addition of 500 ng/mL doxycycline (**Figure 4C, S8A**). Previous literature suggests that that the N-terminal V-set domain of Siglecs is necessary for sialic acid substrate binding (Griciuc et al., 2013). We tested an additional construct of Siglec-F in this system that has its V-set binding domain deleted (Siglec-F ΔV-set: ΔD18-D116). Siglec-F ΔV-set had the same growth rate as 2xY->F cells (**Figure 4C**), suggesting a similar LOF caused by impaired substrate binding. Together our findings indicate that Siglec-F ligand binding and ITIM phosphorylation are necessary to induce cell death.

ITIM-containing Siglecs activate inflammatory signaling pathways

To gain further insight into the mechanistic effects of Siglec activation, we examined gene expression changes in BV-2 cells overexpressing Siglec-F or related human Siglecs using bulk RNA-seq. Downstream analysis identified overlapping transcriptional network alterations induced by all four Siglec receptors (**Figure 4D, Table S3**), including components of the complement system (*C1qa*, *C1qb*, *C1qc*, *C3*), components of the inflammasome (*Nlrp1a*, *Nlrp1b*, *Casp1*, *Casp4*, *Gsdmd*), pro-inflammatory cytokines (*Il1a*, *Il1b*, *Il18*, *Tnf*), and lysosomal proteins (*Lyz1*, *Lyz2*) (**Figure 4D**). This could potentially explain the mechanism of Siglec-induced cellular death, as the inflammasome is known to regulate pyroptosis (Green, 2019). In contrast, 2x->F mutants and empty vector controls did not induce transcriptional changes for these genes, suggesting a critical role for ITIM phosphorylation in driving gene expression changes. Close to half of all Siglec-F upregulated genes were also induced by all 3 of the human Siglecs (**Figure 4E**). Siglec-F and Siglec-5 shared the most similar gene expression changes (90% differentially expressed gene (DEG) overlap), while CD33 and Siglec-8 both induced a unique set of DEGs (32% and 38% shared DEGs with Siglec-F, respectively). We next sought to validate whether the shared signaling pathways involving the inflammasome could be reproducibly activated by Siglec-F. We validated that Siglec-F drove increased IL-1β production after dox-induction using qPCR (**Figure 4F**) and western blot (**Figure 4G**) analyses. Previous literature has found that aminopeptidase inhibitor bestatin

can block anthrax lethal toxin-induced cell death via NLRP1 (Chui et al., 2019; Wickliffe et al., 2008). We found that bestatin was able to partially reverse the effects of Siglec-F on BV-2 proliferation in our growth curve assay (**Figure S8B, S8C**). In summary, our results show that expression of Siglec-F and related human Siglecs activates an inflammatory signaling response in BV-2 cells.

To understand the signaling networks connecting Siglec ITIM phosphorylation with downstream gene expression changes, we applied pTyr analysis to BV-2 cells expressing Siglec-F and related human Siglecs (**Figure 5A, Table S4**). We found that Siglec-F drove reduced phosphorylation on a large number of proteins (**Figure 5B**), consistent with its role as an inhibitory receptor. These downregulated phosphopeptides included proteins associated with cellular adhesion, metabolic processes, signal transduction, cellular cytoskeleton, and endosomal trafficking. However, we also observed several pTyr sites on proteins involved in signal transduction that were increased in abundance after Siglec-F expression (**Figure 5C**). Among these sites, we observed that Inpp5d, Prkcd, Inppl1, Dok1, Lyn, Fyb1, Erk1 (Mapk3), and Pik3r1 has increased phosphorylation in our CK-p25 model (**Figure 5D**). This signaling response appeared to be due to ITIM phosphorylation and was shared among human Siglecs, as several of these phosphopeptides had a common directional change in response to CD33, Siglec-5, and Siglec-8 expression (**Figure 5E, 5F**). To validate that these signaling changes do not occur during generation of stable cell line, we selected Erk1/2 (Mapk3/1) as targets and blotted for phospho-Erk activation in BV-2 cells with inducible Siglec-F expression. We observed that Erk1 and Erk2 had increased phosphorylation after 48 hours of dox induction of Siglec-F but not 2xY->F mutants (**Figure S8D, S8E**). Myc-tagged Siglec-F itself was expressed as a 70 kDa glycoprotein that was downregulated after 48 hours of induction in response to its own activation (**Figure S8D, S8F**). In support of our transcriptomic data, we also saw an overlapping set of proteins that increased in the global proteome analysis of BV-2 cells (**Figure S8G**). In addition, we observed the Siglec-F phosphopeptide (SVyTEIK) was specifically increased in Siglec-F expressing cells (**Figure S8H**). Together, our transcriptomic, proteomic, and pTyr analyses suggest that Siglec-F may play a dual role in inhibiting selected microglial signaling events while activating inflammatory response pathways.

Phosphorylation of Siglec ITIM sites is known to recruit SHP-2, a tyrosine phosphatase linked to ERK 1/2 activation (Chemnitz et al., 2004; Sang et al., 2019). SHP099 is a recently developed allosteric inhibitor of SHP-2 (Chen et al., 2016). By pulling down against a C-terminal myc epitope tag on Siglec-F, we found that SHP099 disrupted the interaction between SHP-2 and Siglec-F at 1 µM without blocking SHP-1 (**Figure 5G**). To understand the role of SHP-2 in mediating signaling from the ITIM phosphorylation sites, we performed quantitative pTyr analysis of SHP099-treated cells. Out of 41 unique pTyr sites upregulated by Siglec-F expression, 7 were decreased with SHP-2 inhibition in this analysis (**Figure 5H**). These changes included SHP-2 (Ptpn11), as well as proteins involved in endocytosis (Pag1, Cbl) and immune processes (Lyn, Triobp, Fyb1, Dapp1). Thus, SHP-2 acts as one factor modulating Siglec-F-mediated pTyr signaling activation. Other ITIM-binding factors such as SHP-1 (Ptpn6), Inpp5d/Inppl1, or Pik3r1/2 may also mediate the effects of Siglec-F on pTyr signaling (Liu et al., 2015; Sweeney et al., 2005).

Siglecs activate endocytic and phagocytic responses

We next assessed whether Siglec-F expression could alter microglial function, including endocytosis and phagocytosis. Previous literature has shown that CD22 and CD33 may alter microglial phagocytosis of protein aggregates and cellular debris (Bhattacherjee et al., 2019; Griciuc et al., 2013, 2019; Pluvinage et al., 2019). In contrast, Siglec-F and Siglec-8 have been shown to regulate endocytosis and vesicular trafficking in other cellular contexts (O'Sullivan et al., 2018; Siddiqui et al., 2017; Tateno et

al., 2007; Walter et al., 2007). We tested this endocytic phenotype by co-culturing BV-2 cells that stably express Siglec-F together with empty vector control cells for 24 hours. Cells were then incubated with Fluor 488-conjugated monomeric $A\beta_{1-42}$ and analyzed using flow cytometry (**Figure 6A**). We found that increased Siglec-F expression resulted in Aβ uptake compared to control cells (**Figure 6B**). In contrast, Siglec-F 2xY->F expression did not alter Aβ uptake (**Figure 6C**). We quantified relative fluorophore uptake between Siglec$^+$ and empty vector cells and found that overexpression of Siglec-F, CD33, Siglec-5, and Siglec-8 could all increase cellular uptake of monomeric $A\beta_{1-42}$ (**Figure 6D**). We saw a similar effect using 10 kDa dextran, suggesting this effect is not specific to Aβ (**Figure 6E**). Finally, we tested 1 µm fluorescent beads which can differentiate small scale endocytic events from phagocytosis. We found that overexpression of all four Siglecs could increase bead uptake, while 2xY->F showed the same level of uptake as empty vector (**Figure 6F**).

To show that these molecules were not binding to the surfaces of cells, we examined the uptake of pHrodo-tagged Dextran which fluoresces only at low pH within cellular lysosomes. BV-2 cells stably expressing Siglec-F showed increased pHrodo fluorescence intensity relative to 2xY->F cells (**Figure 6G**). Using this system, we found that SHP-2 inhibitor SHP099 was able to inhibit pHrodo Dextran uptake at concentrations >500 nM (**Figure 6H**). Up to 2.5 µM SHP099 did not have an effect on the growth rate of control cells expressing 2xY->F receptors, however it appeared to further decrease the proliferation of Siglec-F-expressing cells (**Figure 6I**). Together, this data and previous literature supports the case that Siglec-F drives an endocytic response via SHP-2 signaling, downregulating its own activation and trafficking substrates to endolysosomal vesicles for degradation.

Discussion

Cross-model phosphoproteomics link signaling changes to AD pathologies

In this study, we sought to identify signaling pathways that are dysregulated in various mouse models of neurodegeneration using quantitative phosphoproteomics. Using mass spectrometry, we have quantified the phosphoproteomes of CK-p25 (Cruz et al., 2003, 2006; Fischer et al., 2005), 5XFAD (Oakley et al., 2006), and Tau P301S mice (Yoshiyama et al., 2007). We used a sensitive sample enrichment strategy that allowed for quantitative analysis of the low-abundance pTyr peptides from hippocampal and cortical tissues. Extensive signaling alterations were observed in all three models, linking AD pathologies to specific signaling pathway changes. Most importantly, we identified a common response involving Siglec-F and Inpp5d that we predicted to be linked to microglia using published cell-type specific RNA-seq (Zhang et al., 2014, 2016) and single cell RNA-seq datasets (Keren-Shaul et al., 2017; Mathys et al., 2017).

Siglec-F's role in regulating microglial activation

Our work here indicates that human Siglec-8 and mouse Siglec-F receptors are upregulated on a subset of reactive microglia in AD patients and across various models of neurodegeneration. Using an integrative phosphoproteomics approach, we identified phosphorylation on Siglec-F in three mouse models of neurodegeneration. We found that Siglec-F was upregulated on a subset of microglia at an early stage of disease progression in CK-p25 and 5XFAD mice. The human paralog, Siglec-8, was also found to be upregulated in aged individuals and in patients with late-onset AD. Using *in vitro* models, we found that IFNγ stimulation upregulates Siglec-F and Siglec-8. These results support a model in which the expression of Siglec-F and Siglec-8 changes on microglia during neurodegeneration and aging, potentially altering microglial inflammatory activity.

One primary phenotype that we found to be associated with Siglec-F expression on BV-2 cells was the induction of cell death. We found that this effect was dependent on Siglec-F substrate-binding and ITIM phosphorylation. Our transcriptomic data suggests that Siglec-F triggers cell death via a pro-inflammatory pathway involving activation of the inflammasome and pyroptosis. Previous work on Siglec-F and Siglec-8 has shown that antibody engagement of these receptors causes a pro-apoptotic response in eosinophils, making them a potential drug target for asthma (Kiwamoto et al., 2012; Zimmermann et al., 2008). In contrast, genetic knock-out of Siglec-F leads to increased inflammation in asthma due to impaired apoptosis in eosinophils expressing Siglec-F (Aran et al., 2019; Engblom et al., 2017; Kiwamoto et al., 2015). One unanswered question in defining the role of Siglec-F and Siglec-8 in neurodegeneration is whether this pyroptotic response is acting as a "brake" on neuroinflammation by reducing the number of microglia or if it is adding fuel to the fire by increasing pro-inflammatory cytokine production. The development of brain-penetrant antibodies or bioconjugates targeting Siglec-F may allow for acute depletion of reactive microglia. Our work here suggests also that targeting signaling pathways downstream of Siglec-F may reduce neuroinflammation associated with chronic receptor activation.

Previous works characterizing the genetics of Siglecs suggest that an AD-protective allele in CD33 improves the microglial response during neurodegeneration (Bradshaw et al., 2013; Chan et al., 2015; Griciuc et al., 2013, 2019; Naj et al., 2011; Siddiqui et al., 2017). CD22 (Siglec-2) was also identified as an anti-phagocytic receptor that was upregulated on aging microglia (Pluvinage et al., 2019). Other than CD22 and CD33, there has not yet been a careful analysis of the effects of other Siglec receptors on microglia. Genetic studies of Siglec-8 have identified several variants associated with higher risk for asthma (rs36498, rs10409962, and rs11672925), but these mutations have not yet been linked to microglial function (Angata, 2014; Gao et al., 2010). Beyond these three genes, there remains many open questions about the Siglec family. Do these receptors play redundant roles? What ligands does each receptor respond to? And how do each of these responses fit into the larger picture of Alzheimer's disease progression? By answering these questions, we may be able to improve future therapeutic design strategies targeting Siglec function.

Author Contributions

N.M., L.-H.T., and F.W. designed the study. A.N., L.A.W., N.M., L.A.A., and P.-C. P. performed animal tissue dissections. D.M. collected human brain tissue samples. N.M. collected proteomics data sets. N.M. wrote proteomics data integration software. N.M. and B.A.J. designed enrichment algorithms. N.M. and L.A.A. performed histology analysis. N.M., W.T.R., and J.P. developed and ran iMGL assays. N.M, F.H.R., and L.L. cloned DNA constructs and performed BV-2 cell assays. N.M., F.W., and L-H.T. wrote the manuscript.

Acknowledgements

We thank members of the White and Tsai laboratories for numerous discussions and feedback. We also thank C. Whittaker for help with RNA-seq analysis, J. Cheah for help with BV-2 assay development and screening, and R. Ahn for discussions on signal transduction mechanisms. N.M. was partially supported by the NIH Biotechnology Training Grant T32GM008334. D.M. was supported by NIRG-15-321390, and Arizona Alzheimer's Consortium. This work was supported by the Center for Precision Cancer Medicine at MIT, NIH grants U54-CA210180, R37-NS051874, RF1-AG054321, a grant from the Simons Center for

the Social Brain, the Glenn Foundation and NDC Belfer (The Neurodegeneration Consortium, The Robert A. and Renee E. Belfer Family Foundation, and the Oskar Fisher Project) to L-HT.

Declarations of Interest

The authors declare no competing interests.

Figures

Figure 1. **Cross-model phosphoproteomics analysis identifies changes in signaling pathways.**

(A) Workflow showing phosphopeptide enrichment strategy. Brain regions were dissected from mice and then processed into proteolytic peptide digests and labeled for quantification with TMT. Phosphopeptides were then enriched and analyzed by liquid chromatography followed by tandem-mass spectrometry.

(B-C) Heatmaps of enriched hippocampus phosphotyrosine peptides in hippocampus tissue from (B) CK-p25 and (C) 5XFAD animal mice. Colors indicate fold change relative to control animals on a log2-scale. Row colors (left) indicate peptides from predicted cell-type specific proteins. Green = Astrocyte, Orange = Neuron, Blue = Microglia, Purple = Oligodendrocyte.

(D) Phosphosite enrichment analysis of phosphopeptides from CK-p25, 5XFAD, and Tau mice. Circle colors indicate normalized enrichment scores (NES) and sizes indicate the number of observed sites in each substrate phospho-set within each mouse model. Kinases enriched in at least one model are shown.

(E) Heatmap showing enriched hippocampus phosphotyrosine peptides from 6 m.o. Tau P301S animals. Legend is same as (B).

(F-G) Relative abundances across all tissues for phosphotyrosine peptides: (F) SVyTEIK (Siglec-F pY561); (G) LyDFVK (Inpp5d pY868). ns, not significant ($p > 0.05$); **$p < 1e-2$; ***$p < 1e-3$; ****$p < 1e-4$.

Figure 2. **Siglec-F and Siglec-8 are upregulated in microglia across models of neurodegeneration.**

(A) Immunofluorescence (IF) staining showing Siglec-F and Iba1 localization in hippocampus CA3 region of 3wk induced CK (top) or CK-p25 (bottom) mice. Scale bars = 50 µm. Colors are: Magenta = Iba1, Cyan = Siglec-F. Images are 60x super-resolution max z-stack projections taken from coronal slices.

(B-C) Percent area coverage of (B) Iba1 and (C) Iba1-proximal Siglec-F between CK and CK-p25 mice across hippocampal regions. Values are calculated from 20x z-stack images (n = 4-5 animals / genotype).

(D-E) IF staining of Siglec-F and Iba1 in (D) 5XFAD 2 m.o. hypothalamus (HY) and (E) 5XFAD 6 m.o. dentate gyrus (DG). Yellow = Aβ from methoxy X04 (D) or D54D2 (E). Scale bars = 50 µm.

(F) Percent area coverage of Iba1-proximal Siglec-F relative to total Iba1 across all analyzed thalamic, cortical, and hippocampal regions of 6 m.o. WT (non-Tg) and 5XFAD mice (n = 3-4 animals / genotype).

(G) Percent area coverage of Siglec-F localized to Iba1 compared to total Aβ plaque volume in each field of view across all analyzed images from 5XFAD and non-Tg control mice. Linear regression R^2 value is shown for images with ≥10 μm^2 total amyloid volume.

(H) Cumulative distribution function (CDF) of the distance between Siglec-F^+ and $Iba1^+$ mask voxels and nearest Aβ plaques in 6 m.o. 5XFAD mice. Each value in the CDF represents the mean distance calculated from a single z-stack of a ROI containing ≥ 1 plaque of size ≥10 μm^2. n = 55 images from 4 animals.

(I-J) Relative RNA abundances for Siglec-8 in (H) hippocampus and (I) posterior cingulate cortex post-mortem patient tissue. Linear regression R^2 values are shown on plots.

(K) IF staining showing Siglec-8 and Iba1, and MHC-II in cortical white matter tissue from a patient with late-onset AD (20x wide-field; Case ID: 01-43). Scale bars = 50 µm. Images are 60x super-resolution max z-stack projections.

(L-M) Percent area coverage of Siglec-8 localized to Iba1 or MHC in individuals with non-AD or AD (n = 1 ND, 3 early-onset, 4 late-onset; n ≥ 5 z-stack images / individual). In (K) each point represents one WM or GM region average from each individual. In (L) values and statistics are shown for each image analyzed. Boolean mask operators indicate: ° = mask dilation, ⋂ = intersection, ⋃ = union, NOT = inverse mask.

Figure 3. **Siglec-F and Siglec-8 are upregulated in BV-2 cells and iMGLs by IFNγ stimulation.**

(A) Flow cytometry quantification of BV-2 Siglec-F expression levels. Cells were cotreated with 0-10 ng/mL IFNγ and 0-10 µM tofacitinib. Values are mean fluorescence intensities (MFI) for n = 4 biological replicates / condition.

(B) IF staining of iMGLs treated with IFNγ. Siglec-8 fluorescence is only shown on non-nuclear (Hoechst 33342$^-$) regions. Images are 60x super-resolution max z-stack projections. Colors are: Red = Iba1, Green = Siglec-8, Blue = 33342. Scale bars = 20 µm.

(C) Quantification of Siglec-8 on iMGLs treated with PBS or 25 ng/mL IFNα, IFNβ, or IFNγ. Values are mean Siglec-8 intensity values from Iba1$^+$;33342$^-$ regions (n = 4 wide-field images from n = 2 replicates / condition).

(D) Quantification of Siglec-8 on iMGLs treated ± 25 ng/mL IFNγ and 5 µM tofacitinib. Legend is same as (C).

Figure 4. **Siglec-F and related human Siglecs drive a pro-inflammatory response in BV-2 cells.**

(A) Confluency doubling times quantified from BV-2 cells with stable retroviral expression of Siglec-F and related human Siglec constructs. Plots indicating doubling time (normalized to 2xY->F constructs) estimated from Incucyte bright-field images (n=3-6 replicates / condition). Shown are cells grown in media alone or media + 50 mU sialidase (+SA). Top bars indicate comparisons between cell lines ±SA, lower bars indicate comparisons between each cell line and its respective 2xY->F control line.

(B) Flow cytometry quantification of cell live / dead markers Annexin-V and propidium iodide on BV-2 cells with stable retrovirus expression of Siglec-F constructs. % parent values are shown for early apoptotic (Annexin-V$^+$;PI$^-$), late apoptotic (Annexin-V$^+$;PI$^-$), and necrotic (Annexin-V$^-$;PI$^+$) populations.

(C) Confluency doubling times quantified from BV-2 cells with dox-inducible expression of Siglec-F constructs. Plots indicating doubling time (normalized to 2xY->F constructs) estimated from Incucyte bright-field images (n=3 replicates / condition).

(D) Selected gene expression changes (top) and enriched gene sets (bottom) taken from RNA-seq analysis of BV-2 cells with stable retroviral expression of Siglec constructs, 2xY->F, and empty vector controls. Heatmaps share a colormap range of 0.25 to 4 for z-score values (top), normalized enrichment scores (NES, bottom).

(E) Quantification and overlap of differentially expressed genes (DEGs) between each Siglec-expressing BV-2 cell line. DEGs were calculated for each Siglec gene compared to respective 2xY->F mutants (upregulated: $p < 1e\text{-}8$, $FC > 1.5$; downregulated: $p < 1e\text{-}8$, $FC < 0.66$).

(F) Expression levels of C1qa, IL-1β, and β-actin by qPCR analysis in BV-2 cells with inducible Siglec-F expression after 48 hours of treatment with 500 ng/mL doxycycline. Fold Change values are equal to $2^{\Delta\Delta Cq}$ normalized relative to GADPH mRNA levels.

(G) Western blot showing pro-IL-1β and β-tubulin in BV-2 cells induced to express Siglec-F at 0 and 48 hours.

Figure 5. **Siglec-F perturbs phosphotyrosine signaling pathways in BV-2 cells.**

(A) Experimental design for phosphotyrosine analysis of BV-2 cells with stable expression of Siglec and corresponding 2xY->F mutants. Samples were run as three 10-plex experiments: (1) Siglec-F: WT vs. 2xY->F; (2) Siglec-F, CD33, Siglec-5, and Siglec-8: WT vs 2xY->F; (3) Siglec-F: WT vs. 2xY->F ± 1 μM SHP099. Phosphotyrosine peptides were enriched and analyzed by LC-MS/MS.

(B-C) Volcano plots showing phosphotyrosine peptides that were (B) increased or (C) decreased after Siglec-F expression. Plots show Siglec-F compared to 2xY->F mutant data integrated across all three runs. Protein names are shown for altered peptides. Labels are only shown for peptides with maximum directional change from each protein. Labels colored according to GO terms: magenta = signal transduction, red = endosome, cyan = cell adhesion, yellow = cytoskeleton, green = metabolism.

(D) Heatmap showing phosphosites in CK-p25 which overlapped in their directional change with BV-2 Siglec-F-associated sites. Colors indicate fold change relative to 2xY->F controls.

(E-F) Heatmap showing phosphosites from CD33, Siglec-5, and Siglec-8 overexpression that were (E) increased or (F) decreased with Siglec expression and shared their directional change with Siglec-F. Siglec-F column indicates average of all untreated Siglec-F replicates. Color scale is same as (D).

(G) Western blot quantification of myc, SHP-2, and SHP-1 from myc co-IP eluates. Co-IP lysates were prepared from BV-2 cells stably expressing Siglec-F and optionally treated with 1 μM SHP099.

(H) Heatmap showing phosphosites that were perturbed by SHP099 treatment. Color scale is same as (D).

Figure 6. **Siglec-F expression drives an endocytic response in BV-2 cells.**

(A) Schematic showing experimental setup to measure rates endocytosis in BV-2 cells. Control (MIP empty vector) cells were plated together with cells stably expressing different Siglec constructs. Cells are allowed to adapt to the same media environment for 24 hours, then fluorophores are added to media. Cells with endocytosis substrates (Aβ, Dextran) were assayed after 3 hours, while phagocytosis substrates (FluoSpheres) were assayed after 24 hours. Populations are separated and relative uptake is measured using flow cytometry.

(B-C) Flow cytometry quantification of fluorescent monomeric Aβ uptake and Siglec-F expression for (B) Siglec-F and (C) Siglec-F 2xY->F. Siglec-expressing cells were plated with empty vector control cells in the same well alongside fluorescent substrates.

(D-F) Quantification of relative mean fluorescence intensities (MFI) between empty vector and Siglec-expressing populations. Relative values are shown for each mouse and human Siglec construct for uptake of (D) monomeric Aβ, (E) 10,000 MW Dextran, and (F) 1 μm FluoSpheres. Each condition consists of 6 biological replicates.

(G) pHrodo Dextran uptake in BV-2 cells with stable expression of Siglec-F estimated by Incucyte measurements.

(H) pHrodo dextran uptake in BV-2 cells stably expressing Siglec-F with 0 - 2.5 μM SHP099 treatment. Data is from the same experiment as (G).

(I) Confluency doubling times for BV-2 cells with stable expression of Siglec-F with 0 - 2.5 μM SHP099 treatment. Data is from the same experiment as (G).

Supplementary Figures

Figure S1. **Accessory analyses of mouse model phosphoproteome changes.**

(A) Volcano plots showing changed phosphopeptides in CK-p25 mice. All tissues and time points are considered together for fold change and p-value calculations. Protein names are shown for changed peptides. Labels are only shown for peptides with maximum directional change from each protein. Labels are colored by predicted cell-type specific protein. Green = Astrocyte, Orange = Neuron, Blue = Microglia, Purple = Oligodendrocyte, Salmon = Endothelia.

(B) Unique and overlapping peptides that are upregulated (FC > 1.25, p < 1e-2) or downregulated (FC < .8, p < 1e-2) within each mouse model. Venn colors are: Red = CK-p25, Purple = 5XFAD, Yellow = Tau P301S.

(C) Heatmap showing phosphotyrosine peptides from the cortex of CK-p25 animals. Colors indicate fold change relative to control animals on a log2-scale. Row colors (left) indicate peptides from predicted cell-type specific proteins using the same scheme as (A).

(D) Correlation between phosphopeptide fold changes in the hippocampus and cortex of 2wk CK-p25 mice. Linear regression R^2 value is shown on plot.

(E) Cell-type enrichment analysis of phosphopeptides from CK-p25, 5XFAD, and Tau animals. Heatmap colors indicate LOE of cell-type specific proteins in the set of upregulated or downregulated phosphopeptides for each animal. Cell types are: Ast = Astrocyte; End = Endothelia; Oli = Oligodendrocyte, Mic = Microglia, Neu = Neuron.

(F) Phosphorylation motif logos for enriched peptides from the upregulated (FC > 1.25, p < 1e-2) pSer/pThr phosphoproteome of CK-p25 mice. Y-axis shows log-odds enrichment (LOE) of amino acids proximal to phosphorylation sites.

Figure S2. **5XFAD phosphoproteome accessory analyses.**

(A) Volcano plots showing changed phosphopeptides in 5XFAD animals. All tissues and time points are considered together for fold change and p-value calculations. Protein names are shown for changed peptides. Labels are only shown for peptides with maximum directional change from each protein. Labels are colored by predicted cell-type specific protein. Orange = Neuron, Blue = Microglia, Salmon = Endothelia.

(B) Quantification of transgenic amyloid precursor protein peptides identified in the hippocampus and cortex from 5XFAD and WT mice: HFEHVR and LVFFAEDVGSNK. APP / App indicates peptides mapped to both transgenic and native protein. NTF: N-terminal Fragment, $A\beta_{n-m}$: peptide mapped within Aβ.

(C) Heatmap showing enriched phosphotyrosine peptides in the cortex of 9 mo 5XFAD mice. Colors indicate fold change relative to control animals on a log2-scale. Row colors (left) indicate peptides from predicted cell-type specific proteins using the same scheme as (A).

(D) Correlation between phosphopeptide fold changes in the hippocampus and cortex of 9mo 5XFAD mice. Linear regression R^2 value is shown on plot.

(E) Phosphorylation motif logos for enriched peptides from the downregulated (FC < .8, p < 1e-2) pSer/pThr phosphoproteome of 5XFAD mice. Y-axis shows log-odds enrichment (LOE) of amino acids proximal to phosphorylation sites.

(F) Phosphopeptides associated with Δp35KI mutation in 5XFAD mice. Heatmap colors indicate log2 fold changes from hippocampus tissue. Row colors (left) indicate the number of residue positions for which peptides match the CaMKII motif: O.+Q.xO -, where 'O' indicates hydrophobic residues (FLMVI), '+' indicates positively charged residues (KR), 'x' indicates a phosphosite, and '.' indicates any residue. 'x' and '.' are uncounted for motif scores.

Figure S3. **Tau P301S phosphoproteome and validation analyses.**

(A) Volcano plots showing changed phosphopeptides in Tau P301S mice. All tissues and time points are considered together for fold change and p-value calculations. Protein names are shown for changed peptides. Labels are only shown for peptides with maximum directional change from each protein. Labels are colored by predicted cell-type specific protein. Orange = Neuron, Blue = Microglia.

(B) Heatmap showing enriched phosphotyrosine peptides in Tau P301S 4mo hippocampus tissues. Colors indicate fold change relative to control animals on a log2-scale. Row colors (left) indicate peptides from predicted cell-type specific proteins using the same scheme as (A).

(C) Transgenic MAPT peptides identified in Tau P301S mice. Colored bars indicate directional changes for non-phosphorylated peptides. Red = increased, blue = decreased, grey = unchanged, light-grey = only phosphopeptides were seen in that region. Colored circles indicate phosphorylation sites that were quantified. Red circle = increased, blue circle = decreased, black circle = unchanged.

(D) Correlation between phosphopeptide fold changes in hippocampus tissues of 4mo and 6mo Tau P301S mice. Linear regression R^2 value is shown on plot.

(E-F) Validated peptide-spectrum matches for (E) Siglec-F pY561 (SVyTEIK) and (F) Inpp5d pY868 (LyDFVK) in CK-p25 mice. Green circles indicate predicted fragment ions. Red circles indicate abundant peaks that were not assigned a fragment ion. Orange box indicate precursor isolation window.

Figure S4. **Siglec-F IF antibody validation and regional scanning.**

(A) Validation of E50-2440 antibody on BV-2 with stable Siglec-F expression. Top: Empty vector; Bottom: Siglec-F 2xY->F. Blue = 33342, Red = E50-2440. Scale bars = 20 µm distance.

(B) Immunofluorescence (IF) staining showing Siglec-F and Iba1 localization in CK-p25 3wk hippocampus tile scan view. Boxed regions indicate analyzed regions: DG, CA1, CA2, and CA3. Scale bars = 50 µm distance. Colors are: Magenta = Iba1, Cyan = Siglec-F. Images are max z-stack projections taken from coronal slices.

(C) Individual wide-field images of DG, CA1, CA2, and CA3 regions from CK (top) and CK-p25 mice (bottom).

(D-E) Percent of total Siglec-F mask (D) area and (E) signal intensity that overlaps with Iba1 masks that have been dilated by a variable number of pixels. ° indicates Iba1 mask was dilated prior to Boolean overlap calculation. 1 voxel ≅ 2.4 µm. Values are calculated from CA1, CA2, CA3, and DG image regions from CK-p25 animals using the same image set as **Figure 1C**.

(F) Wide-field image of Siglec-F, Iba1, and Aβ (Methoxy X04) signal across in the thalamus (TH) of 6 m.o. 5XFAD mice.

(G-H) Percent of total Siglec-F mask (G) area and (H) signal intensity that overlaps with Iba1 masks that have been dilated by a variable number of pixels. Legend is same as (D-E). Values are calculated from thalamic, cortical, and hippocampal regions from 5XFAD animals using the same image set as **Figure 2F**.

Figure S5. **Siglec expression patterns in microglial scRNA-Seq and bulk RNA-seq datasets.**

(A) Reanalysis of Siglec expression patterns in CK-p25 microglia (Mathys et al., 2017). Expression levels were imputing using MAGIC (van Dijk et al., 2018) and plotted using the tSNE coordinates from the original publication. Late response MHC-II^{+} microglia (top cluster, marker genes: H2-Ab1, Cd74) show increased Siglec-F expression compared with homeostatic microglia (lower right cluster).

(B) Reanalysis of Siglec expression patterns in 5XFAD microglia (Keren-Shaul et al., 2017). Expression levels were projected onto two dimensions using UMAP (McInnes et al., 2018) and imputed using MAGIC (van Dijk et al., 2018). Disease-associated microglia (lower center, marker genes: Cst7, Lpl) show increased Siglec-F expression compared with homeostatic microglia (center).

(C-D) Relative RNA abundances for Siglec-8 in (C) entorhinal cortex and (D) superior frontal gyrus post-mortem patient tissue. Blue = ND; Yellow = MCI; Green = AD. Linear regression R^2 and p-values are shown on plots.

Figure S6. **Siglec-8 IF antibody validation and accessory analyses.**

(A) IF staining for Siglec-5 (top) and Siglec-8 (bottom) in late-onset AD patient tissue (LOAD; Case ID: 03-06). Show are merge (Left; Red = Iba1, Green = Siglec, Blue = 488 background autofluorescence), background-corrected merge (Middle; Red = Iba1, Green = Siglec / 488 background), and background-corrected Siglec alone (Right). Scale bars = 50 µm distance.

(B) Antibody validation of ab198690 on BV-2 with induced Siglec-8 (48 hours dox). Top: Siglec-8; Bottom: Siglec-8 2xY->F. Blue = Hoechst 33342, Red = ab198690. Scale bars = 20 µm distance.

(C-E) Representative IF images for Iba1, Siglec-8, MHC-II, and Aβ (Methoxy X04) in tissue from patients. Shown are: (C) white matter (WM) region of a LOAD patient (Case ID: 01-43); (D) grey matter (GM) region from a LOAD patient (Case ID: 03-06); and (E) GM region from an early-onset AD patient (Case ID: 00-22).

(F-G) Percent of total Siglec-8 mask (F) area and (G) signal intensity that overlaps with Iba1, MHC, and the union (U) of Iba1 and MHC. ° indicates mask were dilated in by a given number of pixels prior to Boolean overlap calculation. 1 voxel ≅ 2.4 µm. Values are median stack values from n=3 selected 20x wide-field images.

(H) Percent area coverage of Siglec-8 localized to Iba1 or MHC in grey matter (GM) and white matter (WM) across all analyzed images.

(I) Percent area coverage of Siglec-8 localized to Iba1 compared to total Aβ volume in each field of view across all analyzed images. Linear regression R^2 value is shown for images with ≥10 µm^2 total amyloid volume.

Figure S7. **BV-2 and iMGL IFNγ and tofacitinib accessory experiments.**

(A-C) Incucyte (A) object count, (B) object size, and (C) doubling time for BV-2 cells treated with 1-100 ng/mL IFNγ. (A+B) are calculated at 20 hours while (C) is calculated from confluency changes between 30 and 60 hours.

(D-E) Incucyte (D) object count and (E) object size for BV-2 cells co-treated with 10 ng/mL IFNγ and 0-5 μM tofacitinib.

(F) 20x wide-field images of iMGLs treated with IFNγ or PBS and tofacitinib. Siglec-8 fluorescence is only show on non-nuclear regions. Colors are: Red = Iba1, Green = Siglec-8, Blue = Hoechst 33342. Scale bars = 100 μm.

(G) qPCR quantification of Siglec-8 from iMGLs treated with 25 ng/mL IFNγ or PBS.

(H) Quantification of Siglec-8 on iMGLs treated with IFNγ or PBS and tofacitinib. iMGLs were matured with TGFβ before IFNγ stimulation.

Figure S8. **BV-2 Siglec expression accessory data.**

(A) Incucyte object count for BV-2 cells expressing inducible Siglec-F constructs. Cell counts for are normalized to the starting count in each imaging region.

(B-C) Incucyte quantification of (B) object count and (C) confluency doubling time for BV-2 cells expressing inducible Siglec-F and optionally co-treated with 20 μM Bestatin.

(D) Western blot detection of Siglec-F-myc, pERK1/2, total ERK, and β-tubulin in BV-2 cells induced to express Siglec-F for 0-72 hours.

(E) Quantification of Erk1, Erk2, pErk1 / total Erk1, and pErk2 / total Erk2 for bands shown in (D).

(F) Western blot detection of myc-tagged Siglec-F +/- PNGase.

(G) Volcano plot showing proteomic changes induced by stable Siglec-F expression in BV-2 cells. Only proteins with ≥ 2 unique peptides that each were seen in ≥ 2 scans are shown.

(H) Quantification of Siglec-F pY561 (SVyTEIK) across BV-2 lines analyzed.

Supplementary Data

Table S1. **Mouse Phosphoproteomics Sample Info and Peptide Data.** Full table of tissues analyzed, MS runs, peptide quantification values across each mouse model analyzed. Table includes separate tabs for CK-p25, 5XFAD, and Tau P301S data sets. Each tab includes fold change and p-values for comparisons between animal groups.

Table S2. **Human Sample Info**. Clinical histopathology measurements of human tissue.

Table S3. **BV-2 RNA-seq Data.** Full table of mRNA changes after stable Siglec expression in BV-2 cells. Table includes tabs for DEGs list and GSEA analysis.

Table S4. **Processed BV-2 Peptide Data.** Full table of peptide quantification values across BV-2 stable Siglec expression lines analyzed. Table includes separate tabs for phosphotyrosine and proteome data

sets. Each tab includes columns with fold change and p-values comparing between groups: (1) Siglec-F vs all 2xY->F; (2) CD33, Siglec-5, Siglec-8 vs all 2xY->F; (3) Siglec-F + SHP099 vs Siglec-F.

STAR Methods

LEAD CONTACT AND MATERIALS AVAILABILITY

Further information and requests for resources and reagents should be directed to and will be fulfilled by the Lead Contact, Forest M. White (fwhite@mit.edu). Plasmids were produced in our laboratory and are available upon request to the Lead Contact with a completed Materials Transfer Agreement.

EXPERIMENTAL MODEL AND SUBJECT DETAILS

Mouse models

All animal work was approved by the Committee for Animal Care of the Division of Comparative Medicine at the Massachusetts Institute of Technology. The mouse models of AD used in this study were: (1) double transgenic CK-p25 (Cruz et al., 2003, 2006; Fischer et al., 2005), CK control (aged 3-4 m.o., induced for 2-7 weeks by removal of doxycycline from diet); (2) 5XFAD (Oakley et al., 2006); 5XFAD Δp35KI$^{+/+}$ (Seo et al., 2014), WT, WT Δp35KI$^{+/+}$ (9-11 m.o.); (3) Tau P301S (Yoshiyama et al., 2007) Tg and WT; (4) Young and aged C67BL/6J (2-3 m.o.; 13-14 m.o.). Mice were housed in groups of three to five on a standard 12 h light/12 h dark cycle, and all experiments were performed during the light cycle. Food and water were provided ad libitum. Only male mice were used for the phosphoproteomics analyses with the exception of CK/CK-p25 mice that were induced for 7wk. Both male and female mice were used for IF experiments. The full list of each mouse ID, sex, genotype, and age used for proteomics is listed in **Supplementary Table 1**.

Cell culture models

Human embryonic kidney (HEK) 293T cells were from ATCC and cultured in DMEM containing 10% FBS and 1% Pen/Strep (Thermo). BV-2 cells were immortalized from a female C57BL/6 mouse background (Blasi et al., 1990) and cultured in RPMI 1640 medium with GlutaMAX supplemented with 10% FBS, and 1% Pen/Strep. BV-2 were maintained at ~1-50% confluency and split every 3-4 days to avoid activation from overcrowding**.** All cells were incubated at 37°C with 5% CO_2. No mycoplasma contamination was detected in cell lines used in this study.

BV-2 cells stably expressing Siglec constructs were generated using retroviral vectors comprising a MSCV promoter and IRES-puro module (Hynes lab). Retroviral particles were packaged by transfecting 293T cells with MIP constructs, pCMV-VSV-G, and pUMVC packaging vectors. BV-2 cells were transduced for 6-8 hours by co-incubation with 1 mL virus aliquots and 4 µg/mL polybrene. Transduced cells were selected after 24 hours using 2 µg/mL puromycin for 2-3 days.

BV-2 cells with inducible Siglec expression were generated using lentiviral vectors comprising a TRE promoter alongside a UbC promoter expressing TetR (rtTA-Advanced) and IRES-neomycin resistance module (pINDUCER20 (Meerbrey et al., 2011)). Lentiviral particles were packaged by transfecting 293T cells with pINDUCER constructs, psPAX2, and pMD2.G 2nd generation packaging vectors. BV-2 cells were transduced for 6-8 hours by co-incubation with 1 mL virus aliquots. Transduced cells were selected after 24 hours using 1 mg/mL G418 for 2-3 days.

iPSC-derived Microglia (iMGLs)

iMGLs were generated from previously characterized APOE e3/e3 patient line (Lin et al., 2018) using a published protocol (Abud et al., 2017; McQuade et al., 2018). iPSC cells were grown in 6-wells on matrigel to 90% confluency and split with ReLeSR. Colonies of 50-200 cells (~200 µm diameter) were

counted and plated onto a matrigel-coated 6-well plate at a density of 100 clumps/well. The next day (day 0), media was changed to 2 mL/well of STEMdiff™ Hematopoietic Kit with Supplement A at 1:200. On day 2, 1 mL of STEMdiff™ with Supplement A was added to each well. On day 3, media was changed to 2 mL/well of STEMdiff™ with Supplement B. On days 5, 7, and 9, 1 mL/well of STEMdiff™ with Supplement B was added to each well. On day 11, non-adherent induced hematopoietic stem cells (iHPSCs) were collected from the media supernatant.

iMGLs were derived from iHPSCs by maturing cells in iMGL Differentiation Base Media (iMBM). iMBM was created by mixing 2x500 mL DMEM/F12, HEPES (1:1), 20 mL ITS-G, 20 mL B27, 5 mL N2, 10 mL Glutamax, 10 mL NEAA, 10 mL Pen/Strep (Gemini), 500 µL insulin, and 35 µL monothioglycerol and straining through a .22 µm filter. iHPCs were spun at 300 g for 5 min and re-plated in a 6-well on matrigel at a density of 200,000 cells/well in 2 mL iMBM with freshly added 25 ng/mL M-CSF, 100 ng/mL IL-34, and 50 ng/mL TGFβ-1. Freshly prepared iMBM was added to cells every other day from days 13-35. On days 23 and 36, media supernatant was collected, centrifuged at 300xg for 5 min, and resuspended in 1 mL fresh iMBM to reduce media volume without cell loss. On day 36 and thereafter, cells were given bi-weekly media changes, supplemented with 100 ng/mL CD200 and 100 ng/mL CX3CL1 to promote microglial maturation. After 2 months, microglia began to adhere to the plate and were split once by gentle washing with PBS for assays.

Human samples

Samples of fixed free-floating brain slice tissue were secured from AD and neurologically normal, non-demented elderly control (ND) brains obtained at autopsy at the Banner Sun Health Research Institute Tissue Bank (BSHRI). The brain bank at BSHRI is one of the world's best, dedicated to the highest standards (average RNA integrity; RIN 8.5) and postmortem interval (2.8 hours) (Birdsill et al., 2011; Walker et al., 2016). Cognitive status of all cases was evaluated antemortem by board-certified neurologists, and postmortem examination by a board-certified neuropathologist resulting in a consensus diagnosis using standard NIH AD Center criteria for AD or ND. Samples analyzed in the current study were collected from 3 male and 5 female human subjects with ages ranging from 60-96 and 60-82 years, respectively. The full list of each ID, sex, age, and diagnostic histopathology measurements for patients is listed in **Supplementary Table 1**.

METHOD DETAILS

Proteomics Sample Processing

Mice were deeply anesthetized in 5% isoflurane after which their cerebral cortex, cerebellum, and hippocampus were dissected while immersed in ice cold PBS. Tissues were snap frozen in liquid nitrogen and stored at -80°C.

Tissues for proteomics analysis was homogenized in 3 mL ice-cold 8 M urea. Lysates were then centrifuged at 4000xg for 30 minutes to clear lipids and DNA. Aliquots were taken for a BCA assay of protein concentration. Lysates were then treated with 10 mM DTT for 1 hour at 56°C, followed by 55 mM iodoacetamide for 1 hour at room temperature, rotating in the dark. Samples were diluted by adding 8 mL Ammonium Acetate pH 8.9 and then digested at room temperature overnight on a rotator with trypsin at a 1:50 ratio of trypsin to total protein mass (1-2 mg total protein expected for hippocampus, 3-4 mg for cerebellum, and 8-10 mg for cortex). This reaction was quenched with 1 mL 99.99% Acetic Acid and samples were desalted using Sep-Pak Lite C18 cartridges for hippocampus and Sep-Pak Plus for cortex and cerebellum samples. Peptides were then dried to half volume in a speed-vac

and post-cleanup concentrations were assayed using a Pierce™ Quantitative Colorimetric Peptide Assay. Peptides were then divided into 130 µg aliquots that were snap-frozen and lyophilized. Peptides were then labeled with 6-plex and 10-plex isobaric tandem mass tags (TMT) according to manufacturer's protocol. Labeled samples were then dried down in a speed-vac overnight. Two or more technical replicates were run for each collection of tissues to improve pTyr coverage.

Phosphotyrosine analysis of BV-2 cells was performed by first transducing cells with MCSV-IRES-Puro retrovirus to generate stable Siglec expression lines. 4 days after transduction, cells were split into 10 cm dishes with 1 million cells/dish in 10 mL of fresh RPMI media. 1 µM SHP099 was added to cells 24 hours before lysis. Cells were lysed after 48 hours in ice-cold 8 M urea. Peptides with TMT 10-plex labels were prepared following the same protocol as mouse brain tissue above.

Phosphopeptide enrichment and LC-MS/MS Analysis

Tyrosine phosphorylated peptides were enriched by a two-step process consisting of an immunoprecipitation (IP) with two pan-specific anti-phosphotyrosine antibodies (4G10, PT66) followed by immobilized metal affinity chromatography (IMAC) as previously described (Gajadhar et al., 2015; Johnson and White, 2012; Johnson et al., 2012; Reddy et al., 2016; Wolf-Yadlin et al., 2006). IP supernatants were subjected to a second round of IP with anti-pSer/pThr motif antibodies (MPM-2; 34B2) followed by IMAC cleanup step. IP supernatants were then divided into 80 fractions using high pH reverse phase chromatography on a ZORBAX C18 column. Fractions were concatenated into 20 tubes and dried down. Each fraction was then enriched using commercial Fe-NTA columns. Small amounts of each IP supernatant were saved and diluted 1:1000 in 0.1% acetic acid for global protein expression profiling.

Phosphopeptide-enriched samples were loaded onto a BSA-conditioned pre-column with 10 µm C18 beads. Columns were rinsed with 0.1% acetic acid to remove excess salts and attached to an analytical column with 10 cm of 5 µm C18 beads. Agilent 1100 Series HPLCs were operated at 0.2 mL/min flow rates with a pressure-restricted T-junction to attain nanoliter flow rates. Peptides were eluted with increasing concentrations of buffer B (70% acetonitrile, 0.1% acetic acid) using the gradient settings: 0-13% (10 min), 13-42% (95 min), 42-60% (10 min), 60-100% (7 min), 100% hold (6 min), 100-0% (2 min). Global phosphoproteome and proteome fractions were analyzed using an EASY-nLC nano-flow UHPLC. Fractions were eluted using the gradient settings: 0-10% (10 min), 10-30% (100 min), 30-40% (14 min), 40-60% (5 min), 60-100% (2 min), hold 100% (10 min), 100-0% 2 min. Peptides were ionized by electrospray ionization (ESI) at 1 - 3 kV.

Peptides were then analyzed by LC-MS/MS on a QExactive Plus and QExactive HF-X Orbitrap mass spectrometer operating in data-dependent mode acquiring MS scans and HCD MS/MS fragmentation spectra. Ions with charge >1 were dynamically selected for fragmentation using a top-20 untargeted method with an exclusion time of 30s. The maximum injection time and ACG targets were set to 50 ms and 3e6 respectively. MS scans were captured with resolution = 60,000 and MS2 scans with resolution = 45,000. Peptides were fragmented with the HCD normalized collision energy set to 33%. Protein expression profiling was performed on LTQ Orbitrap or QExactive Plus instruments.

Immunohistochemistry and microglia imaging analysis

For hippocampus slice analysis, mice were perfused transcardially with PBS followed by 4% paraformaldehyde (PFA) to fix tissue. Brains were then dissected and post-fixed with 4% PFA overnight.

The tissue was then sliced into 40 µm sections using a Leica VT100S vibratome and stored in PBS at 4°C. Antigen retrieval was performed on human fixed free-floating tissue by washing glycerol-preserved slices three times with TBST, boiling samples for 10 minutes at 95°C in 10 mM citric acid, 0.05% Tween 20, pH 6, and then washing twice with TBST. Brain slices were blocked and permeabilized in 10% Normal Donkey Serum (NDS), 0.2% Triton-X100 for 1 hour. Blocked slices were then incubated with primary antibody for 1-2 days at 4°C. The following antibodies were used for primary staining: α-MHC-II (CR3/43; 1:100); α-Iba1 (polyclonal; 1:500); α-Siglec-F (E50-2440; 1:100); α-Siglec-8 (ab198690; 1:50). Slices were washed three times with PBS with shaking for 5 minutes between washes. Slices were then stained with secondary antibody (donkey host, 1:500), and Methoxy-X04 (100 µM) to stain plaques or Hoechst 33342 (1:10,000) to stain nuclei. Slices were treated with 1X TrueBlack for 30 seconds after immunostaining and then washed 3 times in PBS to reduce autofluorescence signal. All tissue slices shown and analyzed were treated with TrueBlack with the exception of the tile scan shown in **Figure S3B**.

Slices were imaged on a Zeiss 880 confocal microscope, using a 20x and 63x objective to generate z-stack images from regions of interest. Images were taken with excitation / emission window filters set up to avoid signal bleed between secondaries (Blue: 405 nm, 410-515 nm; Green: 488 nm, 493-577 nm; Red: 561nm, 585-634 nm; Far-Red: 633 nm, 638-755 nm). Super-resolution images were taken using the AiryScan module through a 20x objective with 3-5x digital zoom.

For antibody validation, BV-2 cells transduced with pINDUCER20-Siglec constructs were plated in a 96-well with 500 ng/mL Doxycycline for 48 hours and then fixed with 4% PFA for 15 minutes and washed with PBS. Cells were stained with α-Siglec-F (E50-2440; 1:100) or α-Siglec-8 (ab198690; 1:100) as well as Hoechst 33342 (1:10,000) to stain nuclei. Cells were imaged on a Zeiss 710 confocal microscope.

Siglec Quantification Assays

BV-2 cells for Siglec-F quantification were assayed by plating 3k cells/well in a 24-well with 1 mL media and optional cytokines added. After 72 hours incubation, cells were assayed by removing media and resuspending cells in ice cold 100 µL flow buffer (PBS + 10% FBS) with APC-Cy7-E50-2440 (1:100) antibodies and PI (1:1000) at 4°C with shaking for 15 minutes in the dark. Cells were washed with flow buffer and immediately analyzed on a BD FACS Canto flow cytometer.

iMGLs for Siglec-8 quantification were assays by plating at 2k cells/well in an 8-well glass slide with 500 µL/well of iMBM and optional cytokines and inhibitors. After 72 hours, cells were fixed for 15 minutes at room temperature with 4% PFA and then blocked and permeabilized for an hour with 5% BSA and 0.3% Triton-X100. Cells were stained with primary antibody (ab198690: 1:100; Iba1: 1:500) overnight at 4°C. Cells were washed twice with PBS and then stained with Alexa-488/Alexa-594 secondary antibodies for two hours. Slides were washed twice with PBS and then then covered with Fluomount G solution and glass coverslip and then imaged on a Zeiss 880 confocal microscope.

Siglec Retroviral Expression

Retrovirus was produced in a 10cm plate of HEK 293T cells beginning at 50-60% confluency. HEK cells were transfected for 24 hours with FuGene, GAG-pol, VSVG envelope, and MCSV-IRES-Puro (MIP) plasmids expressing full length Siglec proteins with C-terminal myc epitope tags and ITIM pTyr sites mutated to phenylalanine. After a 10 mL media change and 24-hour incubation, media supernatants were collected and filtered through a .45 µm filter, divided into 1 mL aliquots, and stored at -80°C.

For pINDUCER dox-inducible lentivirus expression, Siglec genes were first cloned into a pENTR gateway entry vector and then recombined into pINDUCER20 and pINDUCER21 backbones using LR Clonase. Constructs were propagated in Stbl3 cells to stabilize repeat-flanked inserts. 293T cells were plated at 80% confluency and then transfected with pINDUCER transfer vectors, psPAX2, and pMD2.G at a 10:10:5 µg ratio using PEI MAX followed by a 10 mL media change after 16 hours. Media supernatants were collected 72 hours post-transfection, filtered through a .45 µm filter, and stored in 1 mL aliquots at -80°C.

For viral transduction, BV-2 cells were plated at 3k cells/well in a 6-well plate. For MIP-WT Siglec constructs, cells were plated at 20k cells/well due to impaired cell growth during selection. Cells were infected with virus plus 5 µg/mL polybrene for 6-8 hours, followed by a fresh media change. After 24 hours, cells were selected with 2 µg/mL puromycin or 1 mg/mL G418 for 72 hours with daily media changes. Stable Siglec-expressing BV-2 cells were then split using 0.05% Trypsin and then centrifuged twice at 200 g for 3 min and washed with twice with fresh media to remove dead cells before beginning down-stream assays. Inducible Siglec cells were split and frozen in 10% DMSO, 50% FBS, and 40% media. Cells were thawed and left to recover for 3-4 days. All cells were assayed post-infection within 10 days total time in culture to avoid negative selection against viral Siglec expression.

Cell Death Flow Cytometry Assay

To measure apoptosis and necrosis markers, BV-2 cell with stable Siglec construct expression were split into 96-well plates at a concentration of 4k cells/well with each well containing 200 µL of media and left to adhere to the plate overnight. The plate was centrifuged for 3 minutes at 400 x g and 4°C, then the media was aspirated. Cells were resuspended in 50 µL ice cold Annexin V binding/washing buffer with Annexin V-Alexa 488 (1:50) and Propidium Iodide (PI, 20 µg/mL) and incubated in the dark at 4°C for 15 minutes. After incubation, 200 µL of binding/washing buffer was added to each well. Cells were analyzed using a FACS Canto flow cytometer to determine the percentages of early apoptotic (Annexin V^+), late apoptotic (Annexin V^+; PI^+), and necrotic populations (PI^+).

Incucyte Proliferation and Endocytosis Assays

BV-2 cells were plated at 3k cells/well for quantification of proliferation and endocytosis. For proliferation-only assays, treatments were added immediately on plating and cells were monitored for 1-4 days. Cells with inducible Siglec expression were co-treated with inhibitors and 500 ng/mL doxycycline. Cells were incubated for 48 hours in an Incucyte Plate Imager and imaged every 1-3 hours with a 10X objective in the bright-field.

RNA-Seq Data Collection

For RNA-Seq analysis of BV-2 mRNA expression, MIP-expressing cells were plated at 20k cells/well in a 6-well plate with 5 mL media. Cells were lysed after 48 hours in 500 µL TRIzol and pipetted repeated through a P1000 to sheer DNA. RNA was extracted by adding 180 µL chloroform, vortexing for 15 seconds, and then centrifuging at 12,000xg for 15 minutes at 4°C. The top, clear, RNA-containing phase was then transferred to a new tube, mixed 1:1 with 100% Ethanol and purified using a Direct-zol RNA MicroPrep kit. RNA-seq libraries were prepared from 50 ng of RNA using Kapa mRNA Hyperprep Kits. RNA-Seq analyses were performed by The MIT BioMicro Center. Library sequencing was multiplexed on two lanes of a HiSeq 2000 (Illumina) with 40 bp reads.

Quantitative real-time (qRT) - PCR

qPCR analyses were performed on 20k (2xY->F) or 50k (WT Siglec) BV-2 cells plated in a 6-well plate with 5 mL media and optional inhibitors. Inducible Siglec expression cells were treated with 500 ng/mL doxycycline for 48 hours. TRIzol-chloroform RNA was purified using 25 µL of Dynabeads mRNA Direct magnetic poly-T beads per sample. Beads were washed twice with 100 µL A and B wash buffers. mRNA was reverse transcribed into cDNA by adding SuperScript IV VILO Master Mix to beads and incubating in a thermocycler for 10 min at 25°C, 10 minutes at 50°C, and 5 minutes at 85°C. cDNA was then diluted 1:20 in ultrapure water and 2 µL was mixed with iQ SYBR Green Supermix and 500 nM primers for a final volume of 6 µL in a Microseal 384-Well PCR Plate. A CFX384 Touch Real-Time PCR was used for qPCR amplification and melting curves were generated to check each sample for product purity.

Endocytosis Assays

For flow cytometry quantification of endocytosis, we plated 2k Siglec-expressing cells in a 96-well alongside 6k empty vector control cells in 200 µL of media. Cells were allowed to settle overnight and then fluorescent substrates were diluted in PBS and added to each well ($A\beta_{1\text{-}42}$-488: 250 ng/mL; 10 kDa Dextran-488: 250 ng/mL; 1 µm blue-green FluoSpheres: 50 million/mL). Cells were incubated with small endocytosis substrates for 3 hours and larger beads for 24 hours. Well media was aspirated and cells were washed once with PBS and then resuspended in 100 µL flow buffer with α-Siglec antibody (Siglec-F: APC-Cy7 E50-2440, 1:100; CD33: APC WM53, 1:100; Siglec-5: Alexa-647 194128, 1:100; Siglec-8: APC 7C9, 1:100). Cells were washed once with flow buffer and then immediately assayed. Relative fluorophore uptake was calculated as the geometric mean fluorescent signal (MFI) of $Siglec^+$ / $Siglec^-$ populations from each well.

To assay endocytosis of pHrodo ligands, BV-2 cells were plated and then treated the next day with inhibitors for one hour, followed by 5 µg/mL pHrodo Green Dextran (10k MW). Incucyte bright-field, and green fluorescence channels were imaged every 1 hour with a 10x objective. Object fluorescent intensities were then quantified using IncuCyte ZOOM software and exported using the metrics: “Total Object Integrated Intensity (GCU x µm²/Image)”.

Siglec Co-Immunoprecipitation and Western Blot

To perform co-IP experiments, BV-2 cells were plated in 15 cm dishes at a 1 million cells / dish and allowed to grow until they reached 70% confluency. SHP099 was added at 1 µM 24 hours prior to lysis. Cells were lysed in ice cold protein IP buffer (1% NP-40, 150 mM NaCl, 50 mM Tris, 5 mM EDTA, pH 7.4) with HALT protease inhibitors. Lysates were spun at 13,400 rpm at 4°C for 30 minutes to clear lipids and DNA. Protein supernatants were transferred to a new tube and protein concentrations were quantified using a BCA assay. 2 mg of lysate was incubated with 20 µL of myc-sepharose beads overnight at 4°C. Beads were spun down at 6,500 rpm and washed three times with 1 mL protein IP buffer. Proteins were eluted by boiling beads at 95°C for 5 min in LDS Sample Buffer (4X) and 100 mM DTT.

For western blots, BV-2 cells with inducible Siglec constructs were plated in a 10 cm dish at 1 million cells/well in fresh RPMI media with 500 ng/mL doxycycline. Cells were lysed after 72 hours in ice cold RIPA with HALT protease inhibitors. Lysates were cleared, protein concentration quantified, and 50 µg aliquots were prepared by boiling with LDS and DTT as above.

Protein lysates and IP eluates were separated on a 4-12% Bis-Tris SDS-PAGE gel at 90-130 V. Proteins were then transferred to a nitrocellulose or PVDF membranes. Membranes were blocked for 1

hour at RT with Intercept Blocking Buffer and then incubated with primary antibodies: α-Siglec-F (E50-2440: 1:1000), α-myc (9B11: 1:1000), α-SHP1 (C14H6: 1:1000), α-SHP2 (D50F2: 1:1000), α-IL-1β (Polyclonal: 1:1000), α-β-tubulin (1:10,000) overnight at 4°C. Membranes were washed 4x 5 min in TBST. Membranes were incubated with Li-Cor secondary antibodies (1:20,000) for 2 hours at RT and then washed 4x 5 min in TBST and 1x in PBS. Membranes were imaged on a Li-Cor Odessey CLx.

QUANTIFICATION AND STATISTICAL ANALYSIS

Proteomics Data Processing and Integration

Peptide-spectrum matching and quantification was run using Proteome Discoverer and MASCOT. Peptides were searched against the UniProt mouse proteome database (UP000000589, SwissProt Version 2020_01) with a max missed tryptic cleavage count of 2. Tau P301S mice and 5XFAD were also searched against a secondary database containing transgenic human MAPT (isoform E, P301S), APP (isoform C K670N/M671L; I716V; V717I), and PSEN1 (isoform I-463 M146L; L286V) sequences. Precursor and fragment ions were matched with 10 ppm and 20 mmu mass tolerances, respectively. 0.8 Da mass tolerances were used for samples run on the LTQ Orbitrap. Variable modifications were included for phosphorylation (STY), oxidation (M), and TMT (N-term, K). Fixed modifications were set for carbamidomethyl (C). Phosphorylation sites were localized using the ptmRS module with a confidence threshold of 0.75. PSMs for Siglec-F pY561 (SVyTEIK) were manually added to data frames after manually validating spectrum with the correct mass and retention time (m/z = 689.37, z=2, RT=55-85 min). TMT peaks for these spectra were manually quantified using Xcalibur Qual Browser to extract peak heights. Phosphosites for Ptpn11 (Y62), Lyn (Y508), Fgr (Y511), Fyn (Y531), and Siglec-F (Y561) were re-assigned after manual validation of spectra with an updated version of CAMV (Curran et al., 2013). Schematic images in **Figure 1A**, **Figure 5A**, and the graphical abstract were created were created with BioRender (https://biorender.com).

Searched .msf files were imported and processed using pyproteome, an in-house tool for phosphoproteomics data integration and analysis. Peptide-spectrum matches (PSMs) were read directly into pandas data frames from .msf files using programmed SQLite queries. PSMs were filtered using an ion score cutoff > 15, isolation interference < 30, and median TMT signal > 1500, and Percolator FDR < 5e-2. Transgenic peptides were excluded from filtering on percolator values. TMT quantification data was normalized using a iterative fitting procedure based on the CONSTrained STANdardization algorithm (Maes et al., 2016). In this procedure, the matrix of filtered TMT quantification values was iteratively adjusted such that rows were mean-centered around 1 and columns were mode-centered around 1. Mode centers were calculated by fitting a gaussian KDE distribution (scipy.stats.kde.gaussian_kde) to column intensities and finding the max value of its probability density function. Duplicate PSMs were then grouped for final quantification using a weighted mean function: $TMT * (1 - \frac{\text{isolation inference}}{100})$ for the TMT intensities and isolation interference value quantified by Proteome Discoverer for each PSM. Heatmaps were generated using seaborn and matplotlib.

Motif enrichment analysis

Motif logo enrichment values were calculated according to the method described for pLogo (O'Shea et al., 2013). Only non-ambiguous phosphopeptides (ptmRS probability > .75) were analyzed, each phosphorylated site on a peptide was considered as its own N-mer. N-mers were set to 15 amino acids. Foreground and background N-mers were extracted from protein-aligned sequences, using 'A' to pad N-and C-terminal peptides. Quantification values from identical N-mers (mis-cleaved, oxidized, or

multiply-phosphorylated peptides) were combined by taking the median value. Log odds enrichment values are equal to $-\log_{10}\frac{sf(k-1)}{cdf(k)}$, with k = the count of amino acids at that relative position for phosphosites in a foreground collection ($p < .05$; FC > 1.25 or FC < .8). Survival function (sf) and cumulative distribution functions (cdf) were calculated using scipy's hypergeometric distribution model (scipy.stats.hypergeom), with: n = the total number of foreground N-mers; K = the count of amino acids at that position in the background collection; and N=the total number of background N-mers.

The number of residues matching a phosphorylation motif was calculated for each phosphorylated site on a peptide and reported as the maximum number for multiply phosphorylated peptides. The patterns used were: (1) CaMKII Motif: - [FLMVI] - [RK] - Q - . - [st] - [FLMVI]-; (2) CDK Motif: - [st] - P - K - K -. For this pattern, '.' matches any residue and [st] matches pSer/pThr. Wildcards and phosphosites were not included in the total residue count for motifs.

Cell-type enrichment analysis

Gene cell-type predictions were estimated using a cell-type specific sequencing atlas (Zhang et al., 2014, 2016). Cell expression values were extracted from Table S4 using the following columns: 'Astrocyte': ['1 month', '4 months', '7 months', '9 months'], 'Neuron': ['Neuron 3', 'Neuron 4'], 'OPC': ['Oligodendrocyte precursor cell 3', 'Oligodendrocyte precursor cell 4'], 'New Oligodendrocytes': ['Newly formed oligodendrocyte 3', 'Newly formed oligodendrocyte 4'], 'Myelinating Oligodendrocytes': 'Myelinating oligodendrocyte 4', 'Myelinating oligodendrocyte 5'], 'Microglia': ['Microglia 1', 'Microglia 2'], 'Endothelia': ['Endo 1', 'Endo 2']. Genes were calculated as being enriched in a given cell type if they met the criteria $\frac{\mu_{cell\ type}}{\sum_{i \neq cell\ type} \mu_i} > 2.5$, where μ is the mean FPKM value from collections of columns for each cell type. OPC and New Oligodendrocytes were excluded from the enrichment calculation to avoid exclusion of pan-oligodendrocyte genes, only 'Myelinating Oligodendrocytes' was used for the displayed 'Oligodendrocyte' category.

Cell type enrichments were calculated on peptide clusters defined by upregulation ($p < 1e\text{-}2$, FC > 1.25) or downregulation ($p < 1e\text{-}2$, FC < .8). Peptides were compared using pooled data from the cortex and hippocampus from all mice with each diseased genotype compared to its WT controls. Peptides in clusters mapping to only one protein were processed into a list of unique genes with at least one PSM (modified or unmodified) that were enriched in any cell type. Log odds enrichment (LOE) values were calculated from hypergeometric distribution functions calculated from foreground and background sets in a manner similar to motif logos above.

Phosphosite enrichment analysis

Phosphosite enrichment analysis (PSEA) were performed using the procedure outlined in a previous publications (Krug et al., 2018). We used a custom phosphosite database derived from Phosphosite Plus (PSP) (Hornbeck et al., 2015). Kinase-substrate mappings were downloaded from PSP using information for all species (Kinase_Substrate_Dataset.gz), and then re-mapped to mouse phosphosites using homology information from PSP (Phosphorylation_site_dataset.gz). Phosphopeptide fold changes were estimated from the median value of redundant peptides. Fold changes were z-scored and phosphosites were rank ordered. Enrichment scores were calculated using the integral of a running-sum statistic (exponential weight = 0.75) that was increased for each gene or site contained within a given set and decreased for each gene not contained in that set. Enrichment scores for 1000 matrices with scrambled rows were generated and used to calculate an empirical p-value, q-value, and

normalized enrichment score (NES). Only phosphosite sets with a minimum overlapping set size of 20 were scored. Phosphosite sets that were enriched in at least two models were selected for display.

Gene ontology analysis

Gene ontologies were generated using goatools (Klopfenstein et al., 2018). The following GO terms were used for each category: Signal Transduction: GO:0016791 (phosphatase activity), GO:0007165 (signal transduction); Endosome: GO:0005768 (endosome); Adhesion: GO:0007155 (cell adhesion); Cytoskeleton: GO:0005856 (cytoskeleton); Metabolism: GO:0008152 (metabolic process).

scRNA-Seq data analysis

Single cell RNA (scRNA) data was downloaded for: (1) CK-p25 mice (Mathys et al., 2017) using NCBI:GEO accession GSE103334; (2) 5XFAD mice (Keren-Shaul et al., 2017) using NCBI:GEO accession GSE98971. scRNA datasets were smoothed for missing values using MAGIC (van Dijk et al., 2018). CK-p25 data was displayed using tSNE coordinates from the original publication. Cells clustered as "microglia" from 5XFAD and C57BL/6 mice in Keren-Shaul et al. were re-projected using UMAP (McInnes et al., 2018) as original tSNE coordinates were not available.

Immunofluorescence overlap, proximity, and intensity analysis

Z-stack projections, channel masks, area coverage, percentage overlap, and mask-proximity analyses were calculated using ImageJ. Z-stack slices were first normalized using the attenuation correction plugin (Biot et al., 2008). To remove background, mean slice signal intensities were multiplied by a constant factor (Siglec-8 = 3.5, Iba1 = 3, Siglec-F = 3.5, MHC-II = 3, Aβ= 8) and then subtracted from raw pixel intensities. Masks were generated from the Iba1, MHC, and Siglec channels using ImageJ's Huang method to automatically set thresholds, and then slices were filtered for 2d particles with size > 0.5 μm^2.

For overlap analysis, Siglec channel intensities were multiplied by copies of the Iba1 and/or MHC-II masks that were dilated in 3D by 2 voxels to cover neighboring antibody signals. Voxel mask binary operations were performed using the And/Or/Not operations provided by ImageJ's CLIJ plugin (Haase et al., 2020). Mask overlap was calculated as $\frac{Siglec \cap Iba1}{Siglec}$ for mask intensity and area values. Mask-proximity analyses were performed by calculating the distance between each voxel in an image mask and the nearest Aβ plaque (> 10 μm^3). Aβ plaques were located using ImageJ's 3D Objects Counter plugin. Proximity and mask overlap values were calculated for individual 20x wide-field images. Cumulative distribution functions, Kolmogorov–Smirnov (K-S), and 2-sample t-test statistics were generated using numpy and scipy (Virtanen et al., 2020; Van Der Walt et al., 2011).

For quantification of Siglec-8 IF images, we generated binary masks from Iba1 and DAPI channels. We then restricted masks to $Iba1^+;33342^-$ regions to generate cell masks and calculated Siglec-8 channel intensities within masks with size > 100 μm^2. Median object intensities were used for each image's quantification of Siglec-8. 2-sample t-test statistics on Siglec-8 intensity mean values for images were calculated using scipy (Virtanen et al., 2020).

Incucyte cell confluency analysis

Incucyte brightfield, green-, and red-fluorescence images were collected every 2-3 hours through a 10X objective. 96-wells were analyzed with 4 images per well. 24-wells were analyzed with 9 images per well. IncuCyte ZOOM software was used to calculate cell boundaries from each brightfield

image using a neural network trained on example BV-2 images. Confluency measurements were exported for the properties: Confluency = "Phase Object Confluence (Percent)", Object Count = "Phase Object Count (1/Well)", and Object Size = "Avg Phase Object Area (µm²)". Confluency values were normalized to the earliest time point unobstructed by fog, bubbles, or out-of-focus cells (1-6 hours, manually selected from each assay). Doubling times were calculated as $t_2 = \frac{\Delta t \ln 2}{\ln\left(\frac{y_f}{y_0}\right)}$. 2-sample t-test statistics on median confluency values from biological replicates were calculated using scipy.

RNA-Seq and qPCR data analysis

mRNA libraries were prepared for 5-6 biological replicates of each Siglec receptor and control constructs. FastQ sequencing files were aligned to mm10 (ens88 annotation) with STAR and results were summarized using RSEM. Differential gene expressions were calculated using DESeq2 running under R. Single sample GSEA enrichment scores were calculated using MSigDB (h, c2cp, c5bp, c5cc, c5mf collections) with the parameters xtools.gsea.GseaPreranked, set_min=5, set_max=1500, and nperm=1000. salmon (Patro et al., 2017) was used to ensure each sample had correct expression of Siglec construct sequences.

qPCR C_q values were exported from the Bio-Rad CFX Manager and processed with pandas. C_q values < 15 or > 40 were discarded and median C_q values were calculated from 2-4 technical replicates of each sample-target combination. Fold changes were calculated as $2^{-\Delta\Delta Cq}$ for quantification cycle number relative to GADPH in each sample. 2-sample t-test statistics were generated using scipy.

DATA AND CODE AVAILABILITY

Data supporting findings from this study are available from the Lead Contact, Forest M. White, upon reasonable request. All proteomics data generated in this study has been deposited on PRIDE under the accession: PXD018757. All sequence data has been deposited in Gene Expression Omnibus and are available under the accession: GSE149153.

The proteomics data integration software is available on GitHub (https://github.com/white-lab/pyproteome). This repository also includes detailed software for concatenating peptide fractions on a Gibson FC 204 Fraction Collection (https://github.com/white-lab/fc-cycle), and an updated tool for validating PSMs (https://github.com/white-lab/CAMV). Sources for other code used in this study are indicated in the Key Resources Table.

ADDITIONAL RESOURCES

Detailed protocols for proteomics sample processing, phosphopeptide enrichment, C18 column preparation, and other cellular assays are available online: https://github.com/white-lab/protocols

References

Abud, E.M., Ramirez, R.N., Martinez, E.S., Healy, L.M., Nguyen, C.H.H., Newman, S.A., Yeromin, A. V, Scarfone, V.M., Marsh, S.E., Fimbres, C., et al. (2017). iPSC-Derived Human Microglia-like Cells to Study Neurological Diseases. Neuron *94*, 278-293.e9.

Aizawa, H., Zimmermann, N., Carrigan, P.E., Lee, J.J., Rothenberg, M.E., and Bochner, B.S. (2003). Molecular analysis of human Siglec-8 orthologs relevant to mouse eosinophils: Identification of mouse orthologs of Siglec-5 (mSiglec-F) and Siglec-10 (mSiglec-G). Genomics *82*, 521–530.

Alfonso, S.I., Callender, J.A., Hooli, B., Antal, C.E., Mullin, K., Sherman, M.A., Lesné, S.E., Leitges, M., Newton, A.C., Tanzi, R.E., et al. (2016). Gain-of-function mutations in protein kinase Cα (PKCα) may promote synaptic defects in Alzheimer's disease. Sci. Signal. *9*, ra47.

Angata, T. (2014). Associations of genetic polymorphisms of Siglecs with human diseases. Glycobiology *24*, 785–793.

Angata, T., Hingorani, R., Varki, N.M., and Varki, A. (2001). Cloning and Characterization of a Novel Mouse Siglec, mSiglec-F: Differential evolution of the mouse and human (CD33) Siglec-3-related gene clusters. J. Biol. Chem. *276*, 45128–45136.

Angata, T., Margulies, E.H., Green, E.D., and Varki, A. (2004). Large-scale sequencing of the CD33-related Siglec gene cluster in five mammalian species reveals rapid evolution by multiple mechanisms. Proc. Natl. Acad. Sci. U. S. A. *101*, 13251–13256.

Aran, D., Looney, A.P., Liu, L., Wu, E., Fong, V., Hsu, A., Chak, S., Naikawadi, R.P., Wolters, P.J., Abate, A.R., et al. (2019). Reference-based analysis of lung single-cell sequencing reveals a transitional profibrotic macrophage. Nat. Immunol. *20*, 163–172.

Bai, B., Wang, X., Li, Y., Chen, P.-C., Yu, K., Dey, K.K., Yarbro, J.M., Han, X., Lutz, B.M., Rao, S., et al. (2020). Deep Multilayer Brain Proteomics Identifies Molecular Networks in Alzheimer's Disease Progression. Neuron *105*, 975-991.e7.

Beaudette, K.N., Lew, J., and Wang, J.H. (1993). Substrate specificity characterization of a cdc2-like protein kinase purified from bovine brain. J. Biol. Chem. *268*, 20825–20830.

Berchtold, N.C., Cribbs, D.H., Coleman, P.D., Rogers, J., Head, E., Kim, R., Beach, T., Miller, C., Troncoso, J., Trojanowski, J.Q., et al. (2008). Gene expression changes in the course of normal brain aging are sexually dimorphic. Proc. Natl. Acad. Sci. U. S. A. *105*, 15605–15610.

Bhattacherjee, A., Rodrigues, E., Jung, J., Luzentales-Simpson, M., Enterina, J.R., Galleguillos, D., St. Laurent, C.D., Nakhaei-Nejad, M., Fuchsberger, F.F., Streith, L., et al. (2019). Repression of phagocytosis by human CD33 is not conserved with mouse CD33. Commun. Biol. *2*, 1–13.

Biot, E., Crowell, E., Höfte, H., Maurin, Y., Vernhettes, S., and Andrey, P. (2008). A new filter for spot extraction in N-dimensional biological imaging. In 2008 5th IEEE International Symposium on Biomedical Imaging: From Nano to Macro, Proceedings, ISBI, p.

Birdsill, A.C., Walker, D.G., Lue, L.F., Sue, L.I., and Beach, T.G. (2011). Postmortem interval effect on RNA and gene expression in human brain tissue. Cell Tissue Bank. *12*, 311–318.

Blasi, E., Barluzzi, R., Bocchini, V., Mazzolla, R., and Bistoni, F. (1990). Immortalization of murine microglial cells by a v-raf / v-myc carrying retrovirus. J. Neuroimmunol. *27*, 229–237.

Bradshaw, E.M., Chibnik, L.B., Keenan, B.T., Ottoboni, L., Raj, T., Tang, A., Rosenkrantz, L.L., Imboywa, S., Lee, M., Von Korff, A., et al. (2013). CD33 Alzheimer's disease locus: altered monocyte function and amyloid biology. Nat. Neurosci. *16*, 848–850.

Butovsky, O., Jedrychowski, M.P., Moore, C.S., Cialic, R., Lanser, A.J., Gabriely, G., Koeglsperger, T., Dake, B., Wu, P.M., Doykan, C.E., et al. (2014). Identification of a unique TGF-β-dependent molecular and functional signature in microglia. Nat. Neurosci. *17*, 131–143.

Canter, R.G., Huang, W.-C., Choi, H., Wang, J., Ashley Watson, L., Yao, C.G., Abdurrob, F., Bousleiman, S.M., Young, J.Z., Bennett, D.A., et al. (2019). 3D mapping reveals network-specific amyloid progression and subcortical susceptibility in mice. Commun. Biol. *2*, 360.

Carrasquillo, M.M., Belbin, O., Hunter, T.A., Ma, L., Bisceglio, G.D., Zou, F., Crook, J.E., Pankratz, V.S., Sando, S.B., Aasly, J.O., et al. (2011). Replication of EPHA1 and CD33 associations with late-onset Alzheimer's disease: a multi-centre case-control study. Mol. Neurodegener. *6*, 54.

Castanho, I., Murray, T.K., Hannon, E., Jeffries, A., Walker, E., Laing, E., Baulf, H., Harvey, J., Bradshaw, L., Randall, A., et al. (2020). Transcriptional Signatures of Tau and Amyloid Neuropathology. Cell Rep. *30*, 2040-2054.e5.

Cavallini, A., Brewerton, S., Bell, A., Sargent, S., Glover, S., Hardy, C., Moore, R., Calley, J., Ramachandran, D., Poidinger, M., et al. (2013). An unbiased approach to identifying tau kinases that phosphorylate tau at sites associated with alzheimer disease. J. Biol. Chem. *288*, 23331–23347.

Chan, G., White, C.C., Winn, P.A., Cimpean, M., Replogle, J.M., Glick, L.R., Cuerdon, N.E., Ryan, K.J., Johnson, K.A., Schneider, J.A., et al. (2015). CD33 modulates TREM2: convergence of Alzheimer loci. Nat. Neurosci.

Chemnitz, J.M., Parry, R. V., Nichols, K.E., June, C.H., and Riley, J.L. (2004). SHP-1 and SHP-2 Associate with Immunoreceptor Tyrosine-Based Switch Motif of Programmed Death 1 upon Primary Human T Cell Stimulation, but Only Receptor Ligation Prevents T Cell Activation. J. Immunol. *173*, 945–954.

Chen, Y.-N.P., LaMarche, M.J., Chan, H.M., Fekkes, P., Garcia-Fortanet, J., Acker, M.G., Antonakos, B., Chen, C.H.-T., Chen, Z., Cooke, V.G., et al. (2016). Allosteric inhibition of SHP2 phosphatase inhibits cancers driven by receptor tyrosine kinases. Nature *535*, 148–152.

Choi, S.H., Kim, Y.H., Hebisch, M., Sliwinski, C., Lee, S., D'Avanzo, C., Chen, H., Hooli, B., Asselin, C., Muffat, J., et al. (2014). A three-dimensional human neural cell culture model of Alzheimer's disease. Nature *515*, 274–278.

Chui, A.J., Okondo, M.C., Rao, S.D., Gai, K., Griswold, A.R., Johnson, D.C., Ball, D.P., Taabazuing, C.Y., Orth, E.L., Vittimberga, B.A., et al. (2019). N-terminal degradation activates the NLRP1B inflammasome. Science (80-.). *364*, 82–85.

Colonna, M., and Wang, Y. (2016). TREM2 variants: new keys to decipher Alzheimer disease pathogenesis. Nat. Rev. Neurosci. *17*, 201–207.

Counts, S.E., and Mufson, E.J. (2017). Regulator of cell cycle (RGCC) expression during the progression of Alzheimer's disease. Cell Transplant. *26*, 693–702.

Cruz, J.C., Tseng, H.C., Goldman, J.A., Shih, H., and Tsai, L.-H. (2003). Aberrant Cdk5 activation by p25 triggers pathological events leading to neurodegeneration and neurofibrillary tangles. Neuron *40*,

471–483.

Cruz, J.C., Kim, D., Moy, L.Y., Dobbin, M.M., Sun, X., Bronson, R.T., and Tsai, L.-H. (2006). P25/Cyclin-Dependent Kinase 5 Induces Production and Intraneuronal Accumulation of Amyloid Beta in Vivo. J. Neurosci. *26*, 10536–10541.

Curran, T.G., Bryson, B.D., Reigelhaupt, M., Johnson, H., and White, F.M. (2013). Computer aided manual validation of mass spectrometry-based proteomic data. Methods *61*, 219–226.

Dammer, E.B., Lee, A.K., Duong, D.M., Gearing, M., Lah, J.J., Levey, A.I., and Seyfried, N.T. (2015). Quantitative phosphoproteomics of Alzheimer's disease reveals cross-talk between kinases and small heat shock proteins. Proteomics *15*, 508–519.

van Dijk, D., Sharma, R., Nainys, J., Yim, K., Kathail, P., Carr, A.J., Burdziak, C., Moon, K.R., Chaffer, C.L., Pattabiraman, D., et al. (2018). Recovering Gene Interactions from Single-Cell Data Using Data Diffusion. Cell 1–14.

Dittmann, A., Kennedy, N.J., Soltero, N.L., Morshed, N., Mana, M.D., Yilmaz, Ö.H., Davis, R.J., and White, F.M. (2019). High-fat diet in a mouse insulin-resistant model induces widespread rewiring of the phosphotyrosine signaling network. Mol. Syst. Biol. *15*, e8849.

Duan, S., and Paulson, J.C. (2020). Siglecs as Immune Cell Checkpoints in Disease. Annu. Rev. Immunol. *38*, 365–395.

Engblom, C., Pfirschke, C., Zilionis, R., Da Silva Martins, J., Bos, S.A., Courties, G., Rickelt, S., Severe, N., Baryawno, N., Faget, J., et al. (2017). Osteoblasts remotely supply lung tumors with cancer-promoting SiglecF high neutrophils. Science (80-.). *358*.

Ficarro, S.B., McCleland, M.L., Stukenberg, P.T., Burke, D.J., Ross, M.M., Shabanowitz, J., Hunt, D.F., and White, F.M. (2002). Phosphoproteome analysis by mass spectrometry and its application to Saccharomyces cerevisiae. Nat. Biotechnol. *20*, 301–305.

El Firar, A., Voisin, T., Rouyer-Fessard, C., Ostuni, M. a, Couvineau, A., and Laburthe, M. (2009). Discovery of a functional immunoreceptor tyrosine-based switch motif in a 7-transmembrane-spanning receptor: role in the orexin receptor OX1R-driven apoptosis. FASEB J. *23*, 4069–4080.

Fischer, A., Sananbenesi, F., Pang, P.T., Lu, B., and Tsai, L.-H. (2005). Opposing roles of transient and prolonged expression of p25 in synaptic plasticity and hippocampus-dependent memory. Neuron *48*, 825–838.

Flanagan, M.E., Blumenkopf, T.A., Brissette, W.H., Brown, M.F., Casavant, J.M., Shang-Poa, C., Doty, J.L., Elliott, E.A., Fisher, M.B., Hines, M., et al. (2010). Discovery of CP-690,550: A potent and selective janus kinase (JAK) inhibitor for the treatment of autoimmune diseases and organ transplant rejection. J. Med. Chem. *53*, 8468–8484.

Gajadhar, A.S., Johnson, H., Slebos, R.J.C., Shaddox, K., Wiles, K., Washington, M.K., Herline, A.J., Levine, D.A., Liebler, D.C., and White, F.M. (2015). Phosphotyrosine signaling analysis in human tumors is confounded by systemic ischemia-driven artifacts and intra-specimen heterogeneity. Cancer Res. *75*, 1495–1503.

Gao, P.S., Shimizu, K., Grant, A. V., Rafaels, N., Zhou, L.F., Hudson, S.A., Konno, S., Zimmermann, N., Araujo, M.I., Ponte, E. V., et al. (2010). Polymorphisms in the sialic acid-binding immunoglobulin-like lectin-8 (Siglec-8) gene are associated with susceptibility to asthma. Eur. J. Hum. Genet. *18*, 713–719.

Ghetti, B., Allen, B., Ingram, E., Smith, M.J., Takao, M., Spillantini, M.G., and Goedert, M. (2002). Abundant tau filaments and neurodegeneration in mice transgenic for human P301S tau. J. Neuropathol. Exp. Neurol. *61*, 484.

Ghosh, A., and Giese, K.P. (2015). Calcium/calmodulin-dependent kinase II and Alzheimer's disease. Mol. Brain *8*, 1–7.

Green, D.R. (2019). The Coming Decade of Cell Death Research: Five Riddles. Cell *177*, 1094–1107.

Griciuc, A., Serrano-Pozo, A., Parrado, A.R., Lesinski, A.N., Asselin, C.N., Mullin, K., Hooli, B., Choi, S.H., Hyman, B.T., and Tanzi, R.E. (2013). Alzheimer's disease risk gene CD33 inhibits microglial uptake of amyloid beta. Neuron *78*, 631–643.

Griciuc, A., Patel, S., Federico, A.N., Choi, S.H., Innes, B.J., Oram, M.K., Cereghetti, G., McGinty, D., Anselmo, A., Sadreyev, R.I., et al. (2019). TREM2 Acts Downstream of CD33 in Modulating Microglial Pathology in Alzheimer's Disease. Neuron 1–16.

Haase, R., Royer, L.A., Steinbach, P., Schmidt, D., Dibrov, A., Schmidt, U., Weigert, M., Maghelli, N., Tomancak, P., Jug, F., et al. (2020). CLIJ: GPU-accelerated image processing for everyone. Nat. Methods *17*, 5–6.

Haim, L. Ben, Ceyzériat, K., Sauvage, M.A.C. de, Aubry, F., Auregan, G., Guillermier, M., Ruiz, M., Petit, F., Houitte, D., Faivre, E., et al. (2015). The JAK/STAT3 pathway is a common inducer of astrocyte reactivity in Alzheimer's and Huntington's diseases. J. Neurosci. *35*, 2817–2829.

Henn, A., Lund, S., Hedtjärn, M., Schrattenholz, A.A., Pörzgen, P., and Leist, M. (2009). The suitability of BV2 cells as alternative model system for primary microglia cultures or for animal experiments examining brain inflammation. ALTEX Altern. Zu Tierexperimenten *26*, 83–94.

Henriques, A.G., Muller, T., Oliveira, J.M., Cova, M., da Cruz e Silva, C.B., and da Cruz e Silva, O.A.B. (2007). Altered protein phosphorylation as a resource for potencial AD biomarkers. Nat. Publ. Gr. 1–13.

Hollingworth, P., Harold, D., Sims, R., Gerrish, A., Lambert, J.-C., Carrasquillo, M.M., Abraham, R., Hamshere, M.L., Pahwa, J.S., Moskvina, V., et al. (2011). Common variants at ABCA7, MS4A6A/MS4A4E, EPHA1, CD33 and CD2AP are associated with Alzheimer's disease. Nat. Genet. *43*, 429–435.

Hoos, M.D., Richardson, B.M., Foster, M.W., Everhart, A., Thompson, J.W., Moseley, M.A., and Colton, C.A. (2013). Longitudinal study of differential protein expression in an Alzheimer's mouse model lacking inducible nitric oxide synthase. J. Proteome Res. *12*, 4462–4477.

Hornbeck, P. V., Zhang, B., Murray, B., Kornhauser, J.M., Latham, V., and Skrzypek, E. (2015). PhosphoSitePlus, 2014: Mutations, PTMs and recalibrations. Nucleic Acids Res. *43*, D512–D520.

Jansen, I.E., Savage, J.E., Watanabe, K., Bryois, J., Williams, D.M., Steinberg, S., Sealock, J., Karlsson, I.K., Hägg, S., Athanasiu, L., et al. (2019). Genome-wide meta-analysis identifies new loci and functional pathways influencing Alzheimer's disease risk. Nat. Genet. *51*, 404–413.

Johnson, H., and White, F.M. (2012). Toward quantitative phosphotyrosine profiling in vivo. Semin. Cell Dev. Biol. *23*, 854–862.

Johnson, H., Del Rosario, A.M., Bryson, B.D., Schroeder, M.A., Sarkaria, J.N., and White, F.M.

(2012). Molecular Characterization of EGFR and EGFRvIII Signaling Networks in Human Glioblastoma Tumor Xenografts. Mol. Cell. Proteomics *11*, 1724–1740.

Joughin, B. a, Naegle, K.M., Huang, P.H., Yaffe, M.B., Lauffenburger, D.A., and White, F.M. (2009). An integrated comparative phosphoproteomic and bioinformatic approach reveals a novel class of MPM-2 motifs upregulated in EGFRvIII-expressing glioblastoma cells. Mol. Biosyst. *5*, 59–67.

Karch, C.M., and Goate, A.M. (2014). Alzheimer's Disease Risk Genes and Mechanisms of Disease Pathogenesis. Biol. Psychiatry *77*, 43–51.

Keren-Shaul, H., Spinrad, A., Weiner, A., Matcovitch-Natan, O., Dvir-Szternfeld, R., Ulland, T.K., David, E., Baruch, K., Lara-Astaiso, D., Toth, B., et al. (2017). A Unique Microglia Type Associated with Restricting Development of Alzheimer's Disease. Cell *169*, 1276-1290.e17.

Kiwamoto, T., Kawasaki, N., Paulson, J.C., and Bochner, B.S. (2012). Siglec-8 as a drugable target to treat eosinophil and mast cell-associated conditions. Pharmacol. Ther. *135*, 327–336.

Kiwamoto, T., Katoh, T., Evans, C.M., Janssen, W.J., Brummet, M.E., Hudson, S.A., Zhu, Z., Tiemeyer, M., and Bochner, B.S. (2015). Endogenous airway mucins carry glycans that bind Siglec-F and induce eosinophil apoptosis. J. Allergy Clin. Immunol. *135*, 1329-1340.e9.

Klopfenstein, D. V., Zhang, L., Pedersen, B.S., Ramírez, F., Vesztrocy, A.W., Naldi, A., Mungall, C.J., Yunes, J.M., Botvinnik, O., Weigel, M., et al. (2018). GOATOOLS: A Python library for Gene Ontology analyses. Sci. Rep.

Krug, K., Mertins, P., Zhang, B., Hornbeck, P., Raju, R., Ahmad, R., Szucs, M., Mundt, F., Forestier, D., Jane-Valbuena, J., et al. (2018). A Curated Resource for Phosphosite-specific Signature Analysis. Mol. Cell. Proteomics *18*, 576–593.

Kunkle, B.W., Grenier-Boley, B., Sims, R., Bis, J.C., Damotte, V., Naj, A.C., Boland, A., Vronskaya, M., van der Lee, S.J., Amlie-Wolf, A., et al. (2019). Genetic meta-analysis of diagnosed Alzheimer's disease identifies new risk loci and implicates Aβ, tau, immunity and lipid processing. Nat. Genet.

Lambert, J.-C., Ibrahim-Verbaas, C. a, Harold, D., Naj, A.C., Sims, R., Bellenguez, C., Jun, G., DeStefano, A.L., Bis, J.C., Beecham, G.W., et al. (2013). Meta-analysis of 74,046 individuals identifies 11 new susceptibility loci for Alzheimer's disease. Nat. Genet. *45*, 1452–1458.

Lee, M.S., Kwon, Y.T., Li, M., Peng, J., Friedlander, R.M., and Tsai, L.H. (2000). Neurotoxicity induces cleavage of p35 to p25 by calpain. Nature.

Lemeer, S., and Heck, A.J. (2009). The phosphoproteomics data explosion. Curr. Opin. Chem. Biol.

Lin, Y.T., Seo, J., Gao, F., Feldman, H.M., Wen, H.L., Penney, J., Cam, H.P., Gjoneska, E., Raja, W.K., Cheng, J., et al. (2018). APOE4 Causes Widespread Molecular and Cellular Alterations Associated with Alzheimer's Disease Phenotypes in Human iPSC-Derived Brain Cell Types. Neuron *98*, 1141-1154.e7.

Liu, H., Li, L., Voss, C., Wang, F., Liu, J., and Li, S.S.-C. (2015). A Comprehensive Immunoreceptor Phosphotyrosine-based Signaling Network Revealed by Reciprocal Protein-Peptide Array Screening. Mol. Cell. Proteomics *14*, 1846–1858.

Maes, E., Hadiwikarta, W.W., Mertens, I., Baggerman, G., Hooyberghs, J., and Valkenborg, D. (2016). CONSTANd□: A Normalization Method for Isobaric Labeled Spectra by Constrained Optimization.

Mol. Cell. Proteomics *15*, 2779–2790.

Marttinen, M., Paananen, J., Neme, A., Mitra, V., Takalo, M., Natunen, T., Paldanius, K.M.A.A., Mäkinen, P., Bremang, M., Kurki, M.I., et al. (2018). A multiomic approach to characterize the temporal sequence in Alzheimer's disease-related pathology. Neurobiol. Dis. *124*, #pagerange#.

Mastrangelo, M.A., Sudol, K.L., Narrow, W.C., and Bowers, W.J. (2009). Interferon-γ differentially affects Alzheimer's disease pathologies and induces neurogenesis in triple transgenic-AD mice. Am. J. Pathol. *175*, 2076–2088.

Mathys, H., Adaikkan, C., Gao, F., Young, J.Z., Manet, E., Hemberg, M., De Jager, P.L., Ransohoff, R.M., Regev, A., and Tsai, L.-H. (2017). Temporal Tracking of Microglia Activation in Neurodegeneration at Single-Cell Resolution. Cell Rep. *21*, 366–380.

McInnes, L., Healy, J., and Melville, J. (2018). UMAP: Uniform Manifold Approximation and Projection for Dimension Reduction.

McQuade, A., Coburn, M., Tu, C.H., Hasselmann, J., Davtyan, H., and Blurton-Jones, M. (2018). Development and validation of a simplified method to generate human microglia from pluripotent stem cells. Mol. Neurodegener. *13*, 1–13.

Meerbrey, K.L., Hu, G., Kessler, J.D., Roarty, K., Li, M.Z., Fang, J.E., Herschkowitz, J.I., Burrows, A.E., Ciccia, A., Sun, T., et al. (2011). The pINDUCER lentiviral toolkit for inducible RNA interference in vitro and in vivo. Proc. Natl. Acad. Sci. U. S. A. *108*, 3665–3670.

Mota, S.I., Ferreira, I.L., Valero, J., Ferreiro, E., Carvalho, A.L., Oliveira, C.R., and Rego, A.C. (2014). Impaired Src signaling and post-synaptic actin polymerization in Alzheimer's disease mice hippocampus - Linking NMDA receptors and the reelin pathway. Exp. Neurol.

Naj, A.C., Jun, G., Beecham, G.W., Wang, L.-S., Vardarajan, B.N., Buros, J., Gallins, P.J., Buxbaum, J.D., Jarvik, G.P., Crane, P.K., et al. (2011). Common variants at MS4A4/MS4A6E, CD2AP, CD33 and EPHA1 are associated with late-onset Alzheimer's disease. Nat. Genet. *43*, 436–441.

O'Shea, J.P., Chou, M.F., Quader, S.A., Ryan, J.K., Church, G.M., and Schwartz, D. (2013). pLogo: a probabilistic approach to visualizing sequence motifs. Nat. Methods *10*, 1211–1212.

O'Sullivan, J.A., Carroll, D.J., Cao, Y., Salicru, A.N., and Bochner, B.S. (2018). Leveraging Siglec-8 endocytic mechanisms to kill human eosinophils and malignant mast cells. J. Allergy Clin. Immunol. *141*, 1774-1785.e7.

Oakley, H., Cole, S.L., Logan, S., Maus, E., Shao, P., Craft, J., Guillozet-Bongaarts, A., Ohno, M., Disterhoft, J., Van Eldik, L., et al. (2006). Intraneuronal β-Amyloid Aggregates, Neurodegeneration, and Neuron Loss in Transgenic Mice with Five Familial Alzheimer's Disease Mutations: Potential Factors in Amyloid Plaque Formation. J. Neurosci. *26*, 10129–10140.

van Olst, L., Verhaege, D., Franssen, M., Kamermans, A., Roucourt, B., Carmans, S., Ytebrouck, E., van der Pol, S.M.A., Wever, D., Popovic, M., et al. (2020). Microglial activation arises after aggregation of phosphorylated-tau in a neuron-specific P301S tauopathy mouse model. Neurobiol. Aging *89*, 89–98.

Patrick, G.N., Zukerberg, L., Nikolic, M., de la Monte, S., Dikkes, P., and Tsai, L.-H. (1999). Conversion of p35 to p25 deregulates Cdk5 activity and promotes neurodegeneration. Nature *402*, 615–622.

Patro, R., Duggal, G., Love, M.I., Irizarry, R.A., and Kingsford, C. (2017). Salmon provides fast and bias-aware quantification of transcript expression. Nat. Methods *14*, 417–419.

Pluvinage, J. V., Haney, M.S., Smith, B.A.H., Sun, J., Iram, T., Bonanno, L., Li, L., Lee, D.P., Morgens, D.W., Yang, A.C., et al. (2019). CD22 blockade restores homeostatic microglial phagocytosis in ageing brains. Nature *568*, 187–192.

Poulsen, E., Iannuzzi, F., Rasmussen, H., Maier, T., Enghild, J., Jørgensen, A., and Matrone, C. (2017). An aberrant phosphorylation of amyloid precursor protein tyrosine regulates its trafficking and the binding to the Clathrin endocytic complex in neural stem cells of Alzheimer's disease patients. Front. Mol. Neurosci. *10*, 59.

Reddy, R.J., Gajadhar, A.S., Swenson, E.J., Rothenberg, D.A., Curran, T.G., and White, F.M. (2016). Early signaling dynamics of the epidermal growth factor receptor. Proc. Natl. Acad. Sci. U. S. A. *113*, 3114–3119.

Rigbolt, K.T.G., and Blagoev, B. (2012). Quantitative phosphoproteomics to characterize signaling networks. Semin. Cell Dev. Biol.

Riley, N.M., and Coon, J.J. (2016). Phosphoproteomics in the Age of Rapid and Deep Proteome Profiling. Anal. Chem.

Rosenberger, A.F., Rozemuller, A.J., van der Flier, W.M., Scheltens, P., van der Vies, S.M., and Hoozemans, J.J. (2014). Altered distribution of the EphA4 kinase in hippocampal brain tissue of patients with Alzheimer's disease correlates with pathology. Acta Neuropathol. Commun. *2*, 79.

Sang, Y., Hou, Y., Cheng, R., Zheng, L., Alvarez, A.A., Hu, B., Cheng, S.-Y., Zhang, W., Li, Y., and Feng, H. (2019). Targeting PDGFRα-activated glioblastoma through specific inhibition of SHP-2–mediated signaling. Neuro. Oncol. 1–13.

Sankowski, R., Böttcher, C., Masuda, T., Geirsdottir, L., Sagar, Sindram, E., Seredenina, T., Muhs, A., Scheiwe, C., Shah, M.J., et al. (2019). Mapping microglia states in the human brain through the integration of high-dimensional techniques. Nat. Neurosci. *22*, 2098–2110.

Seo, J., Giusti-Rodríguez, P., Zhou, Y., Rudenko, A., Cho, S., Ota, K.T., Park, C., Patzke, H., Madabhushi, R., Pan, L., et al. (2014). Activity-dependent p25 generation regulates synaptic plasticity and aβ-induced cognitive impairment. Cell *157*, 486–498.

Siddiqui, S.S., Springer, S.A., Verhagen, A., Sundaramurthy, V., Alisson-Silva, F., Jiang, W., Ghosh, P., and Varki, A. (2017). The Alzheimer's Disease-protective CD33 splice variant mediates adaptive loss of function via diversion to an intracellular pool. J. Biol. Chem. *292*, jbc.M117.799346.

Songyang, Z., Blechner, S., Hoagland, N., Hoekstra, M.F., Piwnica-Worms, H., and Cantley, L.C. (1994). Use of an oriented peptide library to determine the optimal substrates of protein kinases. Curr. Biol. *4*, 973–982.

Steinke, J.W., Liu, L., Huyett, P., Negri, J., Payne, S.C., and Borish, L. (2013). Prominent role of IFN-γ in patients with aspirin-exacerbated respiratory disease. J. Allergy Clin. Immunol. *132*, 856-865.e3.

Stilling, R.M., Benito, E., Gertig, M., Barth, J., Capece, V., Burkhardt, S., Bonn, S., and Fischer, A. (2014). De-regulation of gene expression and alternative splicing affects distinct cellular pathways in the aging hippocampus. Front. Cell. Neurosci. *8*, 1–15.

De Strooper, B., and Karran, E. (2016). The Cellular Phase of Alzheimer's Disease. Cell *164*, 603–615.

Suzuki, K., Sako, K., Akiyama, K., Isoda, M., Senoo, C., Nakajo, N., and Sagata, N. (2015). Identification of non-Ser/Thr-Pro consensus motifs for Cdk1 and their roles in mitotic regulation of C2H2 zinc finger proteins and Ect2. Sci. Rep. *5*, 1–9.

Sweeney, M.C., Wavreille, A.S., Park, J., Butchar, J.P., Tridandapani, S., and Pei, D. (2005). Decoding protein-protein interactions through combinatorial chemistry: Sequence specificity of SHP-1, SHP-2, and SHIP SH2 domains. Biochemistry *44*, 14932–14947.

Tagawa, K., Homma, H., Saito, A., Fujita, K., Chen, X., Imoto, S., Oka, T., Ito, H., Motoki, K., Yoshida, C., et al. (2015). Comprehensive phosphoproteome analysis unravels the core signaling network that initiates the earliest synapse pathology in preclinical Alzheimer's disease brain. Hum. Mol. Genet. *24*, 540–558.

Tateno, H., Crocker, P.R., and Paulson, J.C. (2005). Mouse Siglec-F and human Siglec-8 are functionally convergent paralogs that are selectively expressed on eosinophils and recognize 6′-sulfo-sialyl Lewis X as a preferred glycan ligand. Glycobiology *15*, 1125–1135.

Tateno, H., Li, H., Schur, M.J., Bovin, N., Crocker, P.R., Wakarchuk, W.W., and Paulson, J.C. (2007). Distinct Endocytic Mechanisms of CD22 (Siglec-2) and Siglec-F Reflect Roles in Cell Signaling and Innate Immunity. Mol. Cell. Biol. *27*, 5699–5710.

Virtanen, P., Gommers, R., Oliphant, T.E., Haberland, M., Reddy, T., Cournapeau, D., Burovski, E., Peterson, P., Weckesser, W., Bright, J., et al. (2020). SciPy 1.0: fundamental algorithms for scientific computing in Python. Nat. Methods 1–22.

Walker, D.G., Whetzel, A.M., Serrano, G., Sue, L.I., Lue, L.F., and Beach, T.G. (2016). Characterization of RNA isolated from eighteen different human tissues: results from a rapid human autopsy program. Cell Tissue Bank. *17*, 361–375.

Van Der Walt, S., Colbert, S.C., and Varoquaux, G. (2011). The NumPy array: A structure for efficient numerical computation. Comput. Sci. Eng. *13*, 22–30.

Walter, R.B., Raden, B.W., Zeng, R., Hausermann, P., Bernstein, I.D., and Cooper, J.A. (2007). ITIM-dependent endocytosis of CD33-related Siglecs: role of intracellular domain, tyrosine phosphorylation, and the tyrosine phosphatases, Shp1 and Shp2. J. Leukoc. Biol. *83*, 200–211.

White, F.M., and Wolf-Yadlin, A. (2016). Methods for the Analysis of Protein Phosphorylation–Mediated Cellular Signaling Networks. Annu. Rev. Anal. Chem.

White, R.R., Kwon, Y.G., Taing, M., Lawrence, D.S., and Edelman, A.M. (1998). Definition of optimal substrate recognition motifs of Ca2+- calmodulin-dependent protein kinases IV and II reveals shared and distinctive features. J. Biol. Chem. *273*, 3166–3172.

Wickliffe, K.E., Leppla, S.H., and Moayeri, M. (2008). Killing of macrophages by anthrax lethal toxin: Involvement of the N-end rule pathway. Cell. Microbiol. *10*, 1352–1362.

Wolf-Yadlin, A., Kumar, N., Zhang, Y., Hautaniemi, S., Zaman, M., Kim, H.-D., Grantcharova, V., Lauffenburger, D.A., and White, F.M. (2006). Effects of HER2 overexpression on cell signaling networks governing proliferation and migration. Mol. Syst. Biol. *2*, 54.

Wood, L.B., Winslow, A.R., Proctor, E.A., McGuone, D., Mordes, D.A., Frosch, M.P., Hyman, B.T., Lauffenburger, D.A., and Haigis, K.M. (2015). Identification of neurotoxic cytokines by profiling Alzheimer's disease tissues and neuron culture viability screening. Sci. Rep. *5*, 16622.

Yoshiyama, Y., Higuchi, M., Zhang, B., Huang, S.M., Iwata, N., Saido, T.C.C., Maeda, J., Suhara, T., Trojanowski, J.Q., and Lee, V.M.Y. (2007). Synapse Loss and Microglial Activation Precede Tangles in a P301S Tauopathy Mouse Model. Neuron *53*, 337–351.

Youngblood, B.A., Brock, E.C., Leung, J., Falahati, R., Bryce, P.J., Bright, J., Williams, J., Shultz, L.D., Greiner, D.L., Brehm, M.A., et al. (2019). AK002, a Humanized Sialic Acid-Binding Immunoglobulin-Like Lectin-8 Antibody that Induces Antibody-Dependent Cell-Mediated Cytotoxicity against Human Eosinophils and Inhibits Mast Cell-Mediated Anaphylaxis in Mice. Int. Arch. Allergy Immunol. *94065*, 91–102.

Yu, C., Gao, J., Zhou, Y., Chen, X., Xiao, R., Zheng, J., Liu, Y., and Zhou, H. (2016). Deep Phosphoproteomic Measurements Pinpointing Drug Induced Protective Mechanisms in Neuronal Cells. Front. Physiol. *7*, 1–14.

Zhang, M., Angata, T., Cho, J.Y., Miller, M., Broide, D.H., and Varki, A. (2007). Defining the in vivo function of Siglec-F, a CD33-related Siglec expressed on mouse eosinophils. Blood *109*, 4280–4287.

Zhang, Y., Wolf-Yadlin, A., Ross, P.L., Pappin, D.J., Rush, J., Lauffenburger, D.A., and White, F.M. (2005). Time-resolved mass spectrometry of tyrosine phosphorylation sites in the epidermal growth factor receptor signaling network reveals dynamic modules. Mol. Cell. Proteomics *4*, 1240–1250.

Zhang, Y., Chen, K., Sloan, S.A., Bennett, M.L., Scholze, A.R., O'Keeffe, S., Phatnani, H.P., Guarnieri, P., Caneda, C., Ruderisch, N., et al. (2014). An RNA-sequencing transcriptome and splicing database of glia, neurons, and vascular cells of the cerebral cortex. J. Neurosci. *34*, 11929–11947.

Zhang, Y., Sloan, S.A., Clarke, L.E., Caneda, C., Plaza, C.A., Blumenthal, P.D., Vogel, H., Steinberg, G.K., Edwards, M.S.B.B., Li, G., et al. (2016). Purification and Characterization of Progenitor and Mature Human Astrocytes Reveals Transcriptional and Functional Differences with Mouse. Neuron *89*, 37–53.

Zheng, C., Zhou, X.W., and Wang, J.Z. (2016). The dual roles of cytokines in Alzheimer's disease: Update on interleukins, TNF-α, TGF-β and IFN-γ. Transl. Neurodegener. *5*.

Zhou, Y., Song, W.M., Andhey, P.S., Swain, A., Levy, T., Miller, K.R., Poliani, P.L., Cominelli, M., Grover, S., Gilfillan, S., et al. (2020). Human and mouse single-nucleus transcriptomics reveal TREM2-dependent and TREM2-independent cellular responses in Alzheimer's disease. Nat. Med. *26*, 131–142.

Zimmermann, N., McBride, M.L., Yamada, Y., Hudson, S.A., Jones, C., Cromie, K.D., Crocker, P.R., Rothenberg, M.E., and Bochner, B.S. (2008). Siglec-F antibody administration to mice selectively reduces blood and tissue eosinophils. Allergy Eur. J. Allergy Clin. Immunol. *63*, 1156–1163.

(2020). 2020 Alzheimer's disease facts and figures. Alzheimer's Dement. *16*, 391–460.

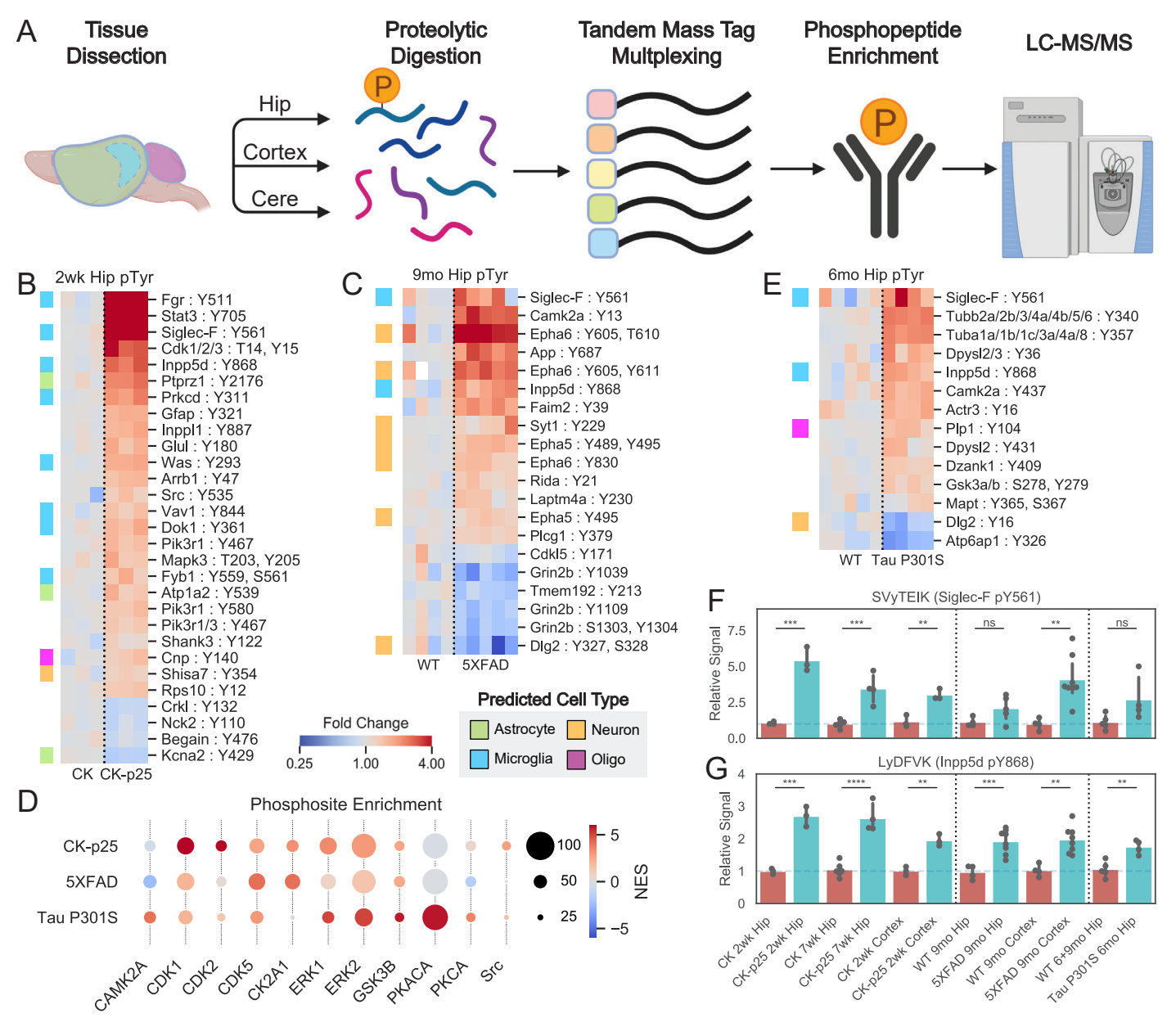
A
Tissue Dissection
Hip
Cortex
Cere
Proteolytic Digestion
Tandem Mass Tag Multplexing
Phosphopeptide Enrichment
LC-MS/MS
B
2wk Hip pTyr
Fgr : Y511
Stat3 : Y705
Siglec-F : Y561
Cdk1/2/3 : T14, Y15
Inpp5d : Y868
Ptprz1 : Y2176
Prkcd : Y311
Gfap : Y321
Inppl1 : Y887
Glul : Y180
Was : Y293
Arrb1 : Y47
Src : Y535
Vav1 : Y844
Dok1 : Y361
Pik3r1 : Y467
Mapk3 : T203, Y205
Fyb1 : Y559, S561
Atp1a2 : Y539
Pik3r1 : Y580
Pik3r1/3 : Y467
Shank3 : Y122
Cnp : Y140
Shisa7 : Y354
Rps10 : Y12
Crkl : Y132
Nck2 : Y110
Begain : Y476
Kcna2 : Y429
CK CK-p25
C
9mo Hip pTyr
Siglec-F : Y561
Camk2a : Y13
Epha6 : Y605, T610
App : Y687
Epha6 : Y605, Y611
Inpp5d : Y868
Faim2 : Y39
Syt1 : Y229
Epha5 : Y489, Y495
Epha6 : Y830
Rida : Y21
Laptm4a : Y230
Epha5 : Y495
Plcg1 : Y379
Cdkl5 : Y171
Grin2b : Y1039
Tmem192 : Y213
Grin2b : Y1109
Grin2b : S1303, Y1304
Dlg2 : Y327, S328
WT 5XFAD
E
6mo Hip pTyr
Siglec-F : Y561
Tubb2a/2b/3/4a/4b/5/6 : Y340
Tuba1a/1b/1c/3a/4a/8 : Y357
Dpysl2/3 : Y36
Inpp5d : Y868
Camk2a : Y437
Actr3 : Y16
Plp1 : Y104
Dpysl2 : Y431
Dzank1 : Y409
Gsk3a/b : S278, Y279
Mapt : Y365, S367
Dlg2 : Y16
Atp6ap1 : Y326
WT Tau P301S
Fold Change
0.25 1.00 4.00
Predicted Cell Type
Astrocyte
Neuron
Microglia
Oligo
D
Phosphosite Enrichment
CK-p25
5XFAD
Tau P301S
100
50
25
5
0
−5
NES
CAMK2A
CDK1
CDK2
CDK5
CK2A1
ERK1
ERK2
GSK3B
PKACA
PKCA
Src
F
SVyTEIK (Siglec-F pY561)
Relative Signal
7.5
5.0
2.5
0.0
*** *** ** ns ** ns
G
LyDFVK (Inpp5d pY868)
Relative Signal
4
3
2
1
0
*** **** ** *** ** **
CK 2wk Hip
CK-p25 2wk Hip
CK 7wk Hip
CK-p25 7wk Hip
CK 2wk Cortex
CK-p25 2wk Cortex
WT 9mo Hip
5XFAD 9mo Hip
WT 9mo Cortex
5XFAD 9mo Cortex
WT 6+9mo Hip
Tau P301S 6mo Hip

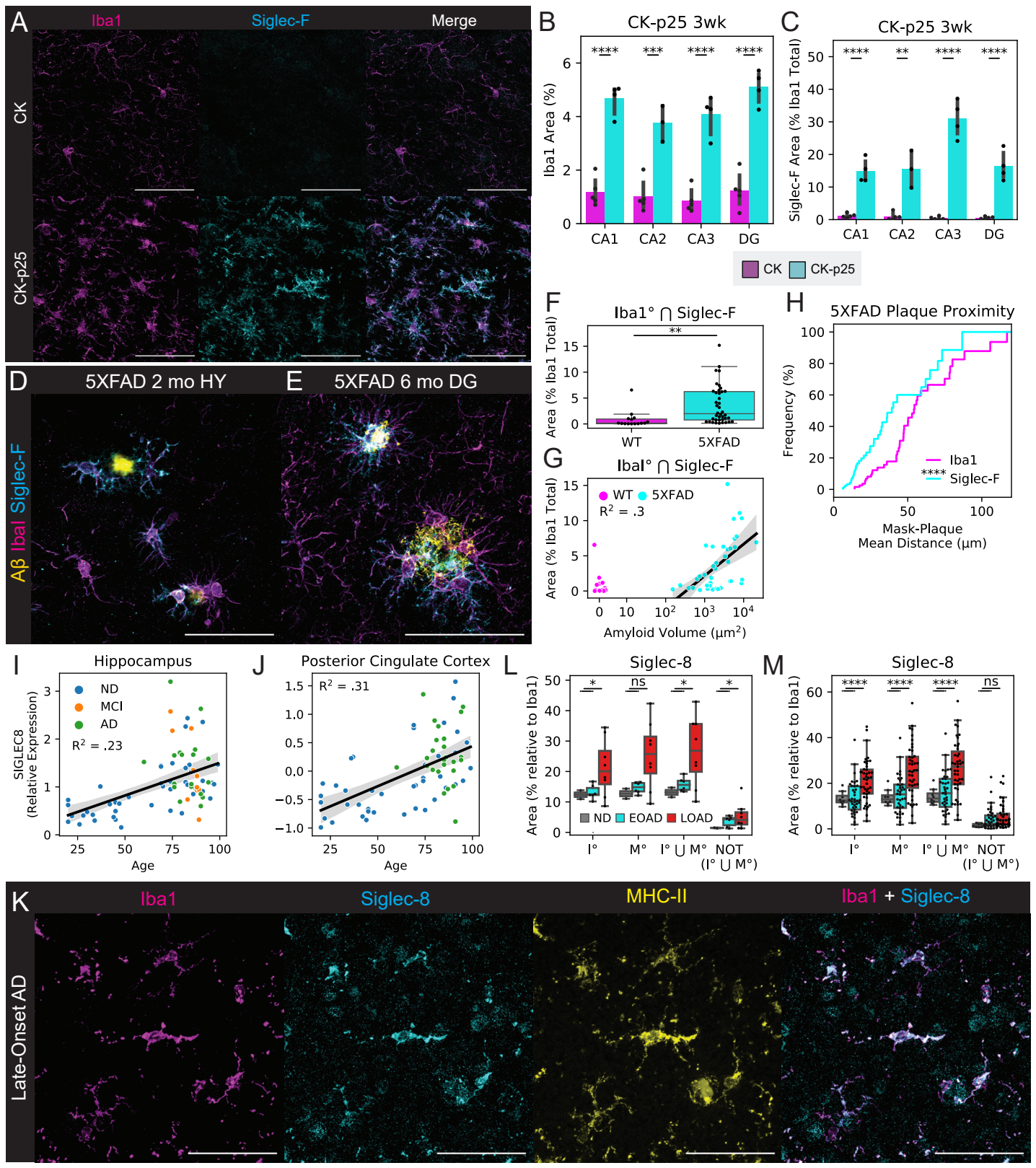
A
Iba1
Siglec-F
Merge
CK
CK-p25
B
CK-p25 3wk
Iba1 Area (%)
CA1
CA2
CA3
DG
C
CK-p25 3wk
Siglec-F Area (% Iba1 Total)
CK
CK-p25
D
5XFAD 2 mo HY
E
5XFAD 6 mo DG
Aβ Iba1 Siglec-F
F
Iba1° ⋂ Siglec-F
Area (% Iba1 Total)
WT
5XFAD
G
Iba1° ⋂ Siglec-F
WT
5XFAD
R² = .3
Area (% Iba1 Total)
Amyloid Volume (μm²)
H
5XFAD Plaque Proximity
Frequency (%)
Iba1
Siglec-F
Mask-Plaque
Mean Distance (μm)
I
Hippocampus
ND
MCI
AD
R² = .23
SIGLEC8
(Relative Expression)
Age
J
Posterior Cingulate Cortex
R² = .31
Age
L
Siglec-8
Area (% relative to Iba1)
ND
EOAD
LOAD
I°
M°
I° ⋃ M°
NOT
(I° ⋃ M°)
M
Siglec-8
Area (% relative to Iba1)
I°
M°
I° ⋃ M°
NOT
(I° ⋃ M°)
K
Iba1
Siglec-8
MHC-II
Iba1 + Siglec-8
Late-Onset AD

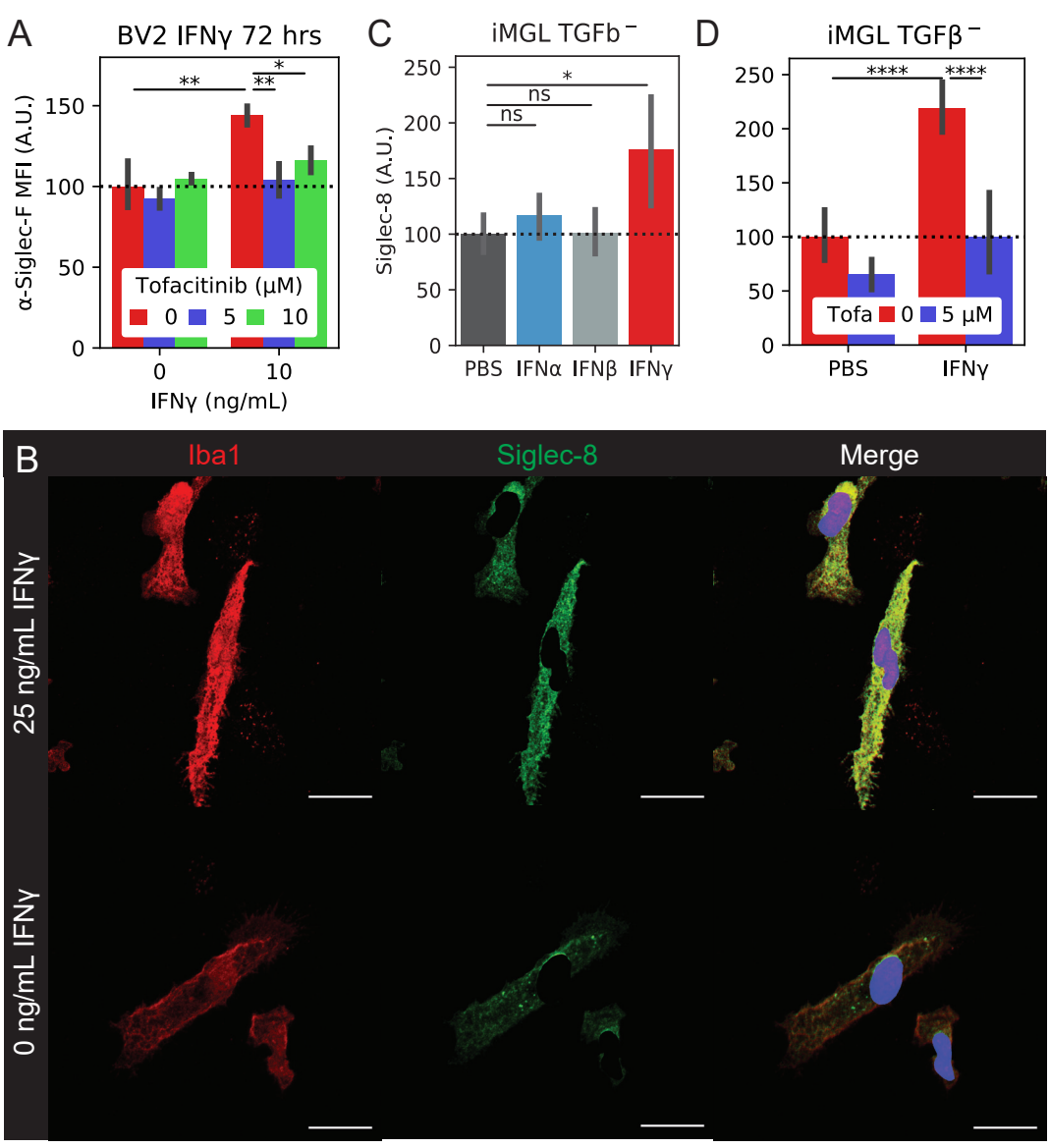
A
BV2 IFNγ 72 hrs
α-Siglec-F MFI (A.U.)
150
100
50
0
**
**
*
Tofacitinib (μM)
0
5
10
0
10
IFNγ (ng/mL)
C
iMGL TGFb⁻
Siglec-8 (A.U.)
250
200
150
100
50
0
*
ns
ns
PBS
IFNα
IFNβ
IFNγ
D
iMGL TGFβ⁻
250
200
150
100
50
0
****
****
Tofa
0
5 μM
PBS
IFNγ
B
Iba1
Siglec-8
Merge
25 ng/mL IFNγ
0 ng/mL IFNγ

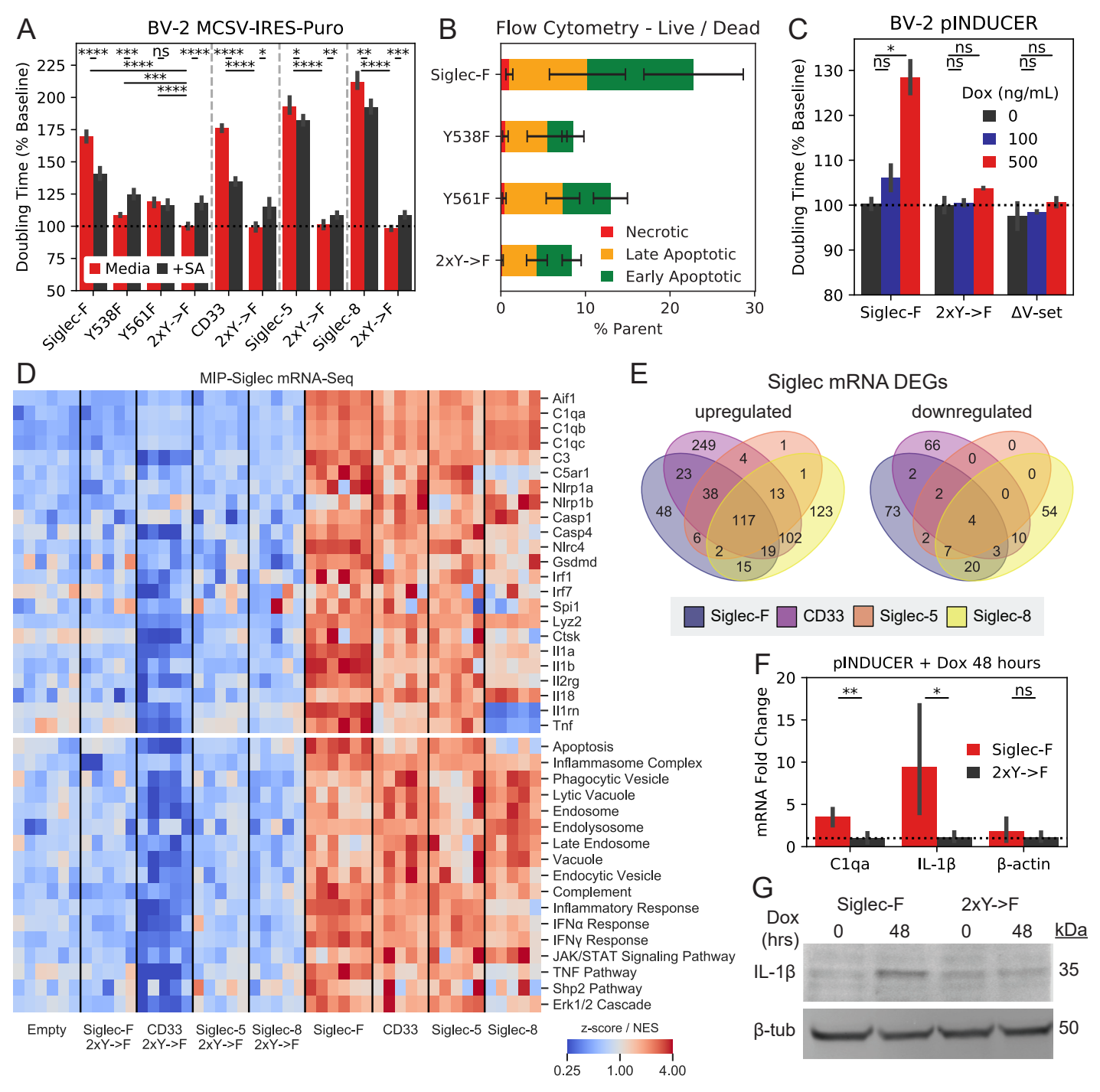
A
BV-2 MCSV-IRES-Puro
Doubling Time (% Baseline)
Media
+SA
Siglec-F
Y538F
Y561F
2xY->F
CD33
2xY->F
Siglec-5
2xY->F
Siglec-8
2xY->F
B
Flow Cytometry - Live / Dead
Siglec-F
Y538F
Y561F
2xY->F
Necrotic
Late Apoptotic
Early Apoptotic
% Parent
C
BV-2 pINDUCER
Doubling Time (% Baseline)
Dox (ng/mL)
0
100
500
Siglec-F
2xY->F
ΔV-set
D
MIP-Siglec mRNA-Seq
Aif1
C1qa
C1qb
C1qc
C3
C5ar1
Nlrp1a
Nlrp1b
Casp1
Casp4
Nlrc4
Gsdmd
Irf1
Irf7
Spi1
Lyz2
Ctsk
Il1a
Il1b
Il2rg
Il18
Il1rn
Tnf
Apoptosis
Inflammasome Complex
Phagocytic Vesicle
Lytic Vacuole
Endosome
Endolysosome
Late Endosome
Vacuole
Endocytic Vesicle
Complement
Inflammatory Response
IFNα Response
IFNγ Response
JAK/STAT Signaling Pathway
TNF Pathway
Shp2 Pathway
Erk1/2 Cascade
Empty
Siglec-F 2xY->F
CD33 2xY->F
Siglec-5 2xY->F
Siglec-8 2xY->F
Siglec-F
CD33
Siglec-5
Siglec-8
z-score / NES
E
Siglec mRNA DEGs
upregulated
downregulated
Siglec-F
CD33
Siglec-5
Siglec-8
F
pINDUCER + Dox 48 hours
mRNA Fold Change
Siglec-F
2xY->F
C1qa
IL-1β
β-actin
G
Siglec-F
2xY->F
Dox (hrs)
kDa
IL-1β
β-tub
35
50

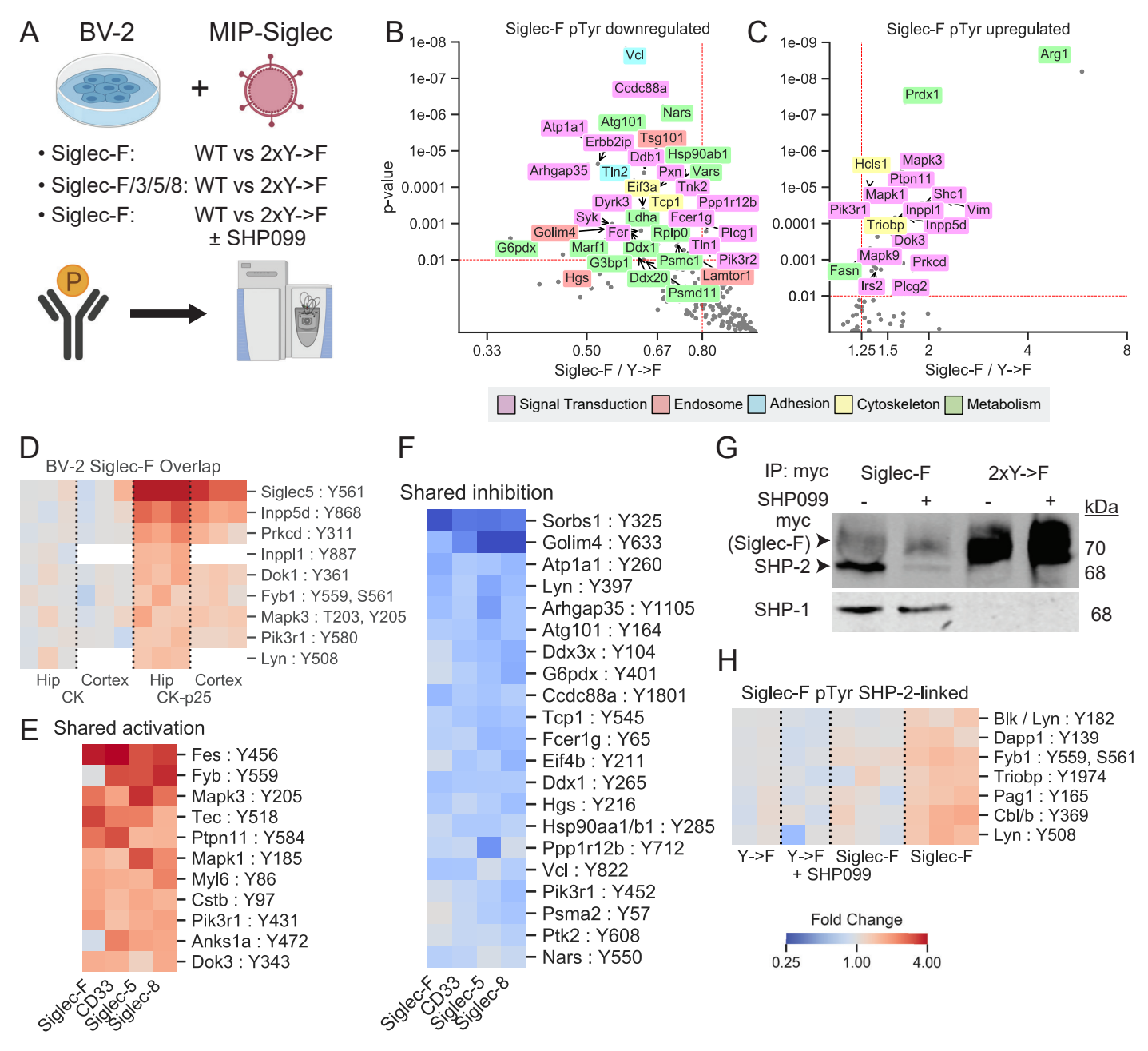
A
BV-2
MIP-Siglec
+
• Siglec-F: WT vs 2xY->F
• Siglec-F/3/5/8: WT vs 2xY->F
• Siglec-F: WT vs 2xY->F ± SHP099
P
B
Siglec-F pTyr downregulated
p-value
Siglec-F / Y->F
C
Siglec-F pTyr upregulated
Siglec-F / Y->F
Signal Transduction
Endosome
Adhesion
Cytoskeleton
Metabolism
D
BV-2 Siglec-F Overlap
Siglec5 : Y561
Inpp5d : Y868
Prkcd : Y311
Inppl1 : Y887
Dok1 : Y361
Fyb1 : Y559, S561
Mapk3 : T203, Y205
Pik3r1 : Y580
Lyn : Y508
Hip
Cortex
Hip
Cortex
CK
CK-p25
E
Shared activation
Fes : Y456
Fyb : Y559
Mapk3 : Y205
Tec : Y518
Ptpn11 : Y584
Mapk1 : Y185
Myl6 : Y86
Cstb : Y97
Pik3r1 : Y431
Anks1a : Y472
Dok3 : Y343
Siglec-F
CD33
Siglec-5
Siglec-8
F
Shared inhibition
Sorbs1 : Y325
Golim4 : Y633
Atp1a1 : Y260
Lyn : Y397
Arhgap35 : Y1105
Atg101 : Y164
Ddx3x : Y104
G6pdx : Y401
Ccdc88a : Y1801
Tcp1 : Y545
Fcer1g : Y65
Eif4b : Y211
Ddx1 : Y265
Hgs : Y216
Hsp90aa1/b1 : Y285
Ppp1r12b : Y712
Vcl : Y822
Pik3r1 : Y452
Psma2 : Y57
Ptk2 : Y608
Nars : Y550
Siglec-F
CD33
Siglec-5
Siglec-8
G
IP: myc
Siglec-F
2xY->F
SHP099
-
+
-
+
kDa
myc (Siglec-F)
SHP-2
SHP-1
70
68
68
H
Siglec-F pTyr SHP-2-linked
Blk / Lyn : Y182
Dapp1 : Y139
Fyb1 : Y559, S561
Triobp : Y1974
Pag1 : Y165
Cbl/b : Y369
Lyn : Y508
Y->F
Y->F + SHP099
Siglec-F
Siglec-F
Fold Change
0.25
1.00
4.00

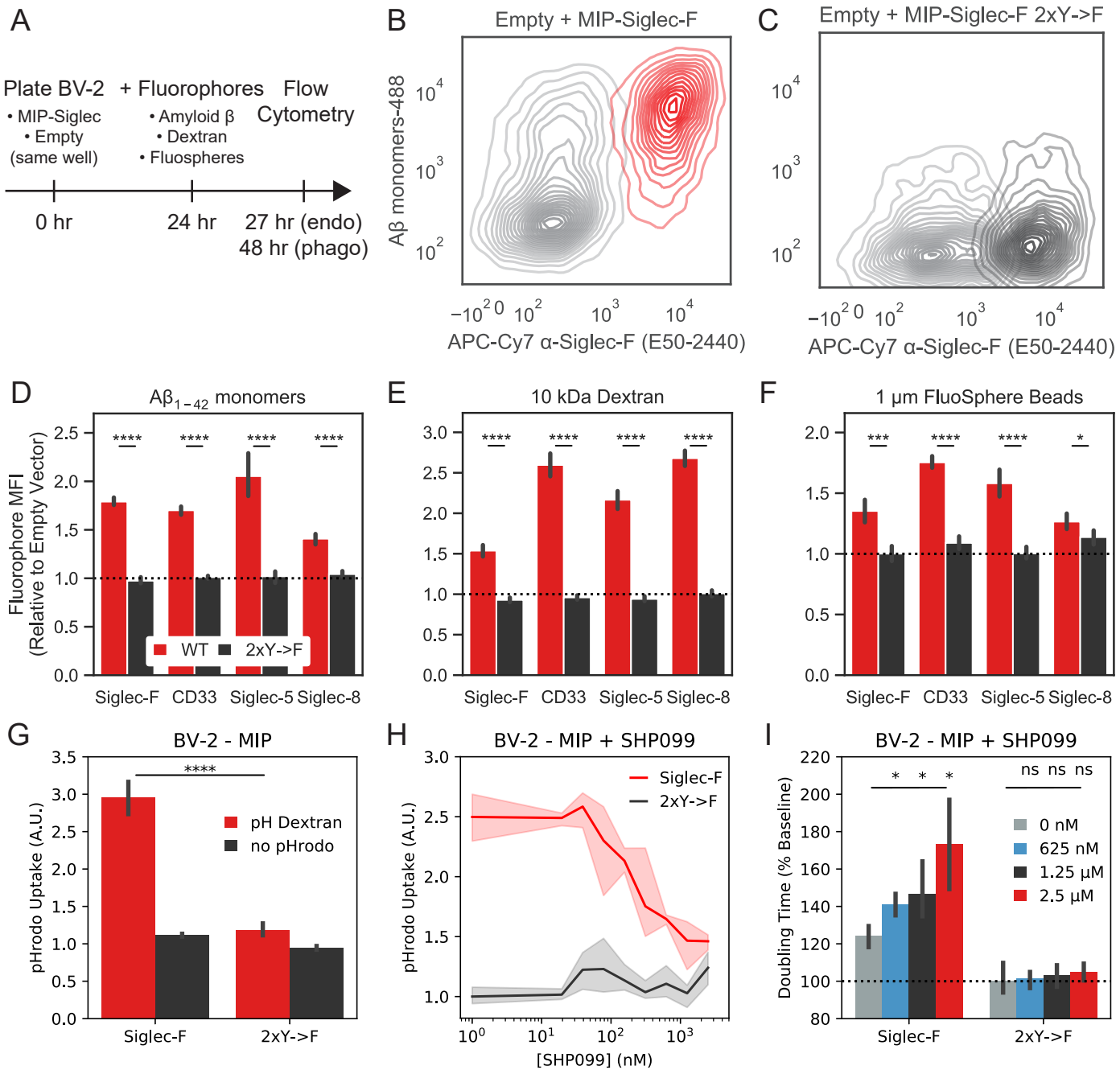
A
Plate BV-2
• MIP-Siglec
• Empty
(same well)
+ Fluorophores
• Amyloid β
• Dextran
• Fluospheres
Flow Cytometry
0 hr
24 hr
27 hr (endo)
48 hr (phago)
B
Empty + MIP-Siglec-F
Aβ monomers-488
APC-Cy7 α-Siglec-F (E50-2440)
C
Empty + MIP-Siglec-F 2xY->F
APC-Cy7 α-Siglec-F (E50-2440)
D
Aβ1−42 monomers
Fluorophore MFI
(Relative to Empty Vector)
WT
2xY->F
Siglec-F
CD33
Siglec-5
Siglec-8
E
10 kDa Dextran
F
1 μm FluoSphere Beads
G
BV-2 - MIP
pHrodo Uptake (A.U.)
pH Dextran
no pHrodo
H
BV-2 - MIP + SHP099
[SHP099] (nM)
I
BV-2 - MIP + SHP099
Doubling Time (% Baseline)
0 nM
625 nM
1.25 μM
2.5 μM

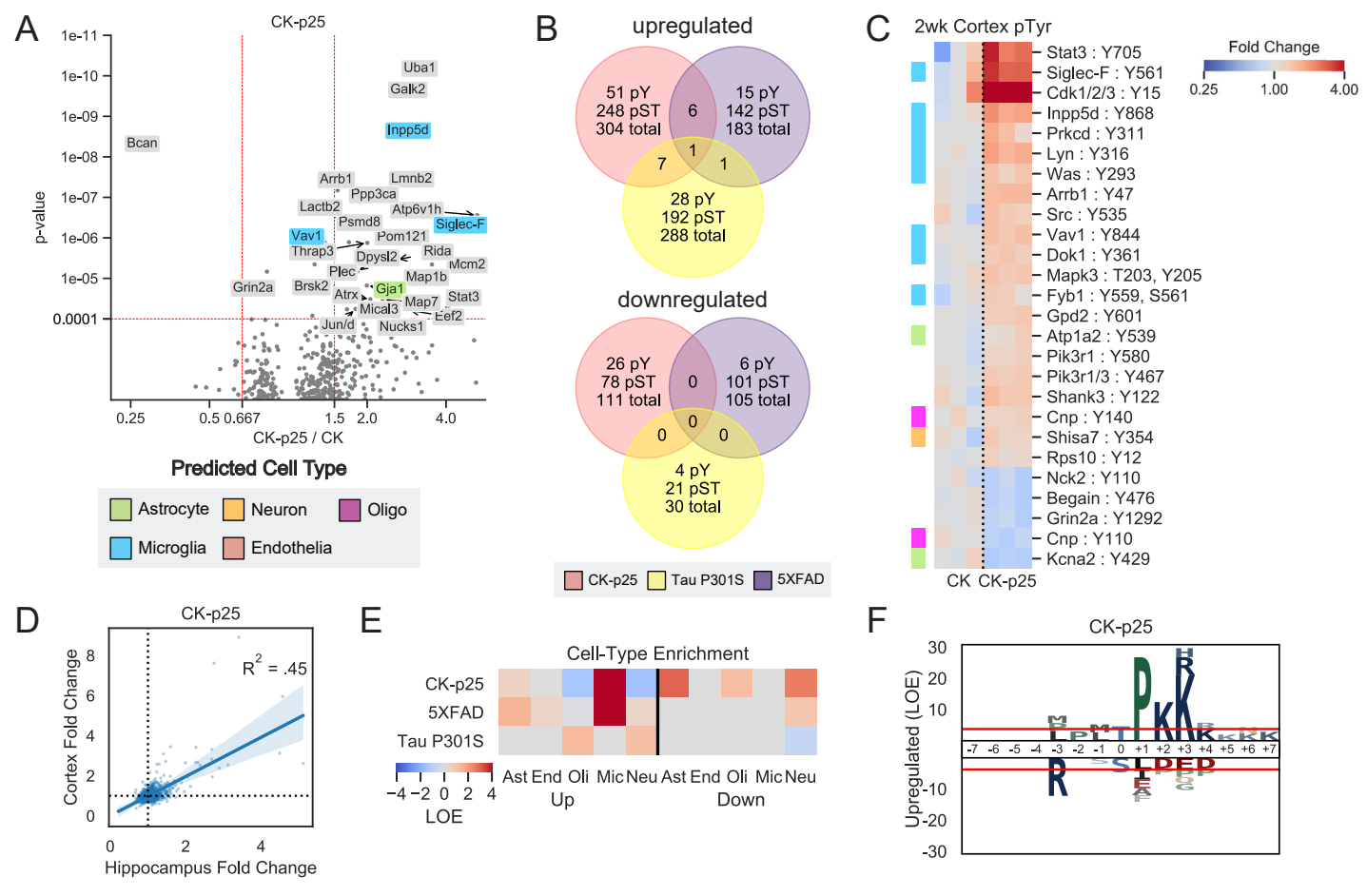
A
CK-p25
p-value
1e-11
1e-10
1e-09
1e-08
1e-07
1e-06
1e-05
0.0001
Uba1
Galk2
Inpp5d
Bcan
Arrb1
Lmnb2
Ppp3ca
Lactb2
Atp6v1h
Psmd8
Siglec-F
Vav1
Pom121
Thrap3
Dpysl2
Rida
Mcm2
Plec
Map1b
Grin2a
Brsk2
Gja1
Atrx
Stat3
Mical3
Map7
Eef2
Jun/d
Nucks1
0.25
0.5
0.667
1.5
2.0
4.0
CK-p25 / CK
Predicted Cell Type
Astrocyte
Neuron
Oligo
Microglia
Endothelia
B
upregulated
51 pY
248 pST
304 total
6
15 pY
142 pST
183 total
1
7
1
28 pY
192 pST
288 total
downregulated
26 pY
78 pST
111 total
0
6 pY
101 pST
105 total
0
0
0
4 pY
21 pST
30 total
CK-p25
Tau P301S
5XFAD
C
2wk Cortex pTyr
Fold Change
0.25
1.00
4.00
Stat3 : Y705
Siglec-F : Y561
Cdk1/2/3 : Y15
Inpp5d : Y868
Prkcd : Y311
Lyn : Y316
Was : Y293
Arrb1 : Y47
Src : Y535
Vav1 : Y844
Dok1 : Y361
Mapk3 : T203, Y205
Fyb1 : Y559, S561
Gpd2 : Y601
Atp1a2 : Y539
Pik3r1 : Y580
Pik3r1/3 : Y467
Shank3 : Y122
Cnp : Y140
Shisa7 : Y354
Rps10 : Y12
Nck2 : Y110
Begain : Y476
Grin2a : Y1292
Cnp : Y110
Kcna2 : Y429
CK
CK-p25
D
CK-p25
R^2 = .45
Cortex Fold Change
0
2
4
6
8
Hippocampus Fold Change
E
Cell-Type Enrichment
CK-p25
5XFAD
Tau P301S
−4 −2 0 2 4
LOE
Ast End Oli Mic Neu Ast End Oli Mic Neu
Up
Down
F
CK-p25
Upregulated (LOE)
30
20
10
-10
-20
-30
-7 -6 -5 -4 -3 -2 -1 0 +1 +2 +3 +4 +5 +6 +7

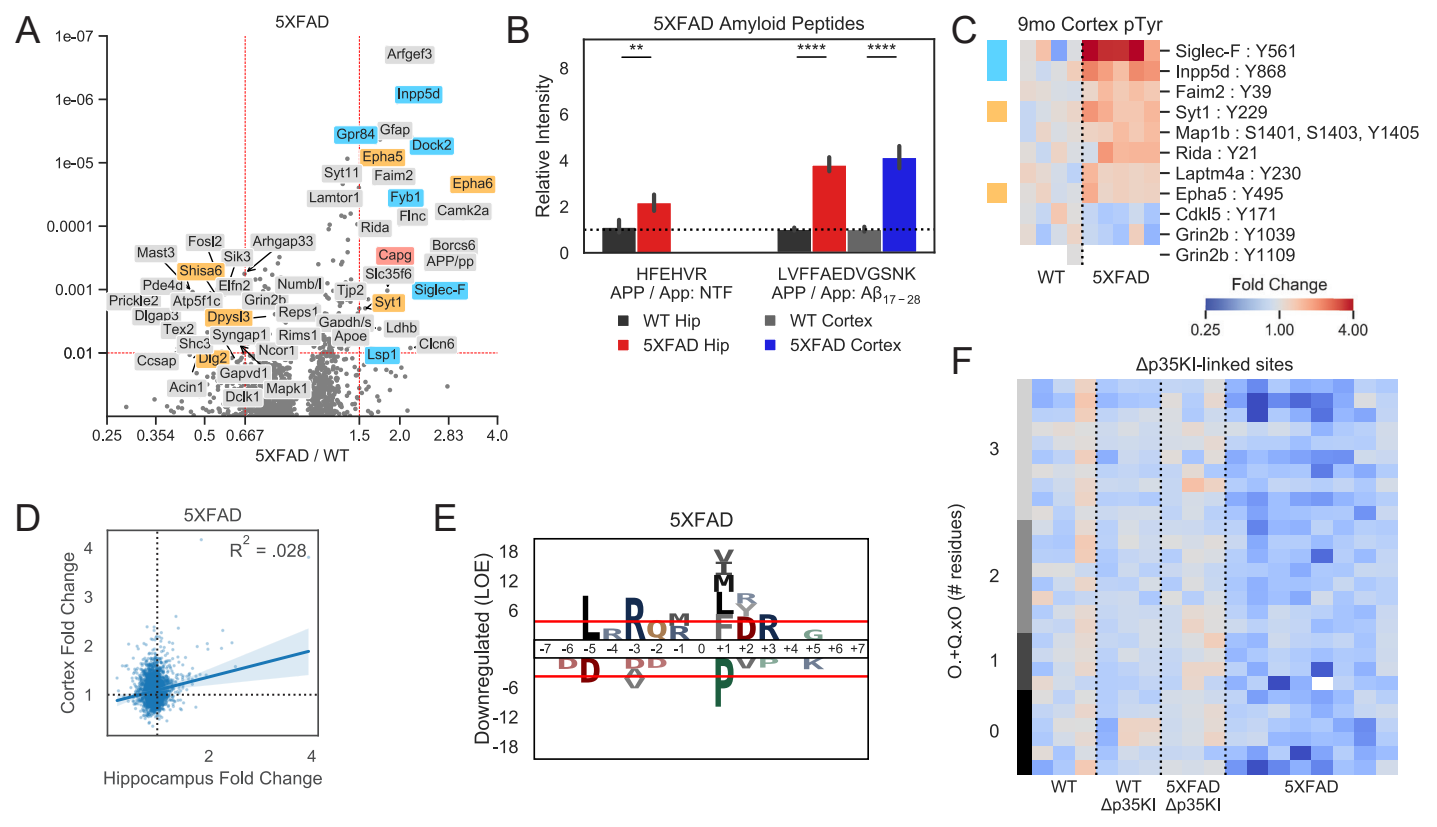
A
5XFAD
1e-07
1e-06
1e-05
0.0001
0.001
0.01
Arfgef3
Inpp5d
Gpr84
Gfap
Dock2
Epha5
Syt11
Faim2
Epha6
Lamtor1
Fyb1
Flnc
Camk2a
Rida
Fosl2
Arhgap33
Mast3
Sik3
Capg
Borcs6
APP/pp
Shisa6
Slc35f6
Pde4d
Elfn2
Numbl
Tjp2
Siglec-F
Prickle2
Atp5f1c
Grin2b
Syt1
Dlgap3
Dpysl3
Reps1
Gapdh/s
Tex2
Syngap1
Rims1
Apoe
Ldhb
Shc3
Ncor1
Clcn6
Ccsap
Dlg2
Lsp1
Gapvd1
Acin1
Mapk1
Dclk1
0.25
0.354
0.5
0.667
1.5
2.0
2.83
4.0
5XFAD / WT
B
5XFAD Amyloid Peptides
Relative Intensity
0
2
4
6
8
**
****
****
HFEHVR
APP / App: NTF
LVFFAEDVGSNK
APP / App: Aβ17 – 28
WT Hip
5XFAD Hip
WT Cortex
5XFAD Cortex
C
9mo Cortex pTyr
Siglec-F : Y561
Inpp5d : Y868
Faim2 : Y39
Syt1 : Y229
Map1b : S1401, S1403, Y1405
Rida : Y21
Laptm4a : Y230
Epha5 : Y495
Cdkl5 : Y171
Grin2b : Y1039
Grin2b : Y1109
WT
5XFAD
Fold Change
0.25
1.00
4.00
D
5XFAD
R2 = .028
Cortex Fold Change
1
2
3
4
2
4
Hippocampus Fold Change
E
5XFAD
Downregulated (LOE)
18
12
6
-6
-12
-18
-7 -6 -5 -4 -3 -2 -1 0 +1 +2 +3 +4 +5 +6 +7
F
Δp35KI-linked sites
O.+Q.xO (# residues)
0
1
2
3
WT
WT
Δp35KI
5XFAD
Δp35KI
5XFAD

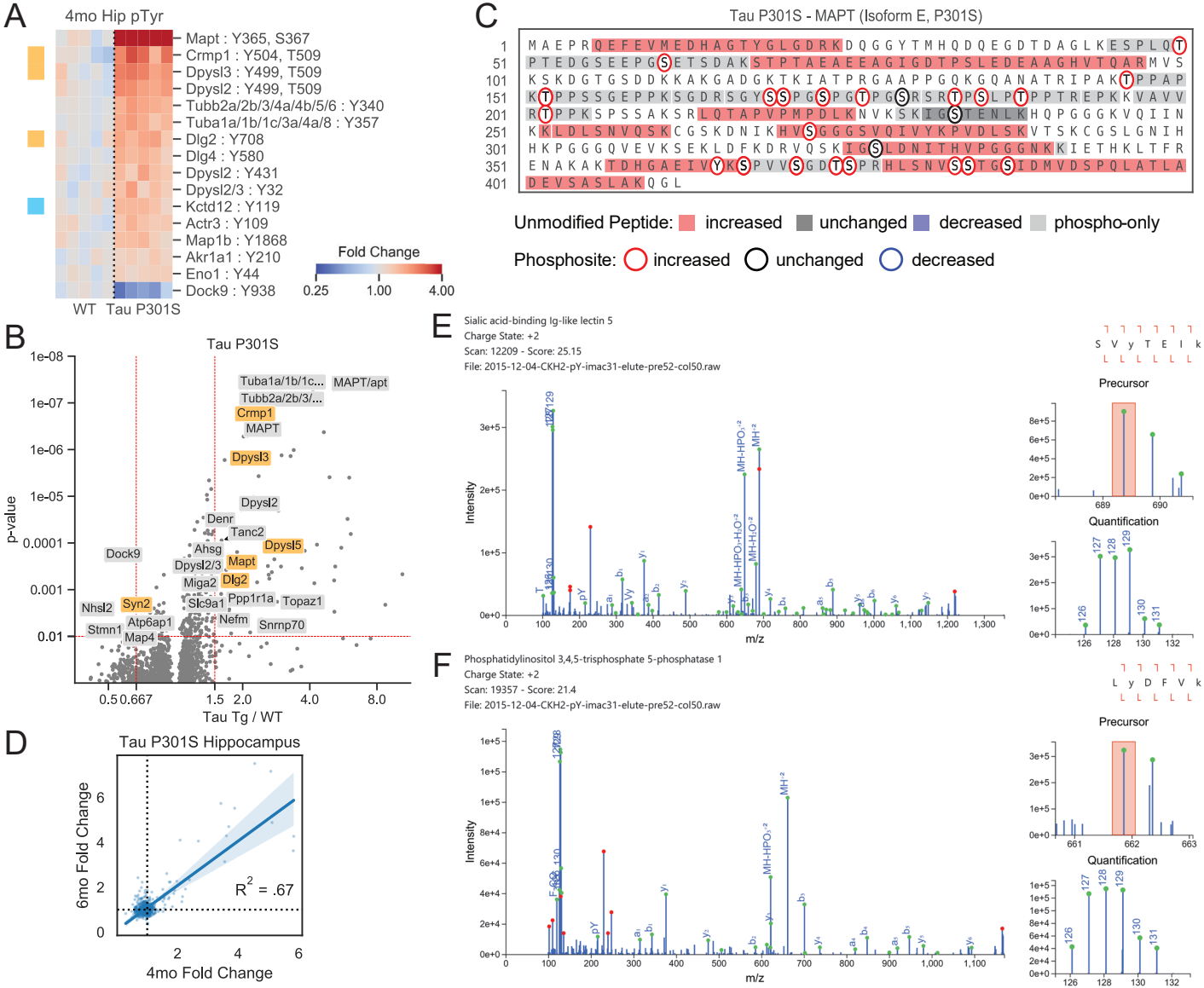
A
4mo Hip pTyr
Mapt : Y365, S367
Crmp1 : Y504, T509
Dpysl3 : Y499, T509
Dpysl2 : Y499, T509
Tubb2a/2b/3/4a/4b/5/6 : Y340
Tuba1a/1b/1c/3a/4a/8 : Y357
Dlg2 : Y708
Dlg4 : Y580
Dpysl2 : Y431
Dpysl2/3 : Y32
Kctd12 : Y119
Actr3 : Y109
Map1b : Y1868
Akr1a1 : Y210
Eno1 : Y44
Dock9 : Y938
Fold Change
0.25
1.00
4.00
WT
Tau P301S
B
Tau P301S
p-value
Tau Tg / WT
Tuba1a/1b/1c...
MAPT/apt
Tubb2a/2b/3/...
Crmp1
MAPT
Dpysl3
Dpysl2
Denr
Tanc2
Dpysl5
Dock9
Ahsg
Dpysl2/3
Mapt
Miga2
Dlg2
Nhsl2
Syn2
Slc9a1
Ppp1r1a
Topaz1
Stmn1
Atp6ap1
Nefm
Snrnp70
Map4
C
Tau P301S - MAPT (Isoform E, P301S)
Unmodified Peptide:
increased
unchanged
decreased
phospho-only
Phosphosite:
increased
unchanged
decreased
D
Tau P301S Hippocampus
6mo Fold Change
4mo Fold Change
R2 = .67
E
Sialic acid-binding Ig-like lectin 5
Charge State: +2
Scan: 12209 - Score: 25.15
File: 2015-12-04-CKH2-pY-imac31-elute-pre52-col50.raw
Intensity
m/z
Precursor
Quantification
F
Phosphatidylinositol 3,4,5-trisphosphate 5-phosphatase 1
Charge State: +2
Scan: 19357 - Score: 21.4
File: 2015-12-04-CKH2-pY-imac31-elute-pre52-col50.raw
Intensity
m/z
Precursor
Quantification

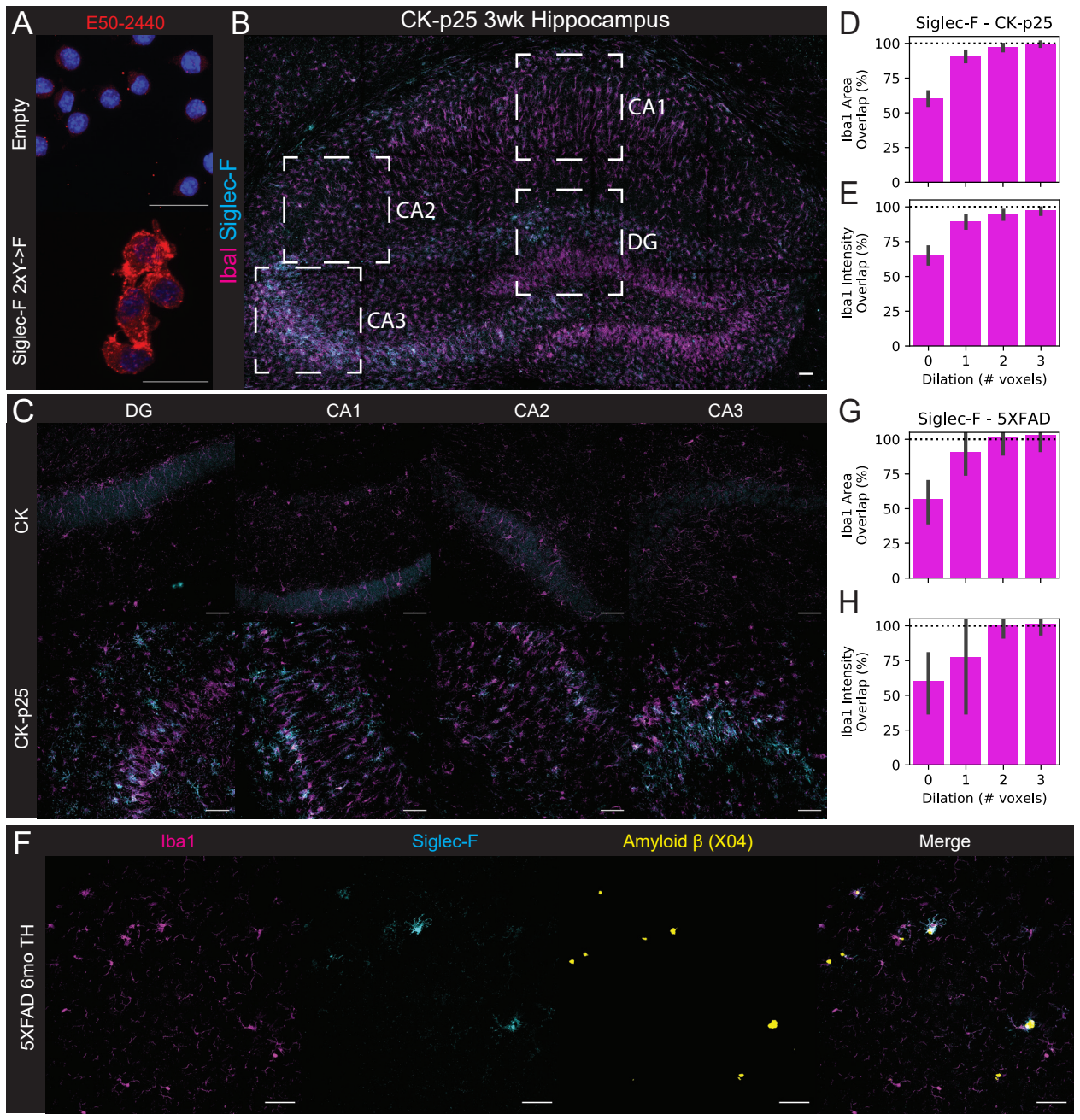
A
E50-2440
Empty
Siglec-F 2xY->F
B
CK-p25 3wk Hippocampus
Iba1 Siglec-F
CA1
CA2
CA3
DG
D
Siglec-F - CK-p25
Iba1 Area Overlap (%)
E
Iba1 Intensity Overlap (%)
Dilation (# voxels)
C
DG
CA1
CA2
CA3
CK
CK-p25
G
Siglec-F - 5XFAD
H
F
Iba1
Siglec-F
Amyloid β (X04)
Merge
5XFAD 6mo TH

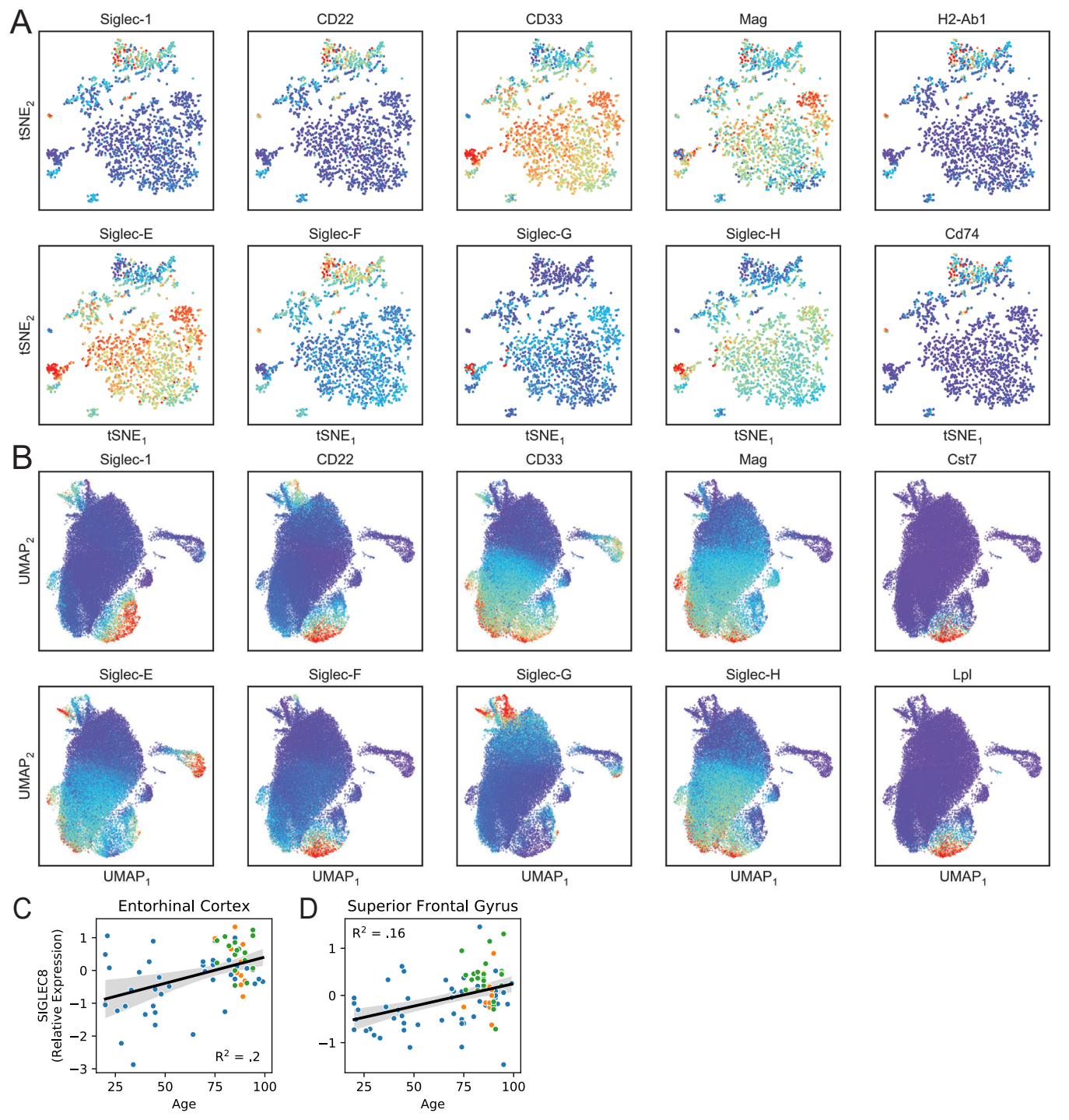
A
Siglec-1
CD22
CD33
Mag
H2-Ab1
Siglec-E
Siglec-F
Siglec-G
Siglec-H
Cd74
tSNE2
tSNE1
B
Siglec-1
CD22
CD33
Mag
Cst7
Siglec-E
Siglec-F
Siglec-G
Siglec-H
Lpl
UMAP2
UMAP1
C
Entorhinal Cortex
SIGLEC8 (Relative Expression)
R2 = .2
Age
D
Superior Frontal Gyrus
R2 = .16
Age

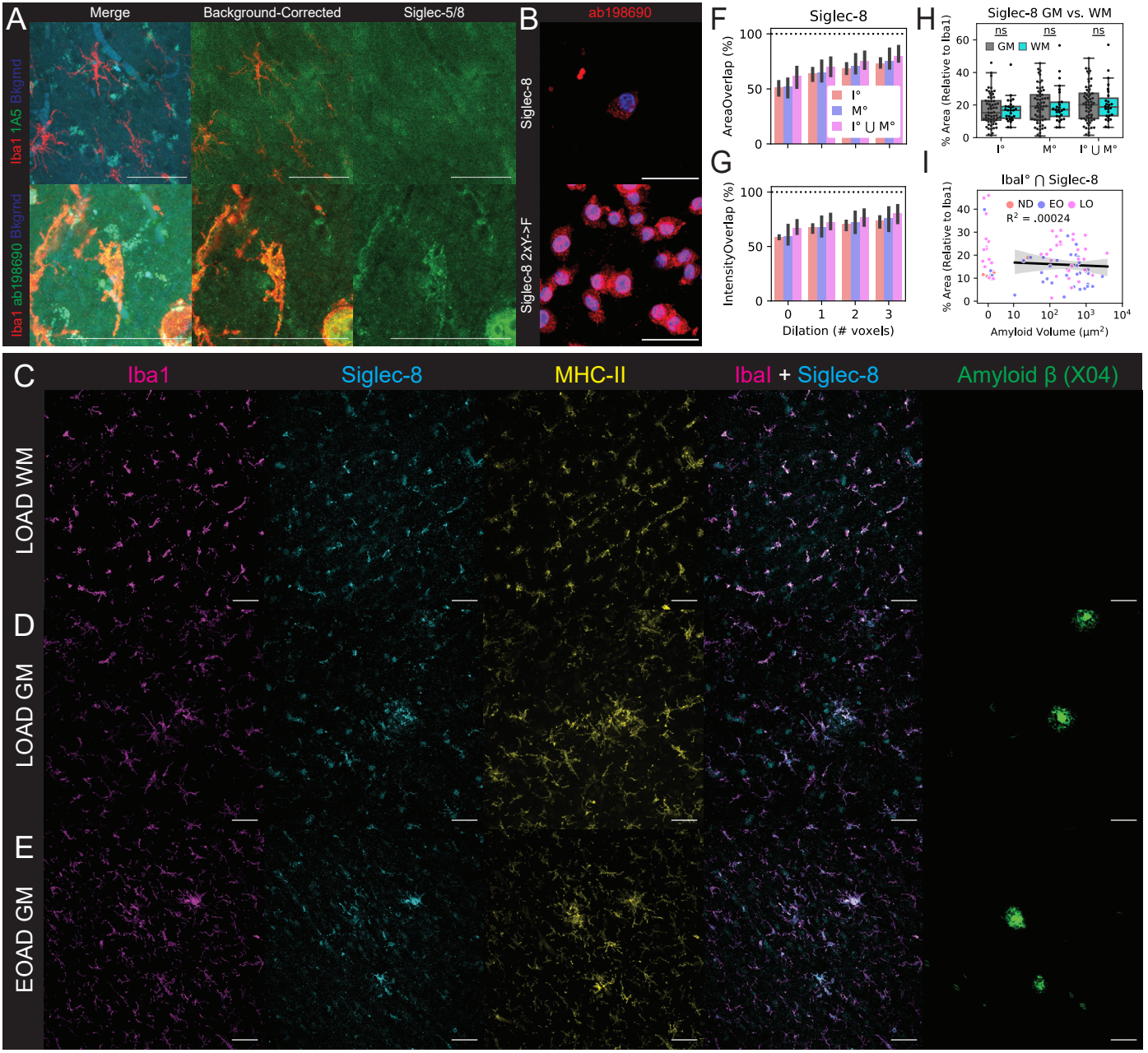
A
Merge
Background-Corrected
Siglec-5/8
Iba1 1A5 Bkgrnd
Iba1 ab198690 Bkgrnd
B
ab198690
Siglec-8
Siglec-8 2xY->F
F
Siglec-8
AreaOverlap (%)
I°
M°
I° ⋃ M°
G
IntensityOverlap (%)
Dilation (# voxels)
H
Siglec-8 GM vs. WM
ns
GM
WM
% Area (Relative to Iba1)
I°
M°
I° ⋃ M°
I
Iba1° ⋂ Siglec-8
ND
EO
LO
R² = .00024
% Area (Relative to Iba1)
Amyloid Volume (μm²)
C
Iba1
Siglec-8
MHC-II
Iba1 + Siglec-8
Amyloid β (X04)
LOAD WM
D
LOAD GM
E
EOAD GM

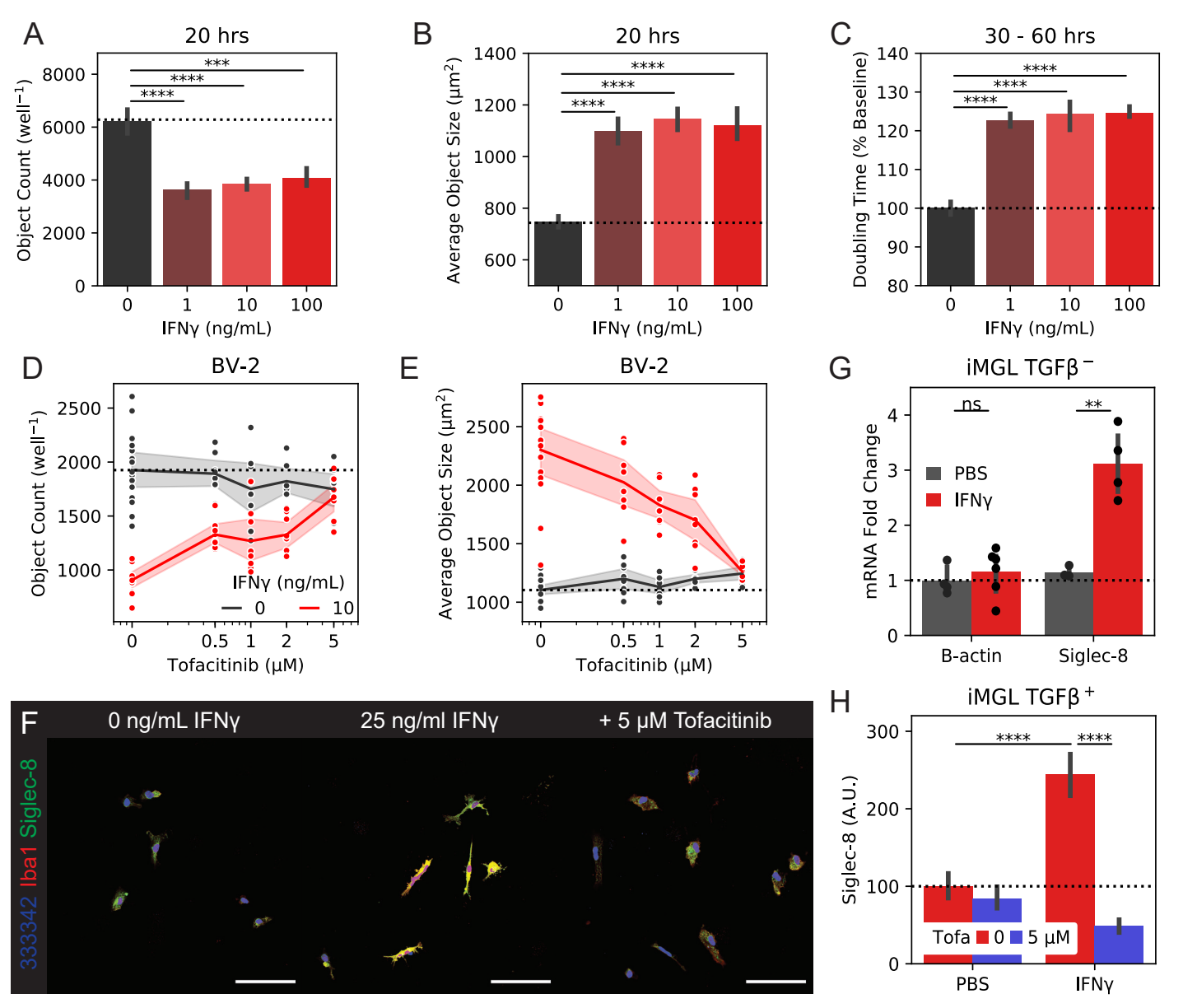
A
20 hrs
Object Count (well^{-1})
IFNγ (ng/mL)
B
20 hrs
Average Object Size (μm^2)
IFNγ (ng/mL)
C
30 - 60 hrs
Doubling Time (% Baseline)
IFNγ (ng/mL)
D
BV-2
Object Count (well^{-1})
IFNγ (ng/mL)
0
10
Tofacitinib (μM)
E
BV-2
Average Object Size (μm^2)
Tofacitinib (μM)
G
iMGL TGFβ$^-$
mRNA Fold Change
ns
**
PBS
IFNγ
B-actin
Siglec-8
F
0 ng/mL IFNγ
25 ng/ml IFNγ
+ 5 μM Tofacitinib
333342 Iba1 Siglec-8
H
iMGL TGFβ$^+$
Siglec-8 (A.U.)
Tofa 0 5 μM
PBS
IFNγ

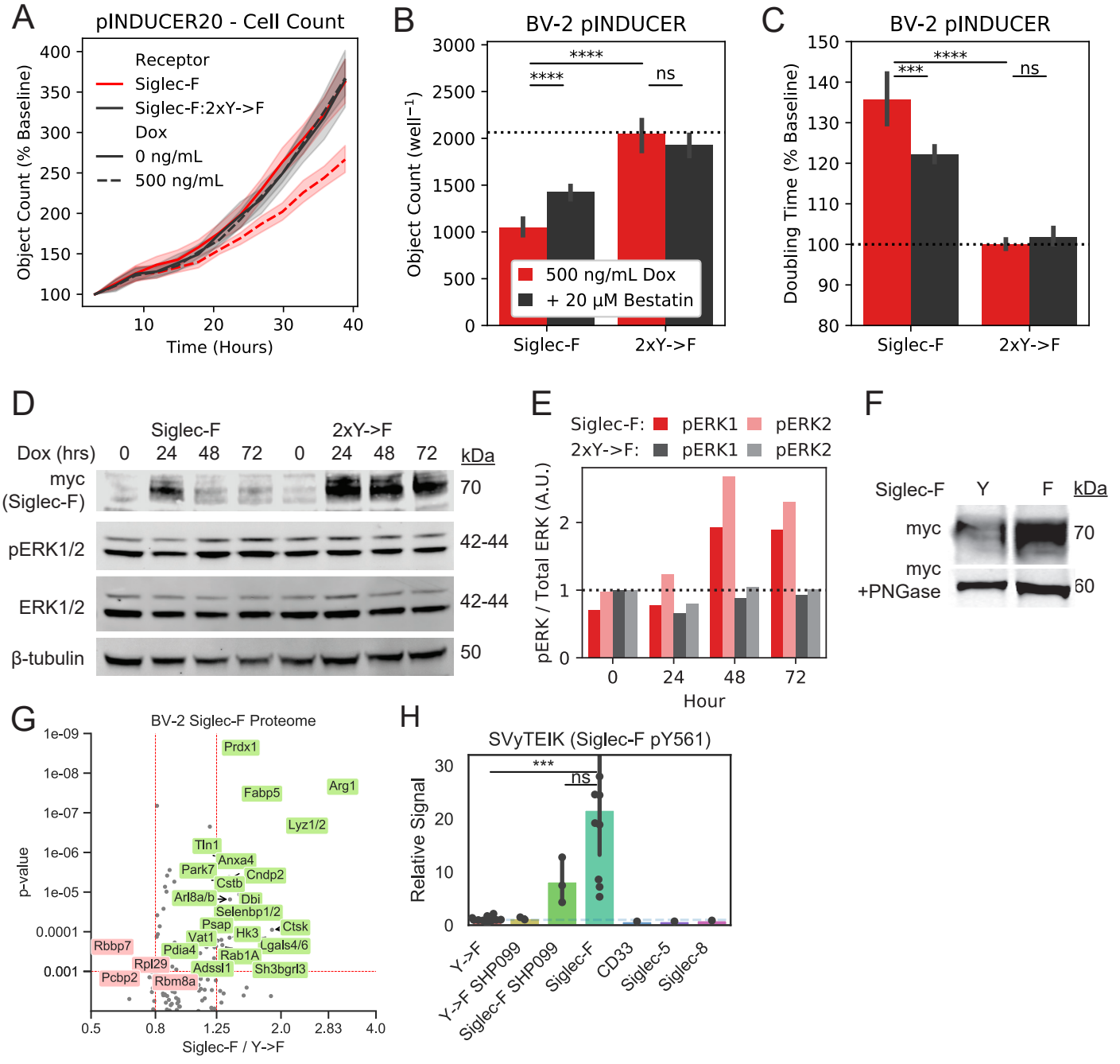
A
pINDUCER20 - Cell Count
Object Count (% Baseline)
Time (Hours)
Receptor
Siglec-F
Siglec-F:2xY->F
Dox
0 ng/mL
500 ng/mL
B
BV-2 pINDUCER
Object Count (well^{-1})
****
****
ns
500 ng/mL Dox
+ 20 μM Bestatin
Siglec-F
2xY->F
C
BV-2 pINDUCER
Doubling Time (% Baseline)
***
****
ns
Siglec-F
2xY->F
D
Siglec-F
2xY->F
Dox (hrs)
0
24
48
72
0
24
48
72
kDa
myc (Siglec-F)
70
pERK1/2
42-44
ERK1/2
42-44
β-tubulin
50
E
Siglec-F: pERK1 pERK2
2xY->F: pERK1 pERK2
pERK / Total ERK (A.U.)
Hour
F
Siglec-F
Y
F
kDa
myc
70
myc +PNGase
60
G
BV-2 Siglec-F Proteome
p-value
Siglec-F / Y->F
Prdx1
Arg1
Fabp5
Lyz1/2
Tln1
Anxa4
Park7
Cndp2
Cstb
Arl8a/b
Dbi
Selenbp1/2
Psap
Ctsk
Hk3
Vat1
Lgals4/6
Rbbp7
Pdia4
Rab1A
Rpl29
Adssl1
Sh3bgrl3
Pcbp2
Rbm8a
H
SVyTEIK (Siglec-F pY561)
Relative Signal
***
ns
Y->F
Y->F SHP099
Siglec-F SHP099
Siglec-F
CD33
Siglec-5
Siglec-8